THE ENVIRONMENTS IN WHICH STARS AND CIRCUMSTELLAR DISCS FORM

Christopher John Poulton

A Thesis Submitted for the Degree of PhD
at the
University of St. Andrews

2008

THE UNIVERSITY OF ST. ANDREWS

The Environments in which Stars and Circumstellar Discs Form

Christopher John Poulton

Submitted for the degree of Ph.D.

June 27, 2008

DECLARATION

I, Christopher John Poulton, hereby certify that this thesis, which is approximately 40,000 words in length, has been written by me, that it is the record of work carried out by me and that it has not been submitted in any previous application for a higher degree.

I was admitted as a research student in October 2004 and as a candidate for the degree of PhD in October 2004; the higher study for which this is a record was carried out in the University of St Andrews between 2004 and 2008.

Date: June 27, 2008 Signature of Candidate:

I hereby certify that the candidate has fulfilled the conditions of the Resolution and Regulations appropriate for the degree of PhD in the University of St Andrews and that the candidate is qualified to submit this thesis in application for that degree.

Date: June 27, 2008 Signature of Supervisor:

The following is an agreed request by candidate and supervisor regarding the electronic publication of this thesis:

Access to printed copy and electronic publication of thesis through the University of St Andrews.

Date: June 27, 2008 Signature of Candidate:

Date: June 27, 2008 Signature of Supervisor:

ACKNOWLEDGMENTS

I would first like to thank my supervisor, Jane Greaves, for her excellent guidance throughout my PhD, reading through and correcting my work and encouraging me to complete tasks more quickly. I was also very fortunate to have Ian Bonnell as a second supervisor whose enthusiasm and ideas helped make this thesis possible. I would also like to thank Andrew Cameron for his invaluable assistance analysing the ϵ Eridani data.

Special thanks to Tom Robitaille, for allowing the use of his SED fitter and for teaching me new computer skills. I am also grateful to all of the people at the Spitzer helpdesk, particularly David Makovoz, for answering many questions regarding point source extraction. Thank you also to Jonathan Williams and Mark Heyer for their feedback when working on the Rosette paper and John Scalo and Tom Megeath for their inciteful responses to my emails.

I gratefully acknowledge PPARC/SciTech for financial support over the course of my PhD.

Thank you to all of my fellow PhD students, especially Garry Angus for making life in the astronomy department more interesting and entertaining. I also thank my first office mates Paul Clark and Clare Dobbs for helping me in the early days with computer problems.

I would like to thank my parents, who have always shown interest in my studies, for encouraging me to pursue a PhD in the first place. Finally, I would like thank my girlfriend Emily who has been a source of great support throughout my PhD and for making me feel better whenever I had a bad day or felt disheartened.

PREFACE

Chapters 3 and 4 of this thesis are based on the first author papers listed below.

[1] Poulton, C.J., Greaves, J.S., Cameron, A.C.
2006, MNRAS, 372, 53

[2] Poulton, C.J., Robitaille, T.P., Greaves, J.S., Bonnell, I.A., Williams, J.P., Heyer, M.H.
2008, MNRAS, 384, 1249

THE UNIVERSITY OF ST. ANDREWS

The Environments in which Stars and Circumstellar Discs Form

Submitted for the degree of Ph.D.

June 27, 2008

Christopher John Poulton

ABSTRACT

In this thesis, images of a debris disc are used to examine the evidence for the presence of a Neptune-like planet around ϵ Eridani and detections of protoplanetary discs are used to investigate the evidence for star and future planet formation.

A χ^2 analysis of the movement of clumps in the ϵ Eridani debris disc is presented using 850 μm SCUBA data taken over a 4 year period and compared with results from simulated data. A rotation is detected at the 2σ level and is faster than the Keplerian rate, consistent with theoretical models in which dust trapped in mean motion resonances tracks a planet orbiting the star at $\approx$26 AU. Future observations that could be taken with SCUBA-2 are also simulated and demonstrate that the true rotation rate cannot be recovered without the identification of the background sources aligned with the clumpy debris disc.

Near and mid infrared observations are used to perform a survey of YSOs in the Rosette Molecular Cloud. Although triggering by compression of the molecular cloud by the expanding HII region at the centre of the Rosette Nebula is a possible origin for some of the recent star formation, the majority of the active star formation is occurring in already dense regions of the cloud not compressed by the expansion of the HII region.

Mid-infrared data for W4 and SCUBA data for the star forming region AFGL 333 are also presented. A survey of YSOs reveals that whilst some young sources are coincident with the W4 loop, consistent with a scenario of triggered star formation in a swept-up shell, several young sources are found to be forming outside of this ring. The dust temperature and mass of AFGL 333 are estimated and the result implies a star formation efficiency of $\sim$4% in the W4 loop.

"We've discovered a massive dust and gas cloud which is either the beginning of a new star, or just an awful lot of dust and gas."

ScienceCartoonsPlus.com

CONTENTS

CHAPTER 1

Introduction

One of the most intriguing questions in science is whether or not life is unique to Earth or ubiquitous throughout the whole universe. An important part of solving this puzzle is to determine the abundance of Earth-like planets and planetary systems like the solar system. It is in tackling this problem where the study of circumstellar discs plays an important role. Protoplanetary discs exist only around young stars that have formed very recently and are formed from the same primordial material as the star. Therefore, by identifying stars with protoplanetary discs, the environments in which they are formed can be examined to determine how long the disc typically survives, setting the timescale for the formation of planetary systems. Debris discs are formed at a later stage in a star's life and are formed by the continual replenishment of dust in the disc by collisions between planetesimals that have formed from the protoplanetary discs. The detection of a debris disc around a star infers the presence of orbiting bodies that collide to replenish the dust in the disc, indicative of a planetary system. This chapter describes the background and theory used later: for debris discs in section 1.1 and star formation in section 1.2.

1.1 Debris Discs

In 1983, data from the Infrared Astronomical Satellite (IRAS) revealed an unexpected far-infrared excess beyond 12 μm during routine calibration observations of Vega. More specifically, the radiation detected at wavelengths 25 μm to 100 μm is more than can be produced by the photosphere of the star. This was later interpreted as thermal radiation from particles with radii larger than 1 mm, heated by radiation from the star to temperatures of 85 K at distances of $\sim$85 AU (Aumann et al., 1984). This was the first detection of solid particles around main sequence stars outside of our solar system without significant mass loss (i.e. not giants).

Following the initial discovery, excess emission was detected from a number of other stars in the far infrared (Aumann, 1985; Mannings & Barlow, 1998), and later at submillimetre (Zuckerman & Becklin, 1993) and mid infrared (Fajardo-Acosta et al., 1998) wavelengths. Only a small number of objects have been resolved in optical, near-infrared and far-infrared wavelengths, e.g. Smith & Terrile (1984) were able to image a disc around β Pictoris in the infrared, from the starlight scattered off the dust using coronagraphs. The difficulty came about because the radiation from the star being observed dominated the faint radiation scattered by the dust (Kalas & Jewitt, 1996). In 1997, the Submillimetre Common-User Bolometer Array (SCUBA) on the James Clerk Maxwell Telescope (JCMT) came into operation, and until 2005 was used to image the warm dust around β Pictoris, Fomalhaut, Vega (Holland et al., 1998) and η-Corvi (Wyatt et al., 2005), the sunlike stars ϵ Eridani (Greaves et al., 1998, 2005), HD 107146 (Williams et al., 2004), and τ Ceti (Greaves et al., 2004b) and the images obtained are discussed below.

1.1.1 Submillimetre Images of Debris Discs

Figure 1.1 shows the debris discs observed at 850 μm using SCUBA that are at distances smaller than 30 pc with their stellar disc parameters shown in Table 1.1. An important consideration when attempting to observe the debris discs at submillimetre wavelengths is that the observed radiation could originate from a background source such as a distant galaxy. Holland et al. (1998) estimate that there is a probability of 2.5% of finding a background galaxy within 10 arcsecs of the star and the counts agree within a factor of $\sim$2 with previous surveys (Smail et al., 1997). Features physically associated with the star should track with the proper motion of the star about which they are observed. Observations of ϵ Eridani by Greaves et al. (1998, 2005) span a period of 5 years and therefore the proper motion of the disc over this timescale should be observable. Some features thought to be part of the disc in 1998 now appear to be stationary with respect to the sky and it therefore looks as though these must be background objects such as dusty galaxies. The debris discs around Fomalhaut, β Pictoris, Vega, ϵ Eridani and τ Ceti are now discussed in more detail as examples of what can be deduced from submillimetre images and modelling of their spectral energy distributions (SEDs).

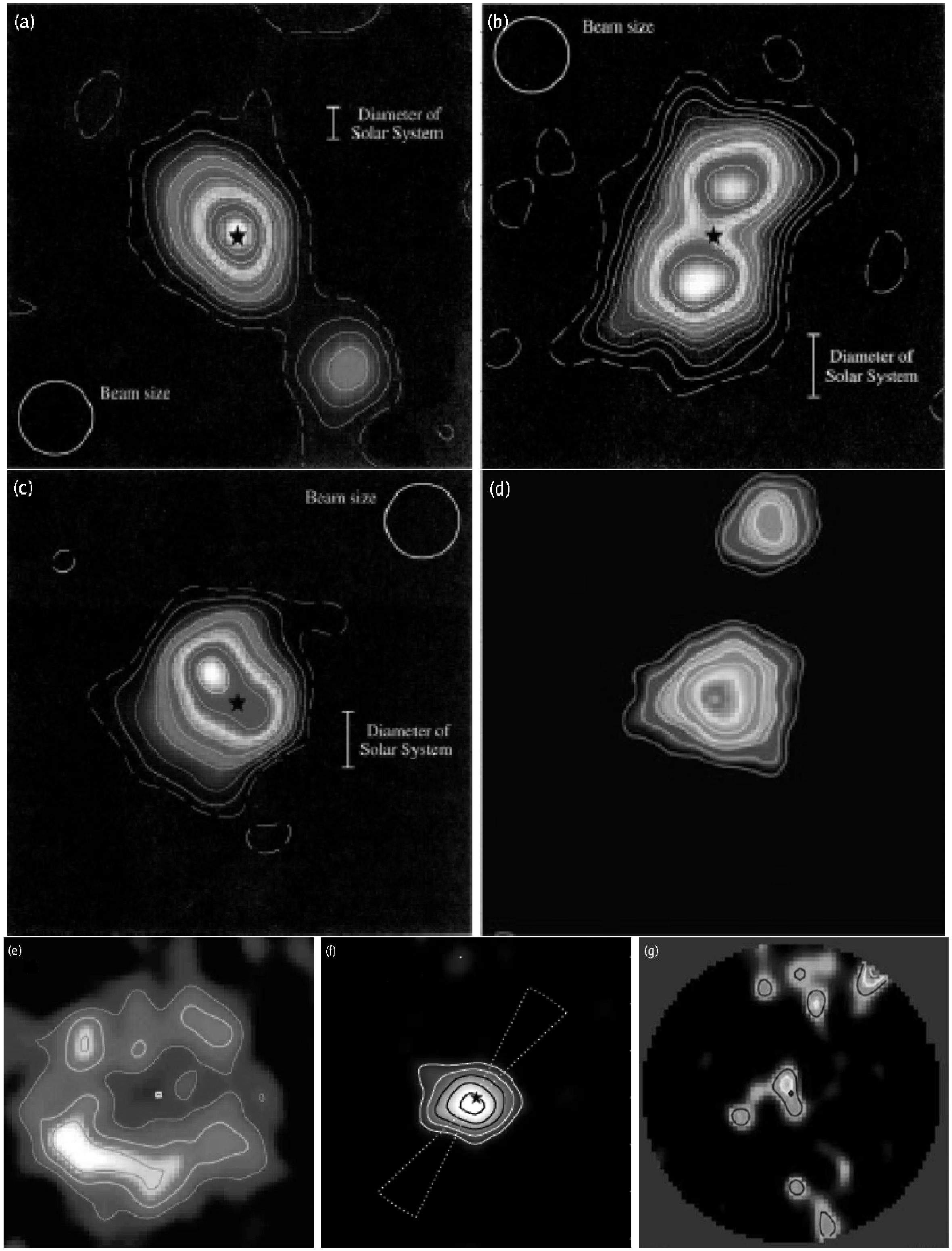

Figure 1.1: Submillimetre (850 μm) images of debris discs observed using SCUBA around (a) β Pictoris (Holland et al., 1998), (b) Fomalhaut (Holland et al., 1998), (c) Vega (Holland et al., 1998), (d) η-Corvi (Wyatt et al., 2005), (e) ϵ Eridani (Greaves et al., 2005), (f) HD 107146 (Williams et al., 2004) and (g) τ Ceti (Greaves et al., 2004b).

Table 1.1: Stellar and disc parameters of the stars imaged at submillimetre wavelengths.

Star	Spectral Type	Age (Gyr)	Distance (pc)	r_{in} (AU)	r_{out} (AU)	Dust Mass ($M_\oplus$)	Refs.[a]
β Pictoris	A5V	0.01-0.1	19.3	20	-[b]	0.096	1
Fomalhaut	A3V	0.2	7.7	125	185	0.018	2
Vega	A0V	0.35	7.8	80	120	0.009	1,3
ϵ Eridani	K2V	0.85	3.2	40	105	0.005	4,5
HD 107146	G2V	0.08-0.2	28.5	>31	150	0.1	6
η Corvi	F2V	1	18.2	100	150	0.04	7
Sun	G2V	4.5	-	30	~100	2.95×10^{-6}	4,8,9
τ Ceti	G8V	10	3.6	~10	~55	4.94×10^{-4}	4,5,10

[a]References: 1 - Dent et al. (2000); 2 - Holland et al. (2003); 3 - Holland et al. (1998); 4 - Greaves et al. (2005); 5 - Di Folco et al. (2004); 6 - Williams et al. (2004); 7 - Wyatt et al. (2005); 8 - Backman et al. (1995); 9 - Landgraf et al. (2002); 10 - Greaves et al. (2004b)

[b]No observed outer boundary

A-type Stars: Fomalhaut, β Pictoris and Vega

The submillimetre image of Fomalhaut obtained by Holland et al. (1998) using SCUBA shows that the dust emission peaks at two regions about 10 arc-seconds north and south of the star. Holland et al. (1998) proposed that this is consistent with a torus of dust with a central cavity about 60 AU in diameter, viewed at an inclination angle of 64±5° (an inclination of 0° indicates that the disc is orientated with its spin axis along the line of sight). Subsequent fits to spectral energy distributions (SEDs) and the submillimetre image obtained by Holland et al. (1998) implied the Fomalhaut submillimetre emission could be modelled as a 120 AU thick torus viewed edge-on (inclination >75°), with inner radius of 100 AU and an abrupt outer boundary of 140 AU (Dent et al., 2000). These figures have been re-calculated by Holland et al. (2003) and are shown in Table 1.1. Dent et al. (2000) compared the SEDs for models of the torus with differing densities in the inner cavity and found that the density in the cavity must be no more than 10% of that in the torus. The incination angle implied is consistent with the comparison between the observed rotation velocities for Fomalhaut and average rotation velocities for stars of the same spectral type (Backman & Paresce, 1993). The regions of peak dust emission at $\sim 10''$ from the star correspond to distances of about 80 AU from the star (Holland et al., 1998). This is slightly larger than the distance of the Kuiper Belt from the Sun (Backman et al., 1995). More recently, a 450 μm image of the Fomalhaut disc has been obtained with SCUBA at the JCMT (Holland et al., 2003). The image shows that the disc is significantly asymmetric and the implications of this are discussed later in this chapter.

The image of β Pictoris shows that the dust extends out to distances of 250 AU from the star and that the measured major and minor axes of the observed ellipse imply a disc inclined at angle of $>60°$ (Holland et al., 1998). Dent et al. (2000) were able to show that the optical and near-infrared models used to account for the extended structure (i.e. no outer edge) seen in the scattered light of β Pictoris (Kalas & Jewitt, 1996) were also adequate to model the submillimetre image and SED, requiring an average grain size of 10 μm to fit the observed SED at longer wavelengths. The IRAS SED also implies the existence of a central cavity with a radius of approximately 30 AU (Backman & Paresce, 1993), although this is not observable in the submillimetre images with the resolution of the JCMT. Further submillimetre imaging of the β Pictoris disc confirmed the detection of a second region of emission $\sim$30 arc-seconds SW of the star (Dent et al., 2000). Holland et al. (1998) propose that this is either a fragmented part of the disc or possibly a second disc around a low-mass companion constrained to be <10 M_{Jup} . Dent et al. (2000) note that if this region was heated by β Pictoris then the dust mass would need to be 1.2 M_{lunar}, comparable to the mass of the primary disc, and this is unlikely as the feature does not appear in deep optical images. As discussed above, it is possible that this second region of emission is a background galaxy but it would be one of the brightest observed.

The higher contours in the image of Vega, show that it bears a resemblance to Fomalhaut in that it exhibits an elongated structure (Holland et al., 1998; Dent et al., 2000). Unlike Fomalhaut and β Pictoris, the lower contour levels of the Vega image show that the observed emission is roughly circular implying that the disc is being viewed close to face-on (Holland et al., 1998). Holland et al. (1998) also point out that the low observed rotation velocity of the star (Backman & Paresce, 1993) and optical spectroscopic observations of Vega (Gulliver et al., 1994) provide evidence that the star is also being observed at a low inclination angle. Also, the fact that the emission NE of the star is significantly brighter than the region SW of the star cannot be explained by simple axi-symmetric modelling and a non-uniform disc structure, observed pole-on is the favoured explanation (Dent et al., 2000). It is possible that a collision between two large bodies could have produced the dust observed (Holland et al., 1998), although dust created in this way is generally only expected to be observable for a few Myr due to collisional grinding (Wyatt & Dent, 2002). Dent et al. (2000) showed that the observed SED can be modelled by an isothermal modified black body and this suggests that the dust lies in a radially-thin ring and also implies that there is a limited range of grain sizes around Vega.

Sun-like Stars: ϵ Eridani and τ Ceti

Fomalhaut, β Pictoris and Vega are all A-type stars with ages <1 Gyr. Their ages span the equivalent to the "heavy bombardment" phase of the solar system, thought to have occurred up to $\sim$700 Myr after the Sun's formation (Greaves et al., 2005). However, their relatively short lifetimes ($\sim$1 Gyr) mean that any planets that formed will be short lived and that formation of life is unlikely to have taken place on these worlds. To gain a better understanding of how typical the solar system is, by comparison of the Kuiper Belt to the discs that surround other stars, a study of Sun-like stars is more relevant. The only nearby (within 5pc) single stars of similar spectral type to the Sun (G2V) are τ Ceti (G8V) and ϵ Eridani (K2V). Studies of these discs are of particular interest since ϵ Eridani at an age of 0.85 Gyr represents an analogue to the young solar system ("heavy bombardment" phase) and τ Ceti at an age of approximately 10 Gyr; an analogue to the future solar system. In the case of ϵ Eridani, a planet has been detected using radial velocity techniques by Hatzes et al. (2000).

Images of ϵ Eridani obtained using SCUBA (Greaves et al., 1998, 2005), show a ring of dust around the star with the emission peaking at a distance of around 65 AU and an outer edge at 105 AU. The best model fitted by Dent et al. (2000) to the SED and submillimetre image has a ring of dust 50-80 AU from the star, consistent with the observations of Greaves et al. (1998). The ratio of flux densities between the faint emission in the central cavity and the peak emission measured in the ring is approximately 2. The model (Dent et al., 2000) includes a central region with a dust density about 10% of that in the ring (radius > 50 AU) in order to fit the SED and submillimetre image. Measurement of the minor and major axes of the disc indicates that the spin axis is inclined at an angle of $25\pm3^{\circ}$ (Greaves et al., 2005) i.e. close to a pole-on orientation. Perhaps the most interesting feature observed in the ϵ Eridani disc is the clearly visible non-uniformity in the disc. As examined later in Chapter 3, this indicates that there may be an additional planet with a larger orbit than the one already discovered by radial-velocity techniques (Hatzes et al., 2000).

An 850 μm image of τ Ceti was obtained recently by Greaves et al. (2004b) using SCUBA at the JCMT. The image shows a region of emission around the star that appears symmetrical, orientated roughly N-S about the star. Greaves et al. (2004b) argue that the observed emission is unlikely to be from a distant background source since it is unlikely that a background object would be elongated symmetrically about the star. Measurement of the major and minor axes imply a close to edge on inclination angle of 60-90°, however it should be noted that the minor axis is not resolved (Greaves et al., 2004b). This did not agree with the stellar rotation velocity which implied a stellar inclination angle of 0-40° (Di Folco et al., 2004; Saar & Osten, 1997). Therefore, either the error in the stellar rotational velocities could be larger than estimated or the features observed could be evidence of non-uniform features present in the disc, similar to those observed in the Vega images (Holland et al., 1998). However, a more recent measurement by Valenti & Fischer (2005) gives a value of 1.3 km/s for $vsini$, implying an inclination angle for the star consistent with that determined from the disc. Since τ Ceti is a cooler star of spectral type G8V, imaging of these features will prove more difficult than the Vega case. The spectral energy distribution of the excess emission can be modelled by dust at a temperature of 60 K (Greaves et al., 2004b). Like the Vega case (Dent et al., 2000), a single temperature fit is evidence that the dust lies in a ring rather than a complete disc and that there is only a limited range of grain sizes.

1.1.2 Relative Sizes and Masses of the Discs

Data on both the stellar and disc parameters are shown in Table 1.1. The dust masses are typically a few M_{lunar} or less and this implies that any planet formation is complete in these systems (Dent et al., 2000). This is consistent with current planet formation theories in which the latter stages of terrestrial planet formation are expected to occur 10^7-10^8 years after the formation of the star (Chambers, 2004). Giant planets are expected to have formed within 10^7 yr based on core accretion models of planet formation (Hubickyj et al., 2005). The inner radii of the discs are generally slightly larger than the inner radius of ~30 AU estimated for the Kuiper Belt (Backman et al., 1995). As discussed later in this review the observable dust is now thought to originate from a collisional cascade (Wyatt & Dent, 2002). Since large bodies would not contribute to the observed flux the dust mass only represents a small fraction of the total disc mass. Collisional lifetime arguments can be used to estimate the total mass of the disc (Wyatt & Dent, 2002). Generally, there is a decline of dust mass with time (Rieke et al., 2005), but Habing et al. (2001) note that not all young stars have a disc and not all old stars have lost theirs, e.g. τ Ceti. A comparison between the dust mass in the solar system and around the stars ϵ Eridani and τ Ceti is most interesting since these stars are of spectral type similar to the Sun.

The dust mass estimate for the τ Ceti disc is around 5% that of the ϵ Eridani disc and this is in agreement with models suggested by Kenyon & Bromley (2004) and Spangler et al. (2001) that the dust mass decreases sharply with time (t^{-1} to t^{-2}). In order to fit the decline of dust mass with time, the solar system, at its age of 4.5 Gyr, would have to contain a dust mass of at least 10^{-4} $M_{\oplus}$, but curiously this is two orders of magitude higher than estimates for the dust mass in the Kuiper Belt (Fixsen & Dwek, 2002; Landgraf et al., 2002). In addition to this, a lower comet population implies a lower collision rate and therefore less dust mass in the disc and the mass of comets in the Kuiper Belt is an order of magnitude less than that estimated for the τ Ceti collisional cascade.

There are two theories that attempt to explain why the Kuiper Belt has less mass than that estimated for the τ Ceti disc. The first postulates that the density of the Kuiper Belt is already mysteriously low if the density of the protoplanetary disc out of which the planets are thought to have formed is extrapolated out to approximately 50 AU (Morbidelli et al., 2003). It is possible a close stellar encounter could be responsible for ejecting many of the original comets but this type of event is reasonably rare. The second theory proposes that the region in which the Kuiper Belt now resides may have originally been unpopulated and became populated by bodies pushed outwards by the migration of Neptune. Slower and smoother migration increases the population pushed outside of a migrating planet. In the case of τ Ceti it may simply be the case that a Neptune-like planet had slower and smoother migration than that which occurred in our own solar system or that the initial number of bodies outside the orbit of the planet was greater. However, this second theory requires the initial protoplanetary discs to be less than 50 AU and this is not observed in the ϵ Eridani disc which extends out to 105 AU and primordial dust discs frequently exceed this (Kitamura et al., 2002).

1.1.3 Origin and Composition of Grains in the Disc

After the original discovery of the far-infrared excess from Vega, Aumann et al. (1984) concluded that the particles emitting the radiation must be a remnant of the protoplanetary disc from which Vega formed. This was because there was no evidence of any mass loss from Vega and particles from the interstellar medium, regions of current star formation and circumstellar dust grains are small enough (radii < 9 μm) to be ejected by radiation blowout. Furthermore, particles could be removed via Poynting-Robertson drag. In this process, photons from the star preferentially strike the leading side of the grain and the radiaton absorbed is re-radiated in all directions, eventually slowing the particle down enough that it will spiral into the star (Backman & Paresce, 1993). Particles with radii < 12 cm would spiral into the star on timescales of the order of the lifetime of Vega. Therefore, Aumann et al. (1984) argued that the particles that remained in the disc must be larger than 120 mm in diameter and probably grew from material in the initial protoplanetary disc.

However, the collisional timescales for grains in debris discs are generally much shorter than the timescales for removal by the Poynting-Robertson effect (Dent et al., 2000; Wyatt, 2005). The velocities of the grains in the disc are such that the collisions are destructive rather than lead to growth of particles (Backman & Paresce, 1993; Wyatt & Dent, 2002). Most of the resulting fragments from the collisions are small enough to be ejected from the disc by radiation pressure from the star (Backman & Paresce, 1993). Dent et al. (2000) suggest that the dust is likely to be continually replenished by a collisional cascade, in which large bodies are ground down to ever smaller sizes through a series of collisions. A debris disc is observable because of the large quantities of small grains created from this collisonal cascade which give a larger surface area from which radiation can be emitted (Wyatt & Dent, 2002). The dust can be replenished as long as there is a reservoir of parent bodies present in the disc to initiate the cascade (Wyatt & Dent, 2002).

The spectral energy distribution is characterised by the spatial distribution, size distribution and composition of the grains (optical properties) that reside in the disc (Wyatt & Dent, 2002). Therefore SED modelling can yield information about the properties of the dust in a debris disc and Fomalhaut has been the most studied disc in this respect (Holland et al., 2003; Wyatt & Dent, 2002).

The spatial distibution of the dust and modelling of the Fomalhaut disc's SED by Wyatt & Dent (2002) was able to constrain the size distribution and this was inferred to be consistent with a disc in collisional equilibrium. A similar analysis was not able to accurately determine the composition of the grains, although the best fit was for non-porous grains similar to the core-mantle model developed by Li & Greenberg (1997) for interstellar grains. This model assumes that the dust grains consist (by volume) of 1/3 aggregate silicate core and 2/3 organic refractory mantle of UV photoprocessed ices that accreted on to the core in the interstellar medium. Sheret et al. (2004) used the core-mantle model to remodel debris discs SEDs and found that while Vega and Fomalhaut required solid dust grains to model their SEDs, other stars (HR 4796 and HD 141159) could only have their SEDs fit using porous grains. Sheret et al. (2004) also found that older stars tended to have less porous grains than younger stars and suggested that this may indicate that collisions in the discs may have reprocessed the grains into a more solid form.

An initial study using 850 μm data used a single grain size of 100 μm at a temperature of 45 K to model the SED of Fomalhaut's disc (Dent et al., 2000), although it was already known that a variety of grain sizes was needed to fully model the SED of Fomalhaut (Zuckerman & Becklin, 1993). More recent and detailed SED modelling has shown that Fomalhaut's disc grain size distribution is consistent with a collisional cascade with bodies ranging in size from 7 μm to 0.2 m in diameter (Holland et al., 1998; Wyatt & Dent, 2002). The upper limit of 0.2 m corresponds to the maximum diameter grains that contribute to the 850 μm flux and below diameters of 7 μm, particles are expected to be blown out of the system by radiation pressure (Wyatt & Dent, 2002). The temperature of grains is dependent on the location in the system (i.e. the distance from the star) and also the grain size; smaller grains will be warmer than larger grains at the same location (Holland et al., 2003). Collisional lifetime arguments also imply that the material now observed originated from a cascade initiated by the break-up of planetesimals up to 4 km in diameter implying a total disc mass of 20-30 $M_\oplus$ (Wyatt & Dent, 2002).

The SEDs of the debris discs around Fomalhaut, Vega, β Pictoris and ϵ Eridani were modelled using a single grain size by Dent et al. (2000) and found to have grain sizes 10-100 μm, opacity indices (a measure of how efficiently the grains re-emit absorbed radiation) between 0.8 and 1.1 and temperatures of 35 to 80 K. Dent et al. (2000) also note that there is not a large range of temperature within any one disc. Greaves et al.

(2004b) showed that for τ Ceti, the 60 to 850 μm SED could be fit with grains of a similar temperature of 60 K and an opacity index 0.5, slightly lower than those inferred by Dent et al. (2000). Opacity indices close to zero imply the presence of grains that are closer to blackbodies and much larger than interstellar grains (Greaves et al., 2004b).

1.1.4 Clearing of the Central Cavity

All of the discs discussed in this review exhibit evidence of a central cavity with radii ranging between 20 and 100 AU (Dent et al., 2000). In the case of Vega and τ Ceti this is inferred from the results of modelling the SEDs (Dent et al., 2000; Greaves et al., 2004b). This is because a single temperature fit means the dusty debris must only lie within a particular range of radii from the star and so forms a ring structure around the star with a distinct inner and outer edge. In the case of Fomalhaut (Holland et al., 2003) and ϵ Eridani (Greaves et al., 2005) the presence of the cavities can also (in addition to SED modelling) be clearly seen in the submillimetre images as regions where the radiation is significantly fainter than the peak radiation in the disc. Evidence for a central cavity in the β Pictoris disc, has been obtained from the IRAS SEDs (Backman & Paresce, 1993) and further modelling of the SED by Dent et al. (2000) shows that β Pictoris must have a radially extended disc with a power-law density distribution and therefore is the only disc to have no distinct outer edge.

Radiation pressure, Poynting-Robertson drag, grain mantle sublimation, grain collisions and interactions with a larger body are all mechanisms capable of removing grains from the inner radii of a debris disc (Dominik & Decin, 2003). These are each discussed in the paragraphs below.

A "blowout" size can be determined for each star, representing the minimum size of grains released at rest that are stable against ejection by the radiation pressure from the star (Backman & Paresce, 1993). Burns et al. (1979) showed that grains are not easily removed in the case of the solar system. More generally, radiation blowout is only considered important for removing small grains (less than a few μm in size) around high luminosity stars (Backman & Paresce, 1993). Even then, it cannot produce the abrupt inner boundary observed in the debris discs (Dent et al., 2000).

The Poynting-Robertson (P-R) effect can cause grains that are stable against radiation pressure blowout to spiral in towards the star (Backman & Paresce, 1993). However, the timescales on which this process occurs are much larger than the age of the star in the cases of Fomalhaut and ϵ Eridani. For the case of ϵ Eridani, particles with diameters of approximately 1 mm would only be cleared out to a radius of about 15 AU (Jura, 1990) in around 1 Gyr and so cannot explain the clearing out to $\sim$35 AU (Greaves et al., 1998). Also, P-R drag would produce a 1/r density distribution if it was the dominant mechanism resonsible for grain removal and this is not observed (Dent et al., 2000).

Sublimation of the icy grain mantles could produce an abrupt inner boundary but ice sublimation is a very strong function of temperature (Backman & Paresce, 1993) and is only really important for T > $\sim$100 K (Moro-Martín & Malhotra, 2002). The debris discs observed are generally too cold for this to be the dominant process (Dent et al., 2000). Melting of the mantles requires even greater temperatures of $\sim$170 K and this "snow-line" occurs at 2.7 AU for Sun-like stars and at even smaller distances for dusty protoplanetary discs (Sasselov & Lecar, 2000). For example, ϵ Eridani has a luminosity of about 0.33 $L_{\odot}$ (Soderblom & Dappen, 1989) and since the gas giants in the solar system are expected to have formed around icy cores, ice mantles would be expected to persist to within a few AU of the star (Greaves et al., 1998). Dent et al. (2000) also note that there is too much variation between the temperatures of each disc for grain sublimation to be the primary process for removing grains.

The central cavity was previously thought to be cleared due to the growth of particles into larger bodies (Aumann et al., 1984; Greaves et al., 1998), since smaller grains would be removed by radiation blowout and P-R drag and larger bodies would emit less radiation per unit mass than smaller grains. However, timescales for grain-grain collisions are significantly smaller than those for the P-R effect and therefore collisions dominate the grain removal process (Dent et al., 2000). Since the collision timescales are so short, and the shattered grains will be removed by radiation blowout or P-R drag then the grains must be replenished by a collisional cascade (Wyatt & Dent, 2002). Dent et al. (2000) propose that there is a critical grain size (approx. a few mm in all cases) which survives for the lifetime of the star and can then act as a reservoir of larger grains that replenishes any grains removed from the disc via a collisional cascade.

It was expected that a planet could contribute to the clearing of a central cavity by ejecting grains that spiral inwards near its orbit (Greaves et al., 2005). Dent et al.

(2000) argued that a massive body sweeping up the grains at the inner radius of the ring is the most convincing explanation for the presence of the central cavity. Roques et al. (1994) found from numerical situations that a planet of $\sim$5$M_\oplus$ at the inner edge of the ring can prevent the inward migration of dust slowed by Poynting-Robertson drag and create a stable central cavity and an abrupt outer edge. Later work by Wyatt (2005) showed that P-R drag is an insignificant process because collisions between planetesimals occur on much shorter timescales and result in the planetesimals being ground into dust which is fine enough to be removed by radiation pressure before P-R drag has a chance to act.

1.1.5 Evidence for Planets

Non Uniformity of the Ring

Dent et al. (2000) note that the Vega and ϵ Eridani discs have observable bright spots which can be interpreted as dust density enhancements. Dent et al. (2000) also state that for Fomalhaut and β Pictoris such "clumps" would be hard to observe since the discs are observed edge-on. However, more recent observations of Fomalhaut at 350 μm (Marsh et al., 2005), and 450 μm and 850 μm (Holland et al., 2003) have shown that the disc is not axi-symmetric and there is at least one "clump" or arc emitting $\sim$5% of the total flux of the disc. The most obvious non-uniformity observed thus far is that of the ϵ Eridani disc for which there is also a new 450 μm image (Greaves et al., 2005). As discussed previously, the 5 year dataset at 850 μm has shown that some of the features previously observed in the disc are stationary with respect to the sky and are therefore unlikely to be physically associated with the star.

A study of collisonal processes in the disc by Wyatt & Dent (2002) showed that a collision between two runaway planetesimals (>1400 km in diameter) could produce enough dust to account for the observed clump in Fomalhaut's disc. However, for the dust to still be observable the ignition of the collisional cascade would have had to occur in the last few Myr (Wyatt & Dent, 2002). Wyatt & Dent (2002) note that this estimate is limited by uncertainties in both the frequencies and the outcomes of collisions between runaway planetesimals and does not rule out a collisional origin for some of the bright spots observed in other debris discs.

A second and more plausible explanation is that $\sim$5% of the planetesimals in the

Fomalhaut ring are caught in a 1:2 gravitational resonance with a planet migrating outwards (Wyatt & Dent, 2002). Numerical simulations by Roques et al. (1994) showed that dust could be trapped in outer mean motion resonances on timescales comparable with the P-R drag lifetimes of the grains. Dent et al. (2000) note that this provides a credible explanation for the density enhancements seen in the Vega and ϵ Eridani rings. Greaves et al. (2005) also argue that for the ϵ Eridani case the only convincing explanation for the ring's sub-structure is gravitational perturbation by a second planet at tens of AU from the star. However, this was based on the models of Ozernoy et al. (2000); Quillen & Thorndike (2002) which require inwardly migrating dust slowed by P-R drag to get caught in the planet's resonances which as discussed earlier may be removed from the system by the action of collisions and radiation pressure. An alternative explanation, presented by Wyatt et al. (2003), is that the dust can also be trapped in resonances when a planet migrates outwards. Dust trapped in a resonance would orbit the star with the planet and should be observable on a timescale of a few years (Wyatt & Dent, 2002). Greaves et al. (2005) also tentatively suggest a counter-clockwise rotation of the ϵ Eridani disc of 1 degree per year, although recognising that a higher resolution image or extended period of observation may be required to prove the rotation (only a 5 year dataset so far) and this is examined in more detail in Chapter 3.

Searches for Debris Discs around Stars with Planet Detections

Greaves et al. (2004a) performed a survey of stars, searching for debris discs around stars with known giant planets, discovered using radial-velocity techniques. No more debris discs were observed and this implied that the stars included in the survey did not have debris discs with dust masses larger than 0.02 $M_{\oplus}$. At the time, an inverse survey of stars with known debris discs showed that only ϵ Eridani had a planet detection by the radial-velocity method. However, very few of the stars observed in this survey had mid-infrared excesses and this implied the existence of central cavities in the discs. As discussed previously, it has been argued that the central cavities are cleared by planets (Roques et al., 1994) at orbits of 5 to 40 AU that are not detectable by current radial-velocity techniques and so it appeared that there may be two groups of stars with different planet locations. However, Wyatt (2005) showed that planetesimals in the disc can be ground into dust and removed by radiation pressure and thus the central cavity can be created this way. Subsequent

Spitzer surveys have also revealed more stars with both detectable planets and debris discs (Beichman et al., 2005).

If two groups of stars with different planet locations do indeed exist, Greaves et al. (2004a) proposed that these systems evolved very differently because the time-scales in which planets form vary in each system. Whilst many properties of the initial disc will affect the timescale on which planets form, the most important factor is the initial disc mass, to which the timescale is inversely proportional (Kenyon & Bromley, 2002). In addition, observations have shown that initial disc mass may vary by as much as two orders of magnitude (Wyatt et al., 2003). In low mass discs, the planetary cores would grow more slowly and would not have accreted much gas by the time the gas in the disc had dispersed, around 10 Myr after the formation of the star (Bary et al., 2003; Thi et al., 2001). These partially formed planets will then migrate to larger orbits via angular momentum exchange with smaller planetesimals on larger orbits. Conversely, high mass discs allow gas giants to form rapidly and these will migrate inwards because the disc will remain gas-rich for the first few Myr (Nelson et al., 2000). In the inward migrating systems the outer planetesimals will also form relatively quickly and through collisional grinding will not be visible soon after the star has formed due to drag forces removing the dust (Dent et al., 2000). However, for the outward migrating systems, Liou & Zook (1999) showed that the systems could evolve to have planets on large orbits that clear central cavities in the disc. This explanation can also account for the non-uniformity of some of the debris discs observed (Wyatt et al., 2003).

1.1.6 Summary

Habing et al. (2001) found the incidence of debris discs around stars relatively close to our Sun to be ~17%, using 60 μm data from ISO and Bryden et al. (2006); Trilling et al. (2008) found a similar value for a sample of sun-like stars (16%). The most striking features of the debris discs observed are the cleared central cavities that seem to be common to all the discs and the sub-structure observed in some of the rings. The most plausible explanation for the clearing of central cavities is the collisions of planetesimals grinding themselves into dust which is then removed by radiation pressure. The clumps observed in some debris discs like ϵ Eridani can be explained by the presence of planets orbiting the host stars migrating outwards, trapping the dust into mean motion resonances. These star systems all have more dust mass than the best estimates for the Kuiper Belt, even around the 10 Gyr-old star of τ Ceti. It would be difficult for life to form in these systems since any planets would be subject to bombardment by comets, similar to the heavy bombardment phase that is thought to have occurred in the early solar system. However, the 1.7 M_J planet orbiting ϵ Eridani (Hatzes et al., 2000) is likely to be more efficient than Jupiter at ejecting comets on Earth-crossing orbits from the system (Horner & Jones, 2008).

Presently, the fraction of stars with planetary systems is estimated to be 12-15% (Fischer et al., 2003; Marcy et al., 2005). The stars with detectable planets and debris discs only represent about 30% of the nearby stellar population, neglecting the overlap between the two samples. The most exciting discoveries may be found in the other ~70% of stars for which there are no detections of planets or debris discs. Greaves et al. (2004a) pointed out that the Sun belongs to this group of stars. This is because the giant planets are situated in the outer solar system and so would be hard to detect using radial-velocity techniques and the Kuiper Belt contains less dust in it than the debris discs discussed here.

1.2 Star Formation

1.2.1 Fundamental Concepts

Since our Galaxy is estimated to be 10 billion years old, the very fact that we observe O type stars with main sequence lifetimes of less than 3 million years implies they must have formed recently on Galactic timescales. This assertion is supported by radio observations that show that OB stars are most often located within dense clouds of gas and dust, presumably out of which they formed.

Stars form in Giant Molecular Clouds (GMCs), the majority of which are located in the spiral arms of our Galaxy. GMCs are made up of mostly molecular hydrogen H_2. Observations of emission lines can be fit with a Gaussian profile to determine a distribution of velocities, I(v):-

$$I(v) = e^{-v^2/2\sigma^2} \tag{1.1}$$

where σ is known as the velocity dispersion. From this it can be determined if clouds are gravitationally bound and so may form stars if they condense further.

Stars form when a clump of gas and dust in a molecular cloud collapses under its own gravity. In the most simple case the gravitational attraction of the system must overcome the gas pressure of the clump. For a system in virial equilibrium the total potential energy, E_P is exactly twice the kinetic energy, E_K:-

$$E_P + 2E_K = 0 \tag{1.2}$$

If $E_P + 2E_K < 0$ the clump will collapse but if $E_P + 2E_K > 0$ then the clump will expand, assuming a nonmagnetic, isothermal, infinite, homogeneous self-gravitating medium with no turbulence (Mac Low & Klessen, 2004). From stability analysis Jeans (1902) derived a dispersion relation for small perturbations:-

$$\omega^2 - c_s^2 \left(\frac{2\pi}{\lambda}\right)^2 + 4\pi G\rho = 0 \tag{1.3}$$

where ω and λ are the oscillation frequency and wavelength, respectively, c_s is the isothermal sound speed, G is the gravitational constant and ρ is the density. Equation 1.3 describes the propagation of sound waves through the medium under the influence of self gravity, for which gravitational collapse will overcome the acoustic restoring force for perturbations with wavelengths greater than the Jeans length, λ_J:-

$$\lambda_J = \sqrt{\frac{\pi c_s^2}{G\rho}} \tag{1.4}$$

Assuming a spherical perturbation with radius equal to the Jeans length, there exists a minimum mass, the Jeans mass, M_J, above which the gravitational collapse will overcome the thermal pressure of the gas contained within the clump:-

$$M_J = \frac{4\pi}{3}\left(\frac{\lambda_J}{2}\right)^3 \rho = \frac{\pi}{6}\left(\frac{\pi}{G}\right)^{3/2} c_s^3 \rho^{-1/2} \tag{1.5}$$

Equation 1.2 is the virial theorem for an isolated body in hydrostatic equilibrium. For a spherical clump of self gravitating, isothermal ideal gas, of radius, r, with an external surface pressure P_{ext}, the virial theorem becomes:-

$$E_P + 2E_K = 4\pi r^3 P_{ext} \tag{1.6}$$

Bonnor (1956) and Ebert (1957) derived the largest possible mass of this sphere of gas in a pressurised medium, whilst still being in hydrostatic equilibrium:-

$$M_{BE} = 1.18 \frac{\sigma^4}{(G^{3/2} P_{ext})^{1/2}} \tag{1.7}$$

where M_{BE} is the Bonnor & Ebert mass and σ is the velocity dispersion. Clumps of gas with masses greater than the Bonnor-Ebert mass will become dynamically unstable to gravitational collapse. A maximum radius, R_c, below which size a clump is gravitationally unstable is given by:-

$$R_C = 0.41 \frac{G M_{BE}}{\sigma^2}. \tag{1.8}$$

The Jeans mass is greater than the mass contained within a Bonnor-Ebert sphere with the same surface conditions because the latter assumes that the clump is more dense than the surrounding material but only part of the mass contained within a Jeans length will collapse. The Jeans mass represents the critical mass that must accumulate before a clump of gas will undergo gravitational collapse. The Bonnor-Ebert mass is able to take account of the high pressures found in GMCs.

Classical Dynamical Theory

The classical dynamical theory of star formation was developed based on the balance between pressure gradients and gravitational collapse and included micro-turbulence but only as an addition to the thermal pressure by modification of the effective sound speed. It did not account for conservation of angular momentum or magnetic support during collapse. This became a problem when the presence of magnetic fields in the Interstellar Medium (ISM) was detected through observations of polarised starlight (Hiltner, 1949, 1951; Chandrasekhar & Fermi, 1953).

If a cloud's mass is greater than the critical mass, M_C, required for gravitational collapse to overcome the magnetic repulsion, then it is termed supercritical and if not it is termed subcritical. From measurements of the magnetic field from Zeeman splitting of the HI (atomic hydrogen) line (Troland & Heiles, 1986) and from measurements of pulsar rotation and dispersion (Rand & Kulkarni, 1989; Rand & Lyne, 1994), M_C was measured to be 4×10^6 $M_\odot$.

Another problem encountered was that the free-fall timescales predicted by this model were orders of magnitude faster than the typical ages of galaxies which led to an overestimation of the star formation rate. Also, conservation of angular momentum predicted rotation periods of under a second for stars when observations of solar-type stars showed rotation periods of the order of tens of days. Mac Low & Klessen (2004) point out that the resulting centrifugal force from this fast a rotation exceeds the gravitational force by eight orders of magnitude so is clearly unphysical. Finally, the detection of bipolar outflows from young stars by Snell et al. (1980) provided part of the solution to the angular momentum problem and Konigl & Pudritz (2000) showed that magnetic fields transfer the angular momentum from the infalling gas to outflowing gas.

Standard Theory of Isolated Star Formation

Mestel & Spitzer (1956) were the first to argue that the magnetic repulsion problem could be overcome by movement of neutral gas across the field lines. This process of ion-neutral drift is known as ambipolar diffusion and allows the local density to increase and therefore lower the value of M_C. The dynamical timescale associated with ambipolar diffusion was also found to be 10-20 times longer than for standard gravitational collapse which helped explain the observed star formation rates. The angular momentum problem was also explained by magnetic tension acting to brake rotating cores.

On the basis of ambipolar diffusion as a dominant physical process, Shu (1977) argued that a singular isothermal sphere in a magnetically subcritical cloud core can develop with a radial density distribution of the form $\rho \propto 1/R^2$. The core should collapse on timescales of the order of the ambipolar diffusion timescale and eventually lead to inside-out collapse with the central region collapsing and accreting before the envelope. As the central region undergoes free-fall collapse the density takes the form $\rho \propto 1/R^{3/2}$, with a free fall speed, $v^2 = -GM/R$. As the inner region collapses an expansion wave moves outward and this transfers mass to the inner region. In this model the accretion rate is equal to $4\pi R^2 \rho v$ and is therefore independent of R and remains constant with time.

This standard theory of star formation was widely accepted during the 1980s but more recently several problems have arisen. Firstly, there are a number of theoretical flaws in the theory: If the ratio of densities at the centre and the surface of the sphere is greater than 14, then a stable equilibrium state cannot be reached and the collapse of the cloud will occur before the $1/R^2$ density distribution can be established (Whitworth et al., 1996; Silk & Suto, 1988; Hanawa & Nakayama, 1997). The symmetry in the inner region of the sphere is also broken by external perturbations so this tends to flatten the density profile. The mass actually moves to the centre of the sphere by ambipolar diffusion in the outer envelope and not by the expansion wave as initially thought. The collapse of a core with a $1/R^2$ density profile also tends to form single objects in preference to binary or multiple systems but most stars form as part of a multiple system (Mathieu et al., 2000; Whitworth et al., 1996).

Secondly, more powerful observation techniques in the 1990s were able to expose further problems with the standard theory. In particular, Nakano (1998) stated that the magnetic field strengths measured in molecular clouds are not actually strong enough to create a magnetically subcritical situation; the previous measurements taken in the 1970-80s were too inaccurate for this to be apparent. Also, the model predicts that the inner part of the core should collapse while the outer envelope remains in place, but mapping in optically thick and thin lines show that the infalling material is too extended to be consistent with inside-out collapse (Tafalla et al., 1998; Williams et al., 1999). The density profiles observed are flat and do not fit the $1/R^2$ structure as predicted by the Shu model. The ages of clumps in molecular clouds measured from observations of chemical abundances are of the order of 10^5 years (van Dishoeck et al., 1993; van Dishoeck & Blake, 1998; Langer et al., 2000) compared to the ambipolar diffusion timescale of 10^7 years.

Observations of protostellar accretion rates do not remain constant but in fact decrease with time. The number of stars in cores indicates that the time for the cores to evolve in the prestellar phase is similar to the length of time spent in the accretion phase. This is in disagreement with the standard model which predicts that the core evolves at the prestellar phase on ambipolar diffusion timescales which are an order of magnitude longer than the dynamical timescales of the accretion phase. Finally, the range of ages of stars in clusters should be much larger than the dynamical timescale if the cores are contracting on ambipolar diffusion timescales, yet in fact the spread of ages is closer to the dynamical time.

The most recent model of star formation presented by Mac Low & Klessen (2004) is based on the work of Larson (1981) and finds that supersonic turbulent flow can support a core from collapse enough to slow the star formation rate but still allow gravitational contraction to take place. The supersonic turbulence can create density fluctuations that result in the formation of dense clumps and filaments. The turbulence decays rapidly and requires driving by either supernovae or galactic rotation but operates either with or without a magnetic field present. Magnetic fields weaker than the subcritical level are capable of reducing the collapse rate but are not able to stop it completely but may still transfer angular momentum if coupled to the gas.

This latest theory addresses many of the inconsistencies associated with the standard model and since the rate of local collapse depends on the strength of the turbulence it also provides an explanation for the varied star formation rates observed.

1.2.2 Observational signatures of star formation

Evolution of Protostars on the HR Diagram

A Hertzsprung-Russell (H-R) diagram for nearby stars can be constructed by plotting their bolometric luminosities against the effective temperature, T_e, of the star, which is the surface temperature of the star assuming that it is radiating as a blackbody. It is related to the luminosity, L_S and the radius, R_S of the star by:-

$$T_e = (L_S/\sigma 4\pi R_S^2)^{1/4} \tag{1.9}$$

where σ is Stefan's constant. The majority of stars lie within a band in the diagram known as the main sequence. The fact that most stars occupy this region of the diagram is consistent with the fact that stars spend most of their lives in hydrostatic equilibrium, fusing hydrogen into helium via the proton-proton chain to produce the necessary pressures to combat gravitational collapse and maintain hydrostatic equilibrium.

Joy (1945) identified a new type of star which was later named after the first star observed of this type, T Tauri. T Tauri stars are normally located in dense clouds of gas and dust which means they have to be observed in the IR since the visible light is scattered by dust and re-radiated in the IR. They have unusually large amounts of lithium in their atmospheres which is utilised during nuclear fusion in stellar interiors. The large amounts of lithium apparent in the surface of T Tauri stars is therefore evidence of surface activity and indicates that the stars are very young. T Tauri stars are also expected to have strong chromospheric activity since their spectra usually include strong emission lines as well as evidence for strong stellar winds and their brightness can vary on timescales of only a few hours.

The abnormal spectra and the fact that computing bolometric brightnesses requires the addition of the IR excesses to the optical fluxes makes construction of H-R diagrams for T Tauri stars difficult but was done by Strom (1977); Cohen & Kuhi (1979). T Tauri stars are positioned above the locus occupied by Population I, zero age main sequence (ZAMS) stars on the Hertzsprung-Russell (H-R) diagram.

Assuming the envelope of a protostar remains radiative, then its luminosity is limited by the photon diffusion rate and it can be shown for low to medium mass, M, stars (Shu, 1982) that:-

$$L \propto M^{5.5}/R^{0.5} \tag{1.10}$$

which means for a contracting protostar the luminosity will increase slowly with decreasing R. Henyey et al. (1955), Hayashi et al. (1962); Hayashi (1966) and Larson (1969) constructed horizontal radiative evolutionary tracks assuming a protostar contracted gradually through a progression of radiative states with decreasing radii as shown in Figure 1.2. Hayashi & Nakano (1965) showed that below a certain temperature the photospheric layers of a star lose their ability to prevent the free streaming of photons. This leads to an increase in the luminosity in the envelope beyond that which can be carried outward by radiative diffusion and therefore the envelope will be become convective. Therefore, there is a minimum temperature and therefore a maximum radii above which the protostar must follow a vertical evolutionary track on the H-R diagram. The combination of the convective and radiative tracks results in the Henyey-Hayashi evolutionary tracks shown in Figure 1.2. Gaustad (1963) argued that the contraction of a protostar could not proceed gradually and at some point the support from thermal pressures would be lost quickly due

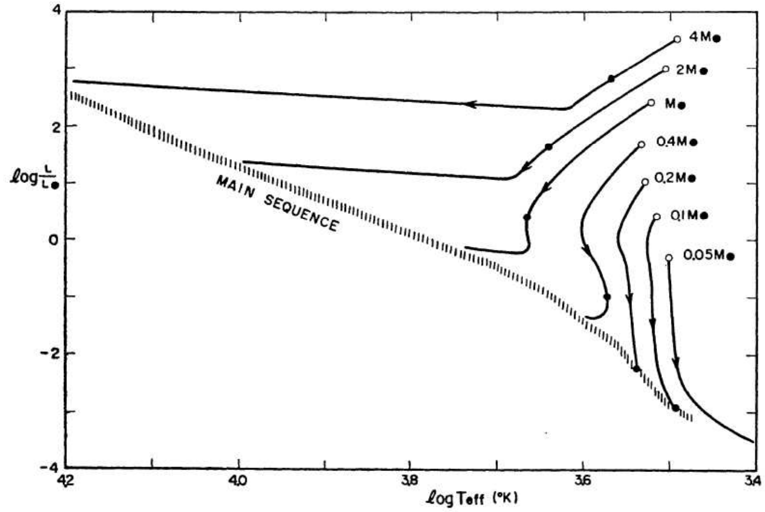

Figure 1.2: Theoretical evolutionary Hayashi-Henyey tracks for stars of various masses between 0.05-4 $M_{\odot}$ under going quasi-hydrostatic collapse. (Figure from Hayashi (1966))

to the high efficiency of radiative transfer leading to a stage of rapid dynamical collapse. Numerical calculations have shown that after this rapid dynamical collapse, low-medium mass stars will appear on the convective part of the Henyey-Hayashi tracks. This means that young stars that have recently formed out of material from their parental molecular cloud will generally be located above the main sequence stars on the H-R diagram and is consistent with the notion that T Tauri stars are pre-main sequence stars.

Since young stars are often enshrouded in dusty envelopes or located in embedded clusters, the light from the young stars is subject to extinction and the youngest stars are invisible at optical wavelengths. Therefore, measuring their luminosities is extremely difficult. Since much of the emission is reprocessed by the surrounding dust and re-radiated at longer wavelengths, the SED does not resemble a blackbody and so determining a temperature is not possible. This means that it becomes extremely difficult to place young stars on a H-R diagram and so a more effective means of classifying YSOs is required.

Classification of Protostars & Pre-Main Sequence Stars

Giant molecular clouds are the sites of active star formation. As discussed later in Section 2.1 these clouds are opaque when observed at optical wavelengths but observations at longer wavelengths in the near and far infrared allow us to detect the radiation from the dust. Recent surveys of nearby clouds show that 70-90% of stars appear to form in embedded clusters which are heavily obscured by dust and are therefore most effectively observed at infrared wavelengths (Lada & Lada, 2003).

Planck's law gives the spectral radiance, B_λ as a function of wavelength, λ, emitted from a blackbody of temperature T using:-

$$B_\lambda = \frac{2hc^2}{\lambda^5}\frac{1}{e^{hc/\lambda kT} - 1} \tag{1.11}$$

where h is Planck's constant, k is the Boltzmann constant and c is the speed of light in a vacuum. Planck's law can also be written as a function of frequency, ν:-

$$B_\nu = \frac{2hv^3}{c^2}\frac{1}{e^{h\nu/kT} - 1} \tag{1.12}$$

where B_ν is the spectral radiance as a function of frequency.

Dust grains are not perfect blackbodies and the spectral radiance, $S_\nu(T)$, emitted by dust grains in circumstellar discs and cool clouds of temperature, T, is actually fit by a modified blackbody (greybody) curve:-

$$S_\nu(T) \propto B_\nu(T)\nu^\beta \tag{1.13}$$

where B_ν(T) is the blackbody intensity and β is the index giving the frequency dependence of the emissivity $Q(\nu)$, varying between 1 and 2 (Hildebrand, 1983).

The spectral index α_λ is measured using the slope of the spectral energy distribution (SED), measured as λ S_λ between 2 and 20 μm:-

$$\alpha_\lambda = \frac{d(log\lambda S_\lambda)}{d(log\lambda)}. \tag{1.14}$$

For a perfect blackbody α_λ has a value of -3 for high frequencies (hν/kT $\ll$ 1), but the dusty discs and envelopes around a Young Stellar Object (YSO) reprocess the light from the star to longer wavelengths. Thus, emission at infrared wavelengths that exceeds that expected for a standard stellar photosphere is an indication of youth. The dust appears on the SED as a superposition of greybody curves since the dust radiates at a range of temperatures.

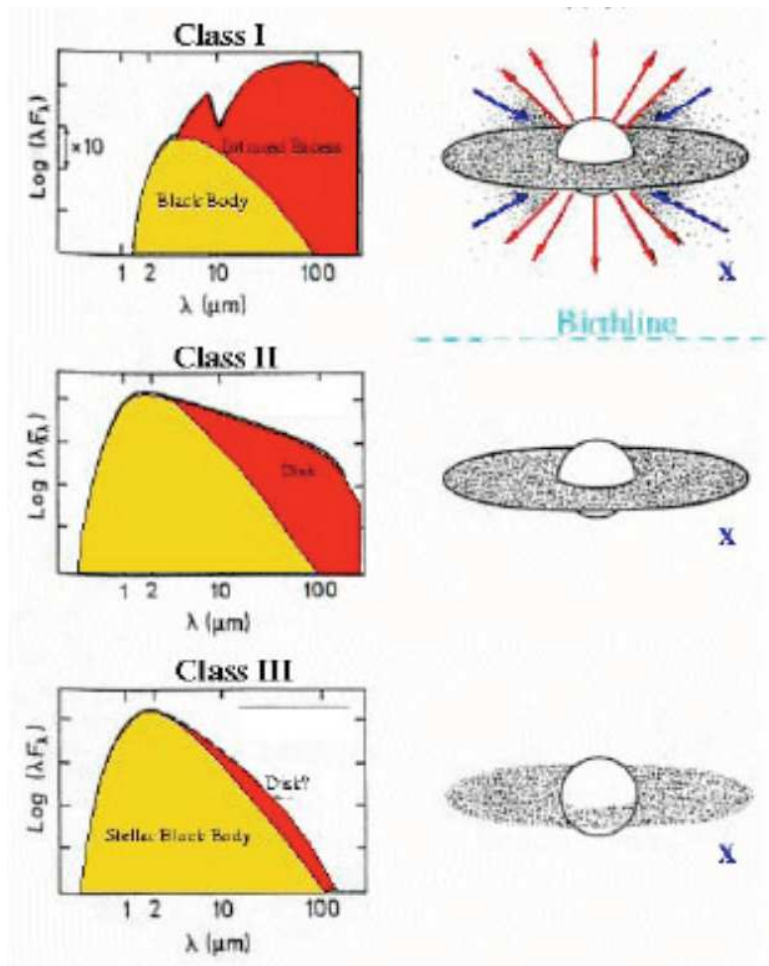

Figure 1.3: Schematic of SED models associated with Class 1 (Envelope), Class II (Disc) and Class III (Remnant Disc) objects. Credit: adapted from C. Lada, P. Andre, M. Barsony, D. Ward-Thompson.

A basic classification scheme for low mass protostars was established by Lada & Wilking (1984) and Lada (1987) in which stars were labelled from Class I (envelope accretion) to III (remnant disc) and later with the addition of Class 0 (early collapse) (Andre et al., 1993) based on the value of α_λ from their SEDs as shown in Figure 1.3. Class 0 and I sources are usually referred to as protostars whilst Class II and III sources are referred to as pre-main sequence stars and the features of each class are briefly discussed below.

Class 0 sources

Class 0 sources are embedded in and surrounded by circumstellar material so that their SEDs peak at around 100μm and are often not observable at wavelengths below 20μm. Their SEDs resemble a single temperature cold blackbody with a temperature ranging between 20 and 70 K. All known Class 0 sources are associated with bipolar outflows, another sign of youth.

Class I sources

Class I sources have SEDs which peak in the far infrared with $\alpha_\lambda > 0$ and are broader than a single temperature blackbody implying that the large infrared excess originates from dust at a range of temperatures. The absorption feature seen at 10 μm is due to silicate dust and this implies that the radiation observed is being emitted mostly from dust. Class I sources are believed to be young protostars with an infalling envelope; this is because the infrared excess is emitted by warm dust close to the star which would be blown away by radiation pressure if no infalling material was present. Infalling envelopes can be detected directly by observing an attenuated red wing compared to the blue wing of spectral lines detected near protostellar cores (Peretto et al., 2006).

Class II sources

Class II and III sources have SEDs which peak in the near infrared. Class II sources have broad SEDs with -2 $< \alpha_\lambda <$ 0, there is an infrared excess but not as large as is present for Class I sources and no 10 μm silicate absorption feature is visible. This implies that these sources are not as embedded as Class I sources and only a disk is present with no infalling envelope. Class II sources are generally identified as Classical T Tauri (CTTs) stars when observed in the optical from their strong emission lines Joy (1945).

Class III sources

Class III sources have SEDs with α_λ < -2 and do not exhibit an infrared excess; most of the emission comes from the stellar photosphere of the young stars with only a small contribution from a remnant disc. Class III sources are also identified as weak line T Tauri stars (WTTs) because of smaller equivalent widths of accretion-tracing lines. Any foreground dust will scatter shorter wavelength emission more than the emission at longer wavelengths and so Class III sources often appear reddened.

Identifying young sources with IR excesses in the field allows regions where star formation is currently taking place to be traced. By analysing the distribution of sources of each evolutionary stage conclusions can be drawn as to how the stars may have formed. In particular, one of the main objectives of this thesis is to assess to what extent star formation is induced by the compression of material in the cloud, commonly referred to as triggered star formation.

1.2.3 Triggered Star Formation

Observations indicate that the initial process governing the onset of star formation in the spiral arms is a gravitational instability in the arms and disks. However, triggering processes are believed to be responsible for sustaining and accelerating star formation following this initial spontaneous process (Elmegreen, 1998). There are three types of triggering commonly considered: compression of globules within a cloud, cloud collisions and accumulation of the cloud into a dense ridge which subsequently collapses into dense cores. This thesis deals with the latter scenario. The winds, expanding HII regions and eventual supernova explosions associated with massive stars can sweep up and compress the surrouding material in molecular clouds. Since the Jeans mass is related to the density of the cloud as $\propto \rho^{-1/2}$ (see Equation 1.5), compression of the gas decreases the value of the Jeans mass which means gravitational collapse can occur more easily and encourage star formation to take place. The details of the triggering processes associated with the expansion of an HII (ionised hydrogen) region are described in Chapter 4 and the expansion of a swept-up shell is examined in Chapter 5.

1.2.4 Disc Survival in Star Forming Regions & Implications for the Formation of Planetary Systems

Haisch et al. (2001b) estimated that in young clusters the fraction of protostars in a young cluster with a disk fell from an initially high value of 80% to 50% after 3 Myr, with an overall disc lifetime of about 6 Myr using K-L excesses. Mamajek et al. (2004) find similar timescales over which the discs disappeared with <7% of stars exhibiting N-band excesses for ages of 30 Myr. Haisch et al. (2001a) found that the disc lifetimes in IC 348 are even shorter for stars earlier than G-type with timescales of 2-3 Myr.

Johnstone et al. (1998) presented a model in which circumstellar discs were photo-evaporated by external UV radiation. Applying this model to the protostellar discs found in the Orion nebula showed that circumstellar discs are rapidly destroyed by the external UV radiation field. Balog et al. (2007) found using IRAC and MIPS 24μm data that 44.5% of stars in NGC 2244 have discs in reasonable agreement with the findings of Habing et al. (2001) and Mamajek et al. (2004). They conclude that only stars within 0.5 pc from the 'O' stars show a deficit of discs.

The disc lifetime sets constraints on the core accretion model of planet formation in which nebular gas is accreted on to a rocky core. Lin et al. (1996) proposed that for the case of 51 Pegasi, the planet may have formed further out in the disc and then migrated inward through interactions with the circumstellar disc. Haisch et al. (2001b) argue that it may be difficult for a planet to form in accordance with the core accretion model and to migrate close to its host within the 3 Myr timescale of disc survival. This constraint on the timescale would support the proposal by Boss (2000) that Jupiter-mass clumps may form on much shorter timescales (a few hundred years) from gravitational instabilities within a disc of 0.091 $M_\odot$ within 20 AU.

Stars more than 10 Myr old do not have optically thick discs but instead have optically thin debris discs with radii ranging from 100-1000 AU and masses ranging from 0.01-10 Earth Masses (Habing et al., 2001; Spangler et al., 2001; Greaves & Wyatt, 2003). The transition to an optically thin debris disc is expected to happen rapidly $< 10^5$ years (Skrutskie et al., 1990; Wolk & Walter, 1996) based on the observations of discs that display colours intermediate between those expected of optically thick and thin discs (Kenyon & Hartmann, 1995; Hartigan et al., 1990; Bontemps et al., 2001; Haisch et al., 2001c; Jayawardhana et al., 2001; Stassun et al., 2001; Najita et al., 2003). Planet formation can explain the "loss" of material during the evolution from an optically thick to an optically thin disc. Growth of planetesimals first occurs in the disc, followed by collision and mergers into planets. Once bodies about 1000 km in diameter are formed, they accelerate any remaining planetesimals to high velocities creating a collisional cascade which creates the dust observable at mid IR wavelengths over timescales of approx. 1 Myr (Kenyon & Bromley, 2004). Mamajek et al. (2004) argued that the 10% of stars observed with N-band excesses may be the detection of dust formed in this way and is an observational signature of planet formation.

Habing et al. (2001) found that for stars younger than 400 Myr, the incidence of debris discs is about 50% but few debris discs are detectable at 60 microns for stars older than 400 Myr. This implies that discs do not survive for longer than 400 Myr similar to the timescale in which the heavy bombardment phase in our Solar System ended. However, Habing et al. (2001) point out that some young stars don't have discs and some old stars still do. If the optically thick disc around a star fails to survive before planet formation can take place then the collisional cascade of planetesimals cannot occur and consequently this would prevent the formation of a debris disc. This may explain why some young stars do not have debris discs.

1.3 Outline of Thesis

This thesis is broadly concerned with the detection and study of circumstellar discs as a means of investigating the formation of stars and planetary systems. In the case of debris discs, star and planet formation are already complete and the dust observed is continuously generated by collisions of comets. In the case of protoplanetary discs, the central source is a pre-main sequence star undergoing the final stages of formation. Mapping the position of these Young Stellar Sources (YSOs) can reveal clues as to if and how the local environment has had an impact on how these sources have formed.

Chapter 2 describes the methods and tools used to perform data reduction and measure the fluxes of sources in the field (point source extraction). Different methods of point source extraction are compared and contrasted to demonstrate their reliability.

Chapter 3 follows on from Greaves et al. (2005), who inferred the presence of a Neptune like planet around ϵ Eridani from motions of clumps in the debris disc. In this chapter, fake datasets are constructed using background galaxy and noise statistics. Chi-squared fitting is then employed to determine how reliably rotations of the disc can be recovered in the fake data and compared to results from the real, observed dataset.

The rest of the thesis consists of two surveys of Young Stellar Objects using IR data from the Spitzer Space Telescope. Chapter 4 follows on from the work of Phelps & Lada (1997) who discovered several clusters of stars in the Rosette Molecular Cloud whose formation appeared to be induced by the compression of material by the HII region associated with NGC 2244. A survey of YSOs in the region is conducted by fitting the data to pre-computed SED models using data with wavelength coverage from the 2MASS J band (1.25 microns) to MIPS 24 micron (Robitaille et al., 2006). The level of clustering apparent in the discovered YSOs is analysed and evidence for triggered star formation is discussed.

Chapter 5 presents a survey of YSOs around the W4 superbubble using spectral indices computed from 2MASS K_S band (2.17 microns) and MIPS 24 micron data and evidence for induced star formation is again discussed. The temperature of the dust in the region around AFGL 333 is estimated using IRIS and SCUBA 850 micron data to determine a mass for the superbubble and a corresponding star formation rate.

CHAPTER 2

Methods

This chapter describes the steps undertaken to reduce the data to produce high quality images and while performing point source extraction during which a flux is estimated for each point source. Data reduction and artifact removal was performed on Spitzer data using contributed software from the Spitzer website[1] and IRAF (Image Reduction and Analysis Facility). The SSC (Spitzer Science Centre) software MOPEX (MOsaicking and Point source EXtractor) was used to produce a mosaic of the individual frames and and also included APEX (Spitzer's Astronomical Point source EXtractor) which was used to perform point source extraction. SCUBA data was reduced using tools from the Starlink packages SURF (SCUBA User Reduction Facility) and KAPPA (Kernel APplication PAckage).

2.1 Observing at Infrared and Sub-millimetre Wavelengths

The dust in star forming regions scatters and absorbs most of light emitted at optical and UV wavelengths but the extinction cross section at infrared and sub-millimetre wavelengths is a factor of 10^2 smaller. Thus, observing at these longer wavelengths allows us to see through the dust and observe regions obscured at optical wavelengths. Throughout this thesis, the light detected originates from dust in interstellar clouds and circumstellar discs; this is the thermal or "blackbody" emission from cool particles. In chapter 3, the ϵ Eridani debris disc is observed at sub-millimetre wavelengths and in chapters 4 and 5, star forming regions containing molecular clouds and protostellar discs are observed in the far to mid infrared. Although protostellar discs consist of material from the molecular

[1]http://ssc.spitzer.caltech.edu/archanaly/contributed/browse.html

cloud from which the star formed whereas debris discs are composed of recycled material from comet collisions much later in the evolution of the host star, the physics governing the emission of radiation and their detection is essentially the same. In both cases UV and optical light from the star is absorbed by and heats dust grains in the disc. The grains then emit at longer wavelengths, typically at infrared wavelengths and longer for proto-planetary discs and in the sub-millimetre for colder debris discs. Since the light emitted from stars is at optical or shorter wavelengths due to their higher temperatures compared to the surrounding dust, the IR and sub-mm emission from the dust is distinct from photospheric emission. The result is that for stars with circumstellar discs, their spectral energy distributions (SEDs) no longer resemble that of a blackbody as is observed for photospheric emission from main sequence stars. Their SEDs will instead be a superposition of the photospheric emission of the star and a number of greybody curves for the dust at much lower temperatures resulting in an excess of emission at IR and sub-mm wavelengths. Sub-mm observations can be done at high, dry sites due to atmospheric windows such as at 850 μm, but for the mid to far IR ($\sim$30-300 μm) the atmosphere is opaque so observations must be done from space.

2.2 Spitzer Data Reduction

The images were obtained by the Spitzer 85 cm telescope, launched in 2003 into an Earth-trailing orbit and observing at wavelengths from 3.6 μm to 160 μm. The data are from the two continuum cameras.

2.2.1 IRAC

IRAC observes simultaneously in four channels at wavelengths of 3.6, 4.5, 5.8, and 8 μm, referred to as IRAC bands 1, 2, 3 and 4 respectively. IRAC bands 1 and 2 use InSb and bands 3 and 4 Si:As detector arrays, both consisting of 256 by 256 pixels (Fazio et al., 2004a,b). The field of view covered by each detector array is $5.2'$ by $5.2'$ with the band 1 and 3 field of view centre offset by $6.8'$ from that observed using bands 2 and 4. The pixel scale in all channels is approximately $1.2''$ by $1.2''$.

The Spitzer pipeline produces flux calibrated images known as Basic Calibrated Data (BCD) frames. These BCD frames undergo the following procedures as part of the automated pipeline:-

- First Frame Effect: Very small thermal changes in the internal IRAC cold electronics occur in the time between taking one frame and the next and this leads to offsets in the background level between the two frames. This is particularly noticable in the first frame taken in a series of observations. The first frame of every observing run with frame times greater than 2 seconds are therefore taken in high dynamic range mode to reduce the time between the first frames of each observation.
- Muxbleed: The InSb arrays (IRAC bands 1 and 2) suffer from this effect when the field of view passes over a bright source. The readout multiplexers in the cold electronics do not return to their quiescent state for a considerable length of time and this is believed to result from running the arrays at very cold temperatures. This results in a repeating pattern across the length of the array where the affected pixels contain extra flux than is actually present, appearing as a string of point sources extending either side of the bright point source. The effect is predictable and is partly removed as part of the automated pipeline.
- Detector Linearisation: As the detectors approach saturation their response becomes non-linear and any fluxes measured while the detector is in this regime will be low by several percent. This is corrected to within 1% in the pipeline but above a certain DN number value the correction can no longer meet the required accuracy of 1% and in this case the pixel is flagged so that it is not used later in the reduction process.
- Flatfielding: Each pixel in the detector array has its own responsivity (i.e. gain) and these variations are found by making observations of regions of sky as empty of emission from stars and dust as possible but with high zodiacal backgrounds. By co-adding and then normalising the values in each pixel in each of the observations, a map of the pixel to pixel variations is produced, called a flat field. This is divided into each frame to correct for the variations.
- Cosmic Ray Detection: Radiation hits are removed by comparing the pixel values of each frame with the median value of the stack and masking out pixel values

above a threshold. The threshold applied is set higher than is possible for real point sources (i.e. higher than the brightest stars in the field) to avoid discarding real sources; more aggressive outlier detection is performed later, when mosaicking the BCD frames together and removes the remaining radiation hits.

- Flux Calibration: Aperture photometry on stars is used to measure both long and short term variations in the absolute IRAC calibration. The aperture used has a $12''$ radius, therefore as a smaller aperture is typically used during point source extraction, a correction factor has to be applied (see Section 2.6.2). The flux in each IRAC band for each calibration star is derived from models of each spectral type and estimated to be accurate within 3% (Cohen et al., 2003). The flux calibration is applied by multiplying the image by a conversion factor and final BCD frames are output with units of MJy/sr.

Artifact Removal

The Artifact Mitigator and the Stray Light masker (contributed software on the Spitzer Website) were used on the basic calibrated data (bcd) frames of the IRAC data to remove artifacts produced both electronically and optically. Both write to a mask file which labels the affected pixels in each frame and this is used when mosaicking to reject pixels labelled as containing a bad data value.

Artifact Mitigator & Jailbar Corrector

- Muxbleed: The pipeline processing only partly removes this effect, the remaining affected pixels are corrected at this stage.

- Column Pull Up/Pull Down: This effect is caused by only brightest sources and results in a change in intensity in the column, above and below the source. The artifact mitigator estimates the true sky value of the affected pixels and applies an offset to correct for the effect.

- Row Pull-Up: Electronic banding may occur in all IRAC channels and is observed as a positive offset either side of a bright source but it is not as significant as muxbleed in channels 1 and 2 or optical banding in channels 3 and 4. The artifact mitigator applies an offset to the affected pixels.

- Latents: This is the contamination of a frame by a bright source observed in a previous frame. Short term latents lasting a few minutes are seen in all IRAC bands, but longer latents are also seen in IRAC bands 1 and 4. The effect is significantly reduced by temporarily heating channels 1 and 4 with a small current through the detector. Remaining latents are masked out for frames in which the previous frame contained a source bright enough to leave a latent more than three times the predicted noise.
- Jailbars: Each IRAC detector has four readout channels, each reading a vertical alternating column in the array leading to every 4th column in the array having a slightly different background level. The Jailbar Corrector computes the median levels of each readout channel and then adds in a correction to make each one equal to the mean median level of all readout channels.

Stray Light Masker

Stray light originates from light reflected off the array covers and from internal scattering in the filters, beam splitters and the primary mirror shadowed by the secondary and supports. The stray light masker predicts the location of stray light incident on the detector arrays from sources using information from the Two Micron All Sky Survey (2MASS) and writes to the mask files to flag the affected pixels.

Artifacts Not Corrected By Software

- The first frame effect: The first frame must be discarded and not included when mosaicking and performing Point Source Extraction as it is taken in High Dynamic Range mode (which means the integration time is much shorter than for the rest of the frames) as described in the pipeline processing.
- Full-Array Pull-Up: This effect occurs when the background level for entire BCD frame is higher than for the rest of the mosaic and is corrected later using MOPEX (see section 2.3).

- Colour Correction: When converting from data numbers detected to flux densities, the convention is to convert the signal to an equivalent monochromatic flux density at the weighted average wavelength of the band being used assuming a flat spectrum across the bandwidth. In reality the sources being observed will be a mixture of bluer sources like main sequence stars and redder sources such as asteroids and Young Stellar Objects with non-flat spectral shapes and the conversion is dependent on the slope of the spectrum across the band. For this reason a correction can be applied to adjust the fluxes measured dependent on their temperature. Errors associated with colour corrections are estimated to be about 3% for IRAC and were not included as they were small compared to other effects and to apply the correction for thousands of objects of different colours would have proved to be very time consuming.

- Array Location Dependent Colour Correction: Due to corrections made during flat-fielding to correct for the zodiacal dust, bluer IRAC sources may require an array location photometric error that in cases of low coverage may be as large as 10%. A correction was applied by multiplying each individual bcd frame with a photometric correction image. The solid angle subtended by each pixel is slightly different across the array due to IRAC being located slightly off the Spitzer telescope axis. This correction is normally made by MOPEX while the frames are being mosaicked to avoid distortion of the frames. Since this correction was already made to the photometric correction images the correction images had to be divided by the pixel solid angle correction images so that the correction was not applied twice.

- Pixel phase: The pixels are more sensitive near their centres than their edges and this effect can be avoided by applying a pixel phase correction. It is a $<1\%$ effect for IRAC bands 2-4 and a 4% effect for IRAC band 1. However, the pixel phase averages out for well sampled data and since the data had high coverage and the correction was small compared to the errors associated with the point source extraction it was not necessary to include a pixel phase correction.

- Aperture corrections: These are applied at a later stage following point source extraction to correct for the fact that the apertures used to minimise the contamination from nearby sources in crowded fields are typically smaller than the $12''$ radius aperture used when measuring the fluxes of calibration stars.

2.2.2 MIPS

The pipeline processing for MIPS includes similar steps as described above for IRAC, however, an infinite aperture is used during the flux calibration and the only artifacts present in the MIPS data are latents and full-array pull-up of which the latter is corrected using MOPEX. Therefore the data reduction steps performed on the MIPS data were:-

- Latent Removal: Removal of latents in the MIPS data was achieved using the Image Reduction & Analysis Facility (IRAF) by division of the individual frames with the median image calculated with values from the same array positions in all the frames.
- Asteroids: These can be misidentified as "red" objects. Data taken near the ecliptic plane are likely to include asteroids, which can be confused with reddened YSOs and are visible in the MIPS 24 μm image. Asteroids can be distinguished from other point sources such as Young Stellar Objects by blinking between frames taken in two different epochs to reveal their rapid motions across the sky. This showed that there was no contribution due to asteroids when surveying the RMC in Chapter 4 and the contribution is expected to be negligible for the survey of the W4 loop in Chapter 5 due to its position far from the ecliptic plane.
- Filtering of 70 micron Data: Filtered or non-filtered frames were available to create the MIPS 70 μm mosaic. The filtered frames were made by subtracting off the median of the surrounding frames, which reduces the effect of latents on the final mosaic. However, in the filtered frames information from regions of extended emission is lost and point source photometry in regions with high levels of extended emission is affected. Non-filtered images were used to create the MIPS 70 μm mosaic since the regions studied did contain high levels of extended emission. This meant that some small artifacts were not removed from the data but ensured that the photometry in regions of extended emission was preserved and thus could be used to perform point source photometry at 70 microns.

2.3 Background Matching (Overlap Correction)

Mosaics often include regions where the background level is noticeably different from the rest of the image. This is caused by bias fluctuations in the array due to the first frame-effect and bright source effects. An example of this effect is shown in Figure 2.1. This can be fixed by matching the background levels of overlapping frames in a mosaic. MOPEX performs background matching by first interpolating the individual frames that are to be used to make the mosaic to a common grid and then applying a constant offset, ϵ^n, to each input frame, I^n, to create a corrected output frame O^n:-

$$O^n(x, y) = I^n(x, y) - \epsilon^n \tag{2.1}$$

The offset for each input frame is determined by minimising the combined uncertainty weighted difference between the overlapping areas, A, of each pair of input frames:-

$$L = \sum_{m,n=1(m \neq n)}^{N} \sum_{k \in A} \frac{I^n(k^n) - I^m(k^m)}{\sigma_n^2(k^n) + \sigma_m^2(k^m)} \tag{2.2}$$

where m and n are labels for each input image and k^n denotes the pixel number in image n. An additional constraint requiring the total of all the corrections applied to each of the frames, excluding outliers, to be equal to 0 ensures that there is no global offset applied.

2.4 Mosaicking

MOPEX interpolates the background matched frames on to a common grid. Bilinear interpolation (linear interpolation performed along one axis, and then along another axis) is used to map the pixels on to the grid to account for the pixel overlap areas between the input frames and the common grid. The frames are co-added to make one image by averaging the interpolated pixel values from each frame.

MOPEX also detects moving objects and radiation hits in the image while mosaicking the individual frames together, a process known as outlier detection. This is done using both single frame spatial filtering, multiframe temporal filtering and multiframe dual temporal-spatial filtering.

Single frame spatial filtering is used to eliminate radiation hits. Two thresholds are applied to a background subtracted image (see section 2.5.1 for how these are produced) as shown in Figure 2.2. Bright point sources will have a greater number of pixels with

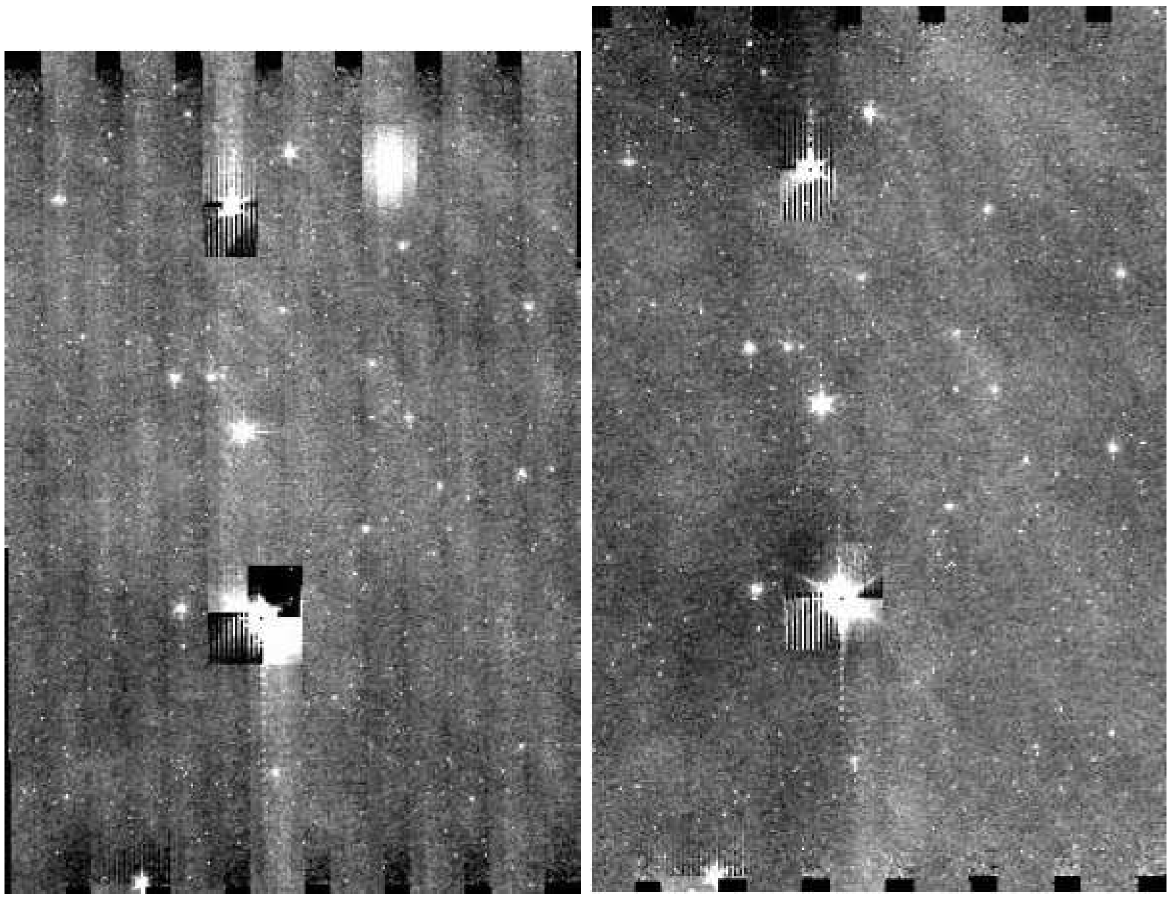

Figure 2.1: Left panel: A mosaic exhibiting systematic variations in the background in frames near bright sources. Right panel: The same mosaic after background matching applied by adding a constant offset to each of the constituent frames.

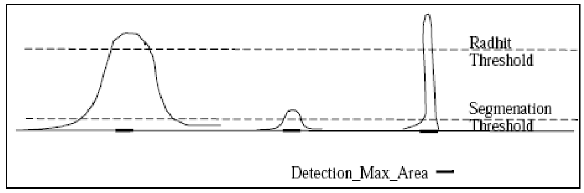

Figure 2.2: A diagram demonstrating how a radiation hit (right) is distinguished from a bright point source (left) and a faint point source (centre). This figure and subsequent sketches from Spitzer documentation.

values above the Segmentation Threshold than that set using the “DetectionMaxArea” parameter. Faint point sources will not include any pixels with values above the Radhit Threshold. Radiation hits will include at least one pixel value above the radhit threshold but a number of pixels with values above the Segmentation Threshold below that set using the “DetectionMaxArea” parameter in MOPEX, to account for the fact that a radhit is smaller than the PSF of a real bright source. In this way, radiation hits can be distinguished from point sources and masked out when producing the final mosaic. The disadvantage of this form of filtering is that medium strength radiation hits or radiation hits occupying a large number of pixels will go undetected.

For multiframe temporal filtering, the frames are interpolated on to a common grid so that each pixel has a number of values from each contributing frame. The mean and standard deviation of the values from all the contributing frames is computed so that for each contributing pixel, a deviation from the mean can be determined. Thresholds for the minimum and maximum value accepted for each contributing pixel are set to find objects that appear in some frames but not others. The disadvantage of this form of filtering is that for parts of the mosaic where the coverage is low, that the standard deviation of contributing pixels can not easily be determined.

Dual outlier detection is a two stage process. In the first stage spatial filtering is used to produce detection maps of clusters of adjacent pixels above a given threshold. Clusters containing a number of pixels less than the minimum allowed size set as a parameter in MOPEX are flagged. Temporal filtering is then applied to the detection maps to eliminate clusters of pixels that do not appear in the majority of the maps at each spatial location. Figure 2.3 illustrates a simple example of dual outlier detection. Dual outlier detection complements multiframe temporal filtering as it works more reliably in parts of the mosaic with low coverage.

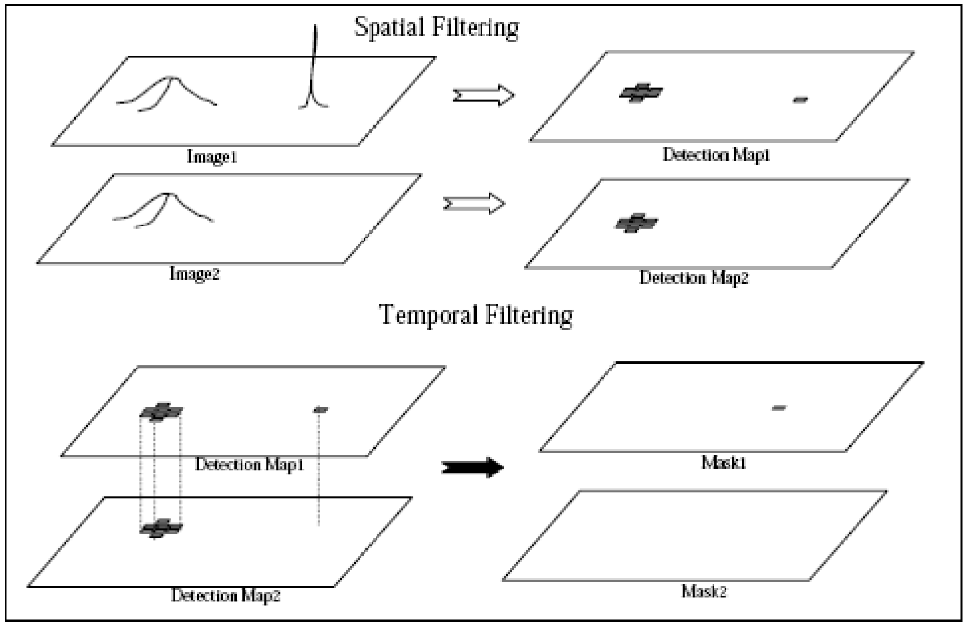

Figure 2.3: Diagram outlining the process of dual outlier detection. Spatial filtering is first applied to produce a detection map and then temporal filtering is used to identify clusters of pixels in the detection map that do not appear in the majority of maps as outliers.

2.5 Point Source Extraction

2.5.1 Background Estimation

A background subtracted image is produced by finding a skewed median for each pixel in the input image by rejecting a number of the highest pixels in a square window of the image which are likely to belong to point sources and should not be included in the background estimation. Two background subtracted images are used during point source extraction, the first is used for point source detection and the background subtraction is aggressive (a small window is used) and the second is used later for point source fitting for which a larger window is used to preserve the photometry.

The background fluctuations are also estimated in a similar way by determining the 68-percentile range of the pixel values in the sliding square window to estimate the Gaussian noise. A signal to noise ratio image is produced by computing the ratio of the input image to the Gaussian noise for each pixel and this was later used during the image segmentation process.

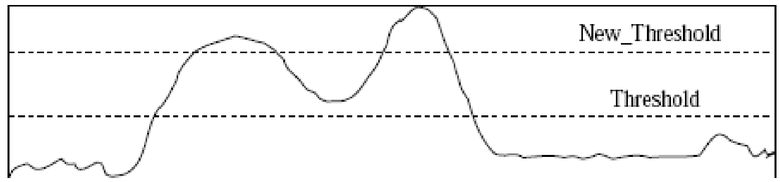

Figure 2.4: Diagram demonstrating how increasing the detection threshold can split a large cluster of pixels into smaller sub-clusters of pixels.

2.5.2 Point Source Detection

Image segmentation is the process by which clusters of adjacent pixels are identified as separate point sources. APEX first finds groups of adjacent pixels above the initial threshold. Input parameters are used to determine the minimum and maximum number of pixels allowed in each cluster of pixels. The minimum and maximum number of pixels was set to 2 and 9 for IRAC and between 4 and 200 for MIPS 24 micron to account for different beam sizes at each wavelength. Clusters with less than the minimum number of allowed pixels are not counted in the point source list. Clusters of pixels larger than the specified upper limit are either reduced in size or split into two separate clusters by iterative increasing of the threshold as shown in Figure 2.4. By default APEX performs non-linear matched filtering to produce a point source probability (PSP) map designed to improve the detectability of point source detection. In practice, this resulted in a high number of false detections particularly in IRAC bands 3 and 4 and MIPS 24 micron band which included complex extended background emission. Running the point source detection module on the SNR image based on the background subtracted image was found to yield the most reliable results.

Point sources that were detected from the same cluster of adjacent pixels after the application of the initial threshold are flagged by APEX as a blend of sources. Figure 2.5 shows a simple example of deblending for a given set of input parameters. Sources identified as part of a blend are later subjected to passive deblending, in which sources whose PSFs overlap are fit simultaneously by APEX.

The position of each point source detected by calculating the centroid for each group of pixels:-

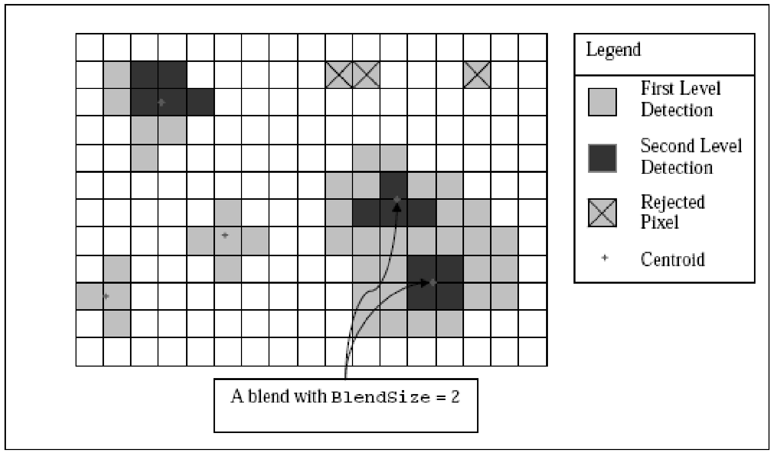

Figure 2.5: An example of image segmentation where the parameters are set so that the minimum number of adjacent pixels required for a valid detection is set to 3 but the maximum allowed number of adjacent pixels is set to 9. Raising the threshold shrinks the upper left cluster of pixels whilst the lower right cluster is split into two separate subclusters.

$$\overline{x} = \frac{\Sigma I_i x_i}{\Sigma I_i} \tag{2.3}$$

$$\overline{y} = \frac{\Sigma I_i y_i}{\Sigma I_i}, \tag{2.4}$$

where I_i is the flux in each pixel and x_i, y_i are the pixel co-ordinates.

2.6 Point Source Photometry

Once a list of point sources detected in the image has been produced, there are two possible methods of determining the flux of each point source. The first is profile fitting of the Point Spread Function (PSF) of the telescope to each source and the second is aperture photometry by integrating the flux within a given radius.

2.6.1 PRF Fitting

The final positions and photometry of the sources are estimated by fitting the data with the Point Response Function (PRF). The Point Response Function is the convolution of the PSF with the pixel response function and standard PRFs are supplied with MOPEX and are available on the Spitzer website. It is also possible to determine a PRF from the data using the MOPEX perl script "prf_estimate" but due to a combination of saturation of bright sources and complex extended emission, generating a PRF in this way proved unreliable and yielded poor results.

The fitting can be done either on the background subtracted image or on the input image and with a constant background in the fitting area estimated as part of the fitting process. The best fit is found by minimising the following χ^2 value (Makovoz & Marleau, 2005):-

$$\chi^2 = \sum_{j=1}^{N} \sum_{i \in W_j} \frac{(s_j(i) - \sum_{n=1}^{M} f(n) PRF(i, R_j(n)) - b)^2}{\sigma_j^2(i)} \tag{2.5}$$

where s_j and σ_j are the pixel values in the fitting area W in the j-th input and uncertainty images respectively, $R_j(n)$ are the local coordinates in the j-th input image of sources with flux f(n), b is the background in the fitting area and PRF(i,R_j(n)) is the contribution of the n-th point source to the i-th pixel. If the χ^2/dof is greater than the threshold then the fitting of the point source has failed and APEX will attempt active deblending in which it attempts to fit the profile with more than one source. In practice, this consistently resulted in many false detections and was not used, and passive deblending in which the sources were separated prior to profile fitting produced more reliable results.

APEX also produces a residual image in which the estimated points sources are subtracted from the input image. This residual image can be used to assess the effectiveness of the profile fitting and examples are shown in Figures 2.6 and 2.7.

2.6.2 Aperture Photometry

The fitted flux is incorrect for sources where the corresponding location in the residual image shows either a hole or part of source left behind and in these cases it is preferable to use an aperture to measure the flux from a source. Aperture photometry essentially involves summing the flux within a radius centred on the point source to determine the total flux. MOPEX computes the aperture photometry flux, AP, by summing the products of the pixel values I_i and the fraction of the pixel included within the aperture a_i:-

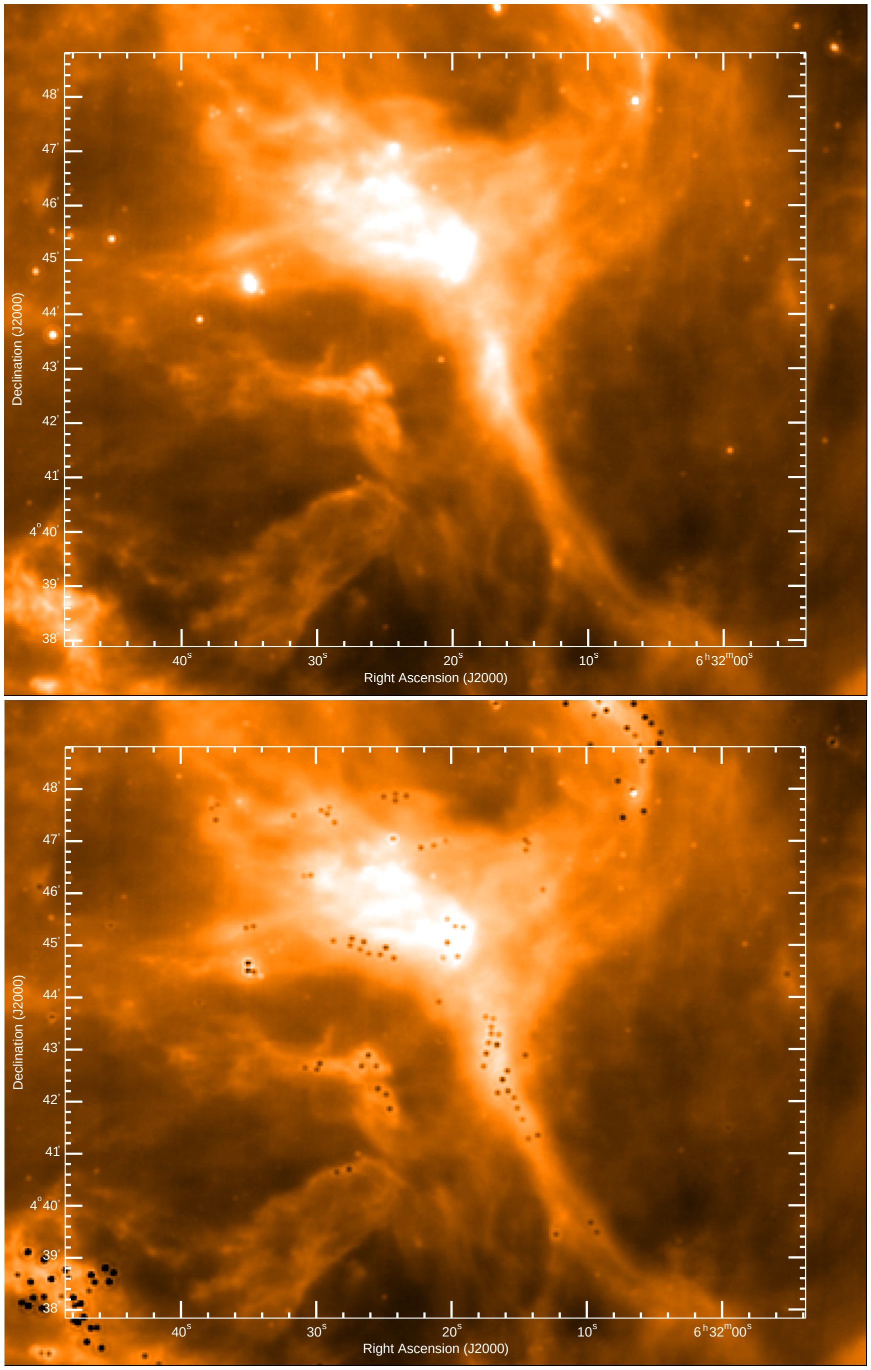

Figure 2.6: Upper Panel: A region of the MIPS 24 μm image of the Rosette Molecular Cloud. The intensity scale is linear from 40 to 60 MJy/sr. Lower Panel: The residual image of the same region with point source fluxes subtracted. The "holes" indicate where the point source flux has been overestimated and the majority are caused by false point source detections when using the PSP image to detect sources.

.

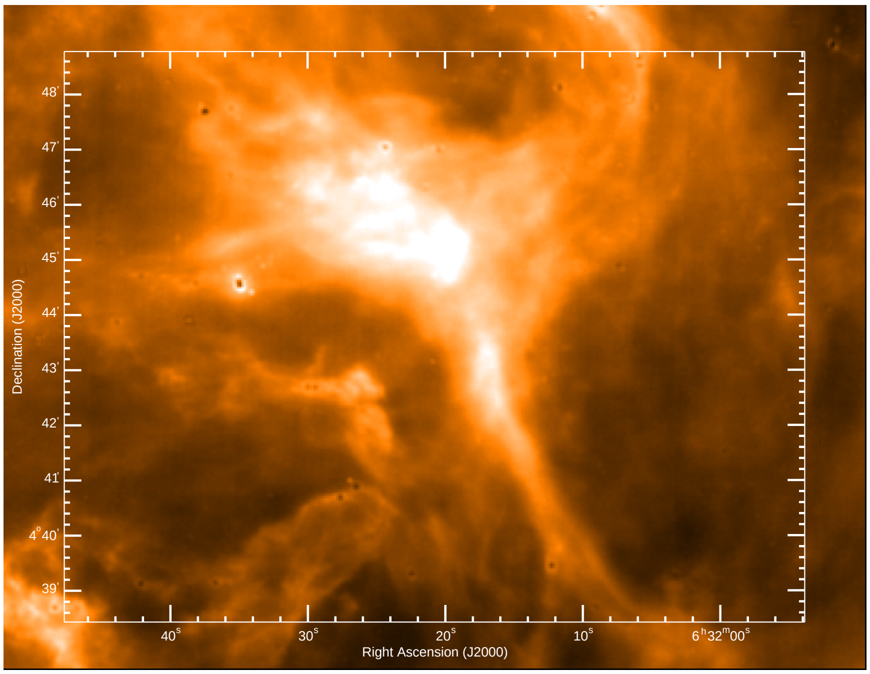

Figure 2.7: Another residual image of the same region shown in Figure 2.6 using the same intensity scale but with improved point source detection using a SNR image based on the filtered image.

.

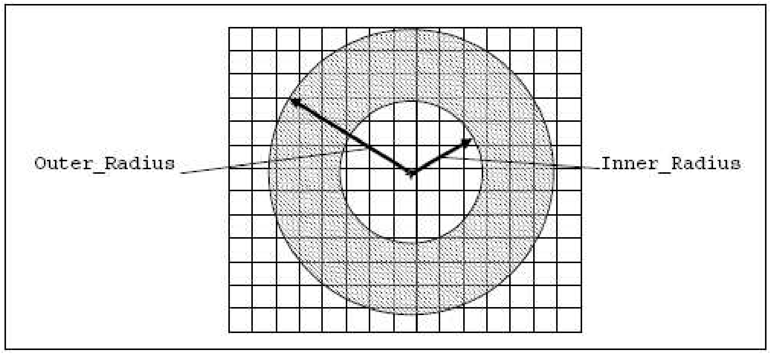

Figure 2.8: Schematic showing an example of an annulus used in background estimation for aperture photometry.

$$AP = \Sigma a_i I_i \tag{2.6}$$

The aperture radius is chosen to include most of the source without including any contaminating objects or bright background nearby. Avoiding background contamination is particularly important in IRAC bands 3 and 4 where PAH (Polycyclic Aromatic Hydrocarbon) emission is highly structured. It therefore follows that aperture photometry is not well suited to crowded regions of sky including a lot of deblended sources as this will result in overestimation of the flux within the aperture.

The background close to the source must also be estimated and subtracted out and this is achieved by either using the background subtracted image (see § 2.5.1) and using equation 2.6 or estimating the local background using a median pixel value computed for pixels within an annulus centred on the point source.

In the latter case, the flux of the median pixel value in the annulus, B, is subtracted from the flux contained within the aperture itself using:-

$$AP = \Sigma a_i I_i - B\Sigma a_i \tag{2.7}$$

To estimate the background close to the source, it is preferable for the inner radius of the annulus to be chosen to be just larger than the radius of the aperture itself. An annulus of 12 arcseconds (10 pixels in IRAC images) is actually used when calibrating the IRAC data by measuring the flux from a set of stars. The apertures typically used in most fields are much smaller than this to avoid flux from contaminating sources as discussed above.

These apertures will include less of the flux of the source than the calibration aperture so a correction ranging between 12% and 23% must be applied to the fluxes computed[2] (Reach et al., 2005). A similar aperture correction must also be applied to point sources found in the MIPS data, where an infinite aperture is used during calibrations.

Comparison of the fluxes determined using these two methods of point source photometry allows their reliability to be assessed. Figures 2.9 and 2.10 show a comparison of aperture fluxes using an aperture of 5 pixels and fitted fluxes computed for a sample of point sources in IRAC band 1. For point sources detected using deblending the aperture flux is higher than the fitted flux, as expected due to contamination by adjacent sources. For points sources detected without deblending the relationship between the aperture fluxes and fitted fluxes roughly lie along a straight line with a slope of 1 indicating that the two methods of point sources photometry are roughly consistent. At higher fluxes the points deviate from the straight line with a slope of 1 and the relationship becomes non-linear. Possible explanations for this are that these sources are so bright that the detector response is non-linear when detecting these fluxes or that the fitting area used for bright sources is too small.

There is also a population of faint sources for which the aperture fluxes are higher than the fitted fluxes. Binning the sources by goodness of fit (χ^2/dof) for the fitted fluxes reveals a bi-modal distribution as shown in Figure 2.11 with peaks near χ^2/dof=1 and χ^2/dof=10. These two populations of sources occupy distinct regions of the aperture vs fitted flux plots, with the χ^2/dof $<$3 sources generally having higher aperture fluxes than fitted fluxes and χ^2/dof $>$3 sources lying along the straight line of slope 1. The high χ^2/dof value for the good non-deblended sources is probably due to underestimated uncertainties or the undersampled IRAC band 1 PRF. The source with χ^2/dof $\sim$1 are actually false detections in the background, confirmed by examination of the image and residual image with the two populations of point sources overlaid.

2.7 SCUBA Data Reduction

The data used from JCMT in Chapter 5 had previously been reduced, but a brief description of the data reduction process is included here for completeness as it is important to

[2]Table 5.7, IRAC Data Handbook

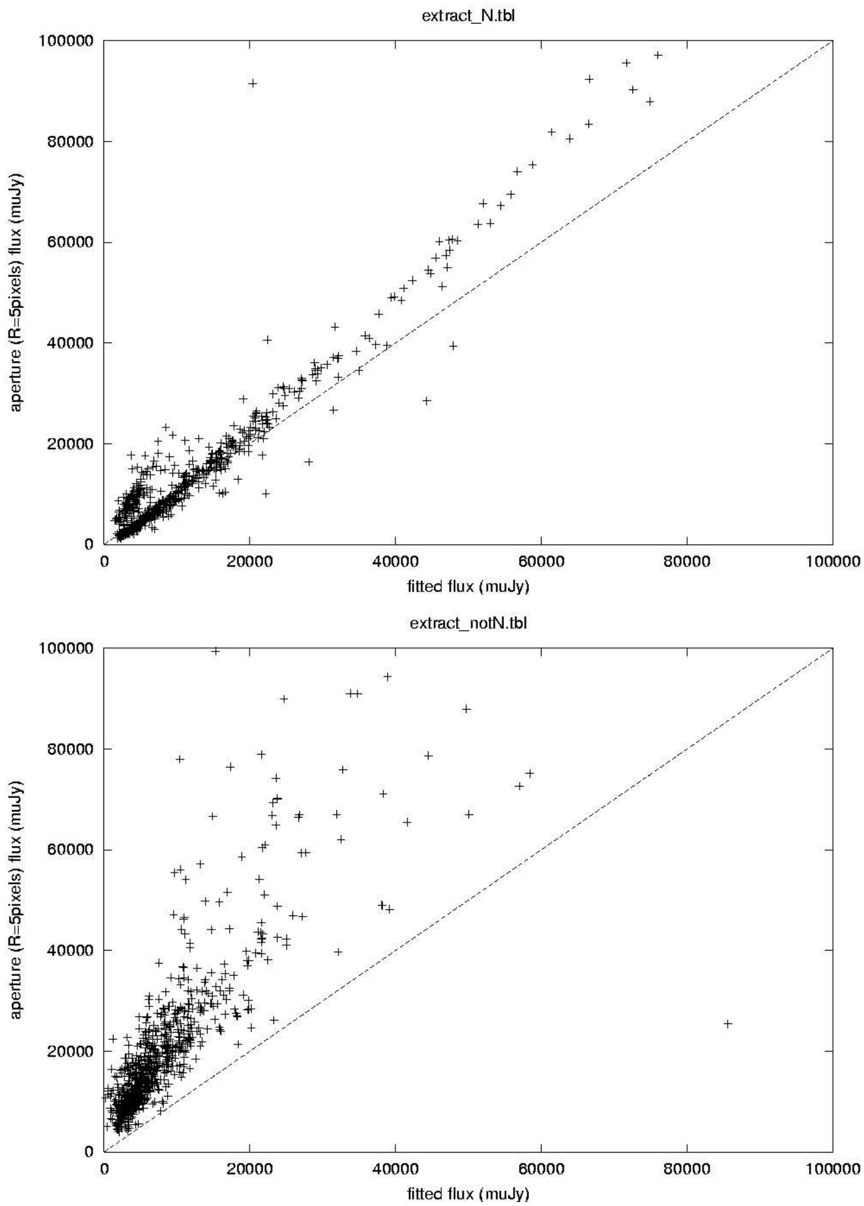

Figure 2.9: Aperture fluxes versus fitted fluxes for a sample of IRAC band 1 points sources: Top: Point sources detected without deblending, Bottom: Point sources detected using deblending.

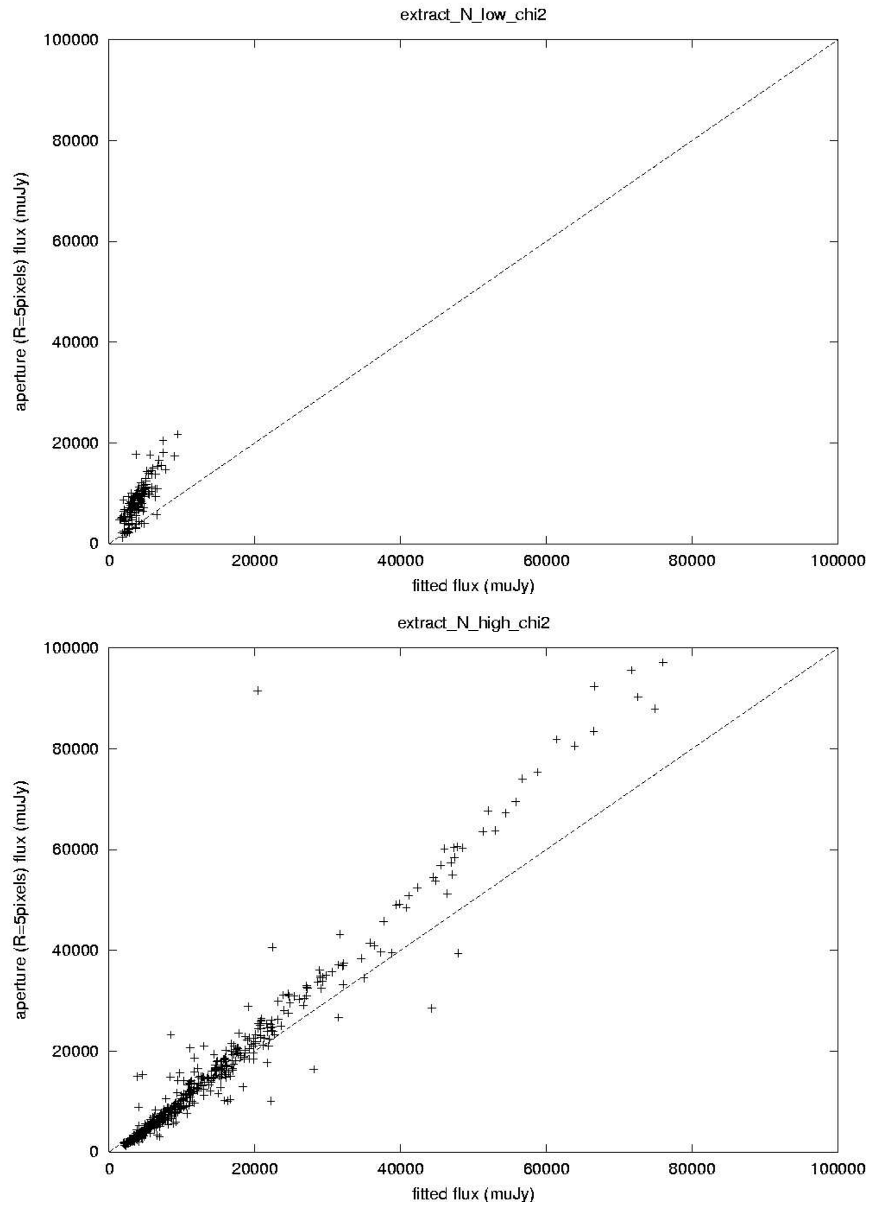

Figure 2.10: Aperture fluxes versus fitted fluxes for a sample of IRAC band 1 points sources: Top: Point sources with χ^2/dof <3 (good fits), Bottom: Point sources with χ^2/dof >3 (poor fits).

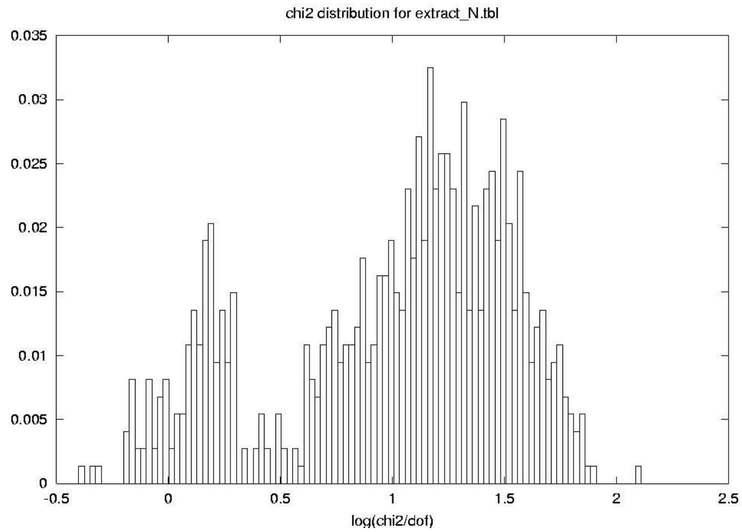

Figure 2.11: Distribution of chi2/dof fits for a sample of IRAC 1 point sources.

understand the process for later simulation of data. General procedures such as flatfielding and mosaicking are similar to Spitzer imaging but corrections must also be made to account for the atmospheric emission and absorption of astronomical signals.

2.7.1 Instrument Description

The sub-millimetre data was taken using the Submillimetre Common User Bolometer Array (SCUBA) on the James Clerk Maxwell Telescope on Mauna Kea, Hawaii. SCUBA consists of a Long Wave array of 37 bolometers operating at 850 μm and a Short Wave array of 91 bolometers operating at 450 μm which are used simultaneously using a dichroic beam splitter. Each pixel operates at diffraction limited resolution on the JCMT which corresponds to a FWHM of $14.5''$ and $8''$ at 850 and 450 μm respectively. The bolometers in the Long and Short arrays are arranged in a hexagonal pattern and both arrays have a field of view approximately 2.3 arcmin across.

2.7.2 Sky Removal - Chopping

During all observations with SCUBA, sky removal is achieved by moving the secondary mirror so that the centre of the array points to a region of sky 30 - 180 arcseconds off source; a process known as chopping. This is done at a rate of 7.8 Hz and observations of the source are interleaved with blank regions of the sky off-source so that the atmospheric signal can be subtracted. The telescope moves to put the source in the opposite chop beam to allow further atmospheric subtraction and an estimate of the DC offset between each bolometer in the array. The data used were taken in jiggle map mode in which the secondary mirror is used to follow a 64 point pattern with 3 arcsecond spacing. This mode was used because the hexagonal arrangement of the bolometers in each array, each spaced 2 beams apart, means that staring at one position would lead to undersampling of the sky. Chopping the secondary takes place at each position with nodding the primary taking place every 16 observations.

2.7.3 Data Reduction Steps

- Flatfielding: In similar fashion to the Spitzer Data reduction sequence the variations in response from each bolometer in the array are corrected by first using the KAPPA task "reduce_switch" to separate the raw data into its components and to subtract the off-beam data from the on beam data. The flat field is applied using the task "flatfield".

- Extinction Correction: The attenuation of the signal due to the atmosphere must be taken into account in order to produce a final image with correct fluxes. The atmospheric opacity is determined using Skydips from both the JCMT at SCUBA wavelengths and the Caltech Submillimetre Observatory (CSO) at 225 GHz. Skydips at the JCMT measure the sky brightness temperature over a range of elevations, by alternating between observing the sky, a hot load and a cold load at each elevation. Since the temperature of the hot and cold loads are known they are used to calibrate the observations of the sky itself. The atmospheric attenuation can then be determined for the specific airmass (elevation) being observed through.

- Despiking: Cosmic ray hits are detected by analysis of the time series data for each bolometer and removing the largest spikes using 5σ clipping.

- Sky Noise Removal: Nodding and chopping do not remove all of the sky-signal because the source signal is constant with time whereas the sky-signal is time dependent but coherent across the array. Sky noise is defined as changes in the sky level faster than 7.8 Hz. The remaining sky-noise signal is estimated using the median of all of the bolometers during an observation.

- Signal Determination: The signal to noise ratio for any given source is calculated by computing the standard deviation of pixels in a region of the field off source in the same sized aperture used to measure the flux of the source.
- Flux Conversion Factor: The final step is to convert from units of Volts in the image to units of mJy arcsecond^{-2} by multiplying the image by a flux conversion factor. Mars and Uranus are used as the primary calibrators using the expected flux derived from standard models for planetary fluxes.

2.7.4 Source Extraction

Source Extraction for the SCUBA data could not be done with standard techniques and the methods of clump identification are discussed in Chapter 3.

CHAPTER 3

Detecting a Rotation in the ϵ Eridani Debris Disc

This chapter is based on a paper published in Monthly Notices of the Royal Astronomical Society by:
Poulton, C.J., Greaves, J.S., Cameron, A.C. (2006, MNRAS, 372, 53)

3.1 Abstract

The evidence for a rotation of the ϵ Eridani debris disc is examined. Data at 850 μm wavelength were previously obtained using the Submillimetre Common User Bolometer Array (SCUBA) over periods in 1997-1998 and 2000-2002. By χ^2 fitting after shift and rotation operations, images from these two epochs were compared to recover proper motion and orbital motion of the disc. The same procedures were then performed on simulated images to estimate the accuracy of the results.

Minima in the χ^2 plots indicate a motion of the disc of approximately 0.6″ per year in the direction of the star's proper motion. This underestimates the true value of 1″ per year, implying that some of the structure in the disc region is not associated with ϵ Eridani, originating instead from background galaxies. From the χ^2 fitting for orbital motion, a counterclockwise rotation rate of $\sim$2.75° per year is deduced. Comparisons with simulated data in which the disc is not rotating show that noise and background galaxies result in approximately Gaussian fluctuations with a standard deviation $\pm$1.5° per year. Thus counterclockwise rotation of disc features is supported at approximately a 2-σ level, after a 4-year time difference. This rate is faster than the Keplerian rate of 0.65° per year for features at $\approx$65 AU from the star, suggesting their motion is tracking a planet inside

the dust ring.

Future observations with SCUBA-2 can rule out no rotation of the ϵ Eridani dust clumps with $\sim 4\sigma$ confidence. Assuming a rate of about 2.75° per year, the rotation of the features after a 10-year period could be shown to be $\geq 1°$ per year at the 3σ level.

3.2 Introduction

3.2.1 ϵ Eridani: A Special Case

Debris discs around nearby stars represent extra-solar analogues of the Kuiper Belt. It is in this context that studying the ϵ Eridani dust ring is of particular interest since it is of spectral type K2V, not too dissimilar to the Sun, but with a much younger age of 0.8 Gyr (Song et al., 2000; Di Folco et al., 2004) and thus represents an analogue to the young solar system. It is generally thought that protoplanetary discs evolve into debris discs after planets have formed, a process that is completed within 10-100 Myr after star birth (Schütz et al., 2004; Holland et al., 1998). Greaves et al. (2004a) remarked that there was an apparent lack of overlap between stars with debris discs detectable at submillimetre wavelengths and those with radial velocity planet detections. However, this was based on the fact that only a few stars were observed with positive detections for both an infrared dust-excess and a radial velocity planet (Dominik et al., 1998; Beichman et al., 2005). It was noted that this was likely to reflect the small number of stars for which both phenomena had been investigated. More recent surveys have shown the detection rate for debris discs is similar for stars with and without planet detections (Beichman et al., 2006). Nevertheless, ϵ Eridani remains unique in having a resolved structure within the debris ring (Greaves et al., 1998, 2005) plus an inner gas giant planet detected by Doppler wobble (Hatzes et al., 2000) and astrometry (Benedict et al., 2006). Further evidence for this planet comes from the forced offset of the centre of the ring (Greaves et al., 2005), consistent with a forced eccentricity of the dust particles (Wyatt et al., 1999). The ring structure also appears perturbed as if by a more distant gas giant, but this body has not yet been detected, which implies a maximum mass constraint at around the dust ring radius of approximately 5 M_J (Macintosh et al., 2003).

3.2.2 Planet Hunting by Tracking of Disc Features

An infrared excess around ϵ Eridani was first detected during photometric measurements by the Infrared Astronomical Satellite (IRAS) (Aumann, 1988), soon after the initial discovery of an IR excess around Vega (Aumann et al., 1984). Subsequent submillimetre observations of ϵ Eridani at 850 μm with the Submillimetre Common User Bolometer Array (SCUBA) by Greaves et al. (1998) resolved the disc and showed a ring-like structure. However, imaging at optical wavelengths has not yet succussfully detected the faint ring surrounding ϵ Eridani (Proffitt et al., 2004).

Further SCUBA observations made in the period 2000-2002 (Greaves et al., 2005) allow us to study the motions of the substructure in the ring over a 5 year period. If clump features are tracking the orbital motion of a planet within the ring, they should appear to rotate faster than the Keplerian rate at the ring radius; this would be an unambiguous signature of a planet with the forced period providing a measure of its orbital semi-major axis. Clumps will appear in a disc where planet formation has taken place because the planets will migrate outwards via angular momentum exchange with the remaining planetesimals. As the planets migrate outwards, the associated gravitational resonances also move out, thus trapping dust particles outside the planet's orbit into mean motion resonances (Wyatt et al., 1999, 2003). It is likely that the Kuiper Belt in the Solar System formed in a similar way; where the material is thought to have been pushed outwards by a mean motion resonance associated with Neptune as it migrated further away from the Sun (Gomes, 2003; Levison & Morbidelli, 2003; Malhotra, 1995).

Circumstellar dust, trapped into resonances by an outwardly migrating planet (Wyatt et al., 1999, 2003; Quillen & Thorndike, 2002), is expected to be observable at submillimetre wavelengths. The ϵ Eridani dust ring offers a unique prospect to directly track motion of clumps over time, because of its favourable inclination ($\sim$25° from face-on to the observer) and the fact that this is one of the closest stars to the Sun at a distance of 3.22 pc. Whilst the Vega and Fomalhaut disc asymmetries have been modelled (Wyatt et al., 2003; Wyatt & Dent, 2002), the disc structure is not as clearly resolved as in the ϵ Eridani dust ring and in the case of Fomalhaut the disc is inclined edge-on to the observer. Models of the distribution of the ϵ Eridani clumps (Quillen & Thorndike, 2002; Ozernoy et al., 2000) suggest the perturbing planet lies $\approx$40-60 AU from the star, thus the clumps are expected to orbit with a period of $\approx$280–520 years. These rotation rates of 0.7–1.3° per year, corresponding to particular resonant periods (Quillen & Thorndike, 2002; Ozernoy et al., 2000), require long times to detect. Here, a preliminary analysis of 5 years of data is presented, making use of image fitting to statistically recover any small rotation present.

3.3 Observations

The results used here consist of the 5 year dataset presented by Greaves et al. (2005). Observations of ϵ Eridani at 850 μm were made with SCUBA between August 1997 and December 2002, in total comprising 56 images and an integration time of 33.5 hours. The dataset is split into two parts, one including data taken during 1997-1998 and the other from 2000-2002; the observing runs were bunched in time so that the effective mid-points of the two periods are around 4 years apart. The 2000-2002 dataset has a noise level lower by a factor of two than the 1997-1998 dataset, this is a result of longer duration and better sensitivity. Data were also obtained at 450 μm, but the SCUBA filter used in 1997-1998 had a low throughput, and so this image can not be used for time-dependent studies.

The analysis made here is of the co-added 1997-1998 data compared to the co-added 2000-2002 results. The stellar proper motion is -1$''$ in RA per year, so any disc emission associated with the star should shift by approximately 4$''$ west, with some blurring because the observing periods were spread out. The diffraction-limited FWHM beam size at 850 μm was 15$''$ by 15.5$''$, but the data have been smoothed using a 7$''$ Gaussian to an effective 17$''$ beam (Greaves et al., 2005). The net pointing errors are expected to be small, below the level of the 1$''$ cell size in the images. The noise for the 1997-1998 dataset is 4.3×10^{-3} mJy arcsec^{-2} (0.96 mJy beam^{-1}) with 2.4×10^{-3} mJy arcsec^{-2} (0.54 mJy beam^{-1}) for the 2000-2002 dataset. Photospheric emission of 1.7$\pm$0.2 mJy has been subtracted from the images, for ease of comparison with simulations that neglect the star.

3.4 Simulated Data

The proper motion and rotation of dust features associated with the star can be assessed by translating and rotating the 1997-1998 and 2000-2002 co-added images to find the best match. The accuracy of the results was evaluated by comparison with simulated data with comparable noise, background galaxies and a foreground consisting of clumps embedded

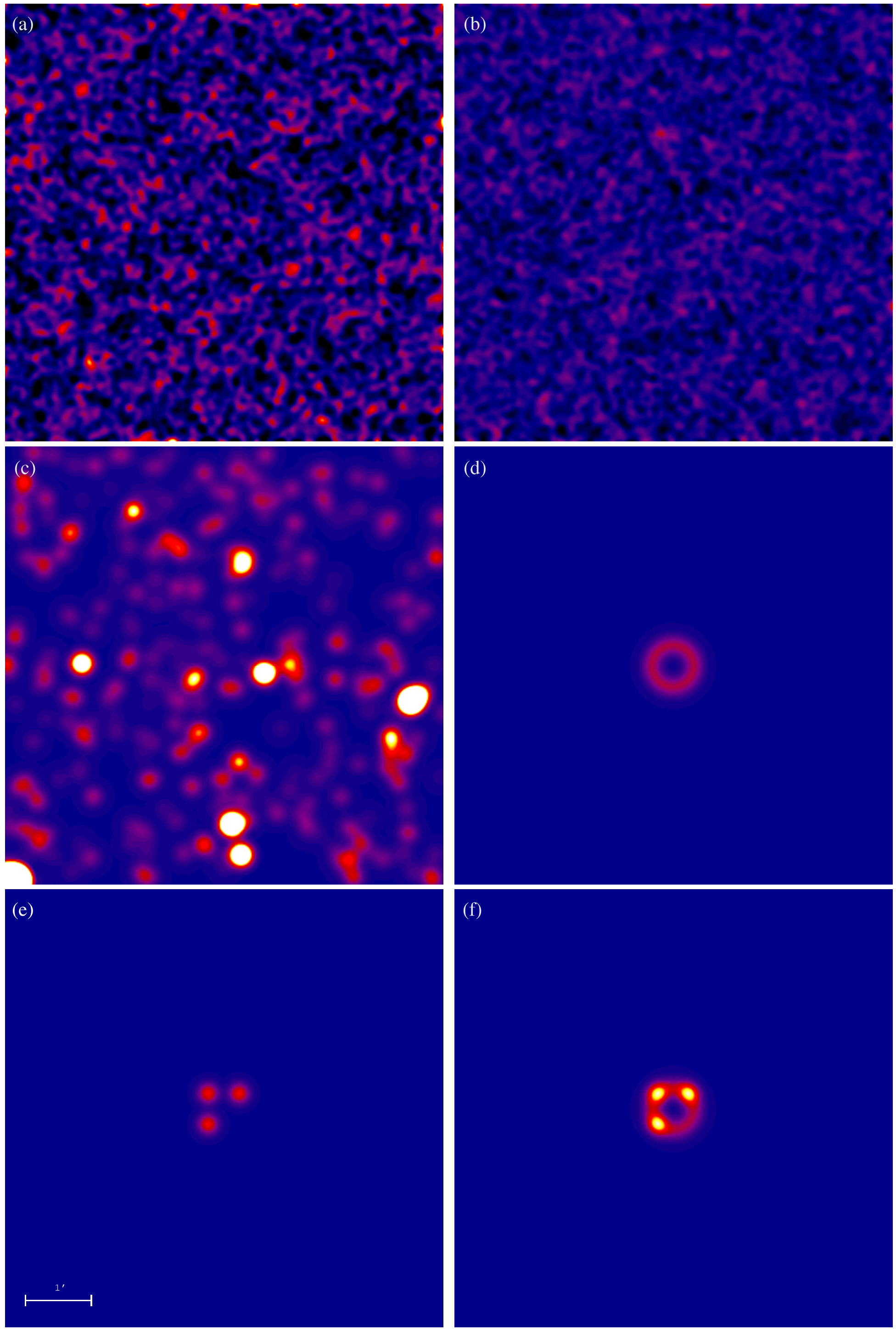

Figure 3.1: Components of a single simulated observation (a) Example of random noise component for 1997-1998 data, smoothed with a 7″ Gaussian with 1″ pixel (400 x 400) grid in R.A., δ coordinates (north is up, east is left), plotted using a linear intensity scale from -1$\times$10^{-2} to 2.5$\times$10^{-2} mJy arcsec^{-2}. (b) Example of random noise component for 2000-2002 data. (c) Example of simulated background galaxies. (d) Simulated ring. (e) Simulated clumps. (f) Total foreground (ring and clumps).

in a smooth ring of radius 20″ centred on the star.

Each simulated image was constructed from a set of frames, each representing an individual observation taken with SCUBA. The simulated analogue of the 1997-1998 dataset comprised 22 frames of equal depth, which when co-added reproduced the noise in the actual data at the final 17″ resolution. The range of proper motion offset compared to the last real data taken was 4-5″. A similar procedure was followed to simulate the 2000-2002 data, using 34 frames and a proper motion range of 0-2.5″. The difference in depths between the real 1997-1998 and 2000-2002 datasets was accounted for by both the number of images in each simulated dataset and the noise levels that were input to each set. While the number of input frames is the real value, the equal noise value per frame is a simplification (as it was too complex to simulate the duration and observing conditions of every real frame). Thus the effective mid-points of the two observing periods, about 4 years apart, may not be exactly matched in the simulated results.

Each simulated frame representing an observation by SCUBA was constructed from random noise, random background galaxies and a foreground (ring and clumps embedded in the ring) of comparable brightness to the observed data, as shown in Figure 3.1. The same background galaxies were used in both the 1997-1998 and 2000-2002 frames but a different sample was generated for each simulation. The chopping motion of the secondary mirror of the telescope used to determine sky levels was also simulated. All of these effects contribute to the real images; the data should thus represent one possible outcome of the simulations, to within the accuracy of the simplifications used.

3.4.1 Simulation details

The noise image was made by choosing the flux for each individual pixel randomly from a Gaussian distribution, smoothing spatially with a 7″ Gaussian as was performed on the observed data. This assumes the noise per 1″ pixel is statistically independent. The mean of the noise distribution was zero and the σ value was chosen so that the final simulated images had a standard deviation (measured in units of flux per beam) matching the real dataset once the galaxy population had been added.

The integral galaxy counts N(>S) for each flux, S, at 850 μm were modelled with Poisson statistics using numbers from Barnard et al. (2004), by a double power law given by

$$N(>S) \propto S^{-\alpha} \tag{3.1}$$

with α=0.94 for S < 1.18 mJy and α=2 for S $\geq$ 1.18 mJy. Each galaxy's point-like flux was smoothed with a 2-D Gaussian to reflect the size of the beam of the JCMT at 850 μm and then placed at random coordinates chosen from a uniform distribution. Thus no area of the image was favoured and any possible galaxy clustering was neglected.

The foreground was modelled by adding beam-sized 2-D Gaussian regions of flux to a ring. The ring was created by placing Gaussians at every pixel at distances between 17.5″-22.5″ from the star, producing an annulus centred on the star with the radius and width observed (Greaves et al., 2005). The flux per pixel in the ring was chosen to match the smooth level observed (i.e. between clumps) of $\approx 10^{-2}$ mJy arcsec^{-2}. Greaves et al. (2005) identified three clumps with possible rotation located northeast, northwest and southeast of the star at a radius of 20″ and thus three clumps were added at these positions in the simulated ring. The peak fluxes of the clumps were set at $\approx$1.5 x 10^{-2} mJy arcsec^{-2} so that the total foreground had peak fluxes at the clump locations of $\approx$2.5 x 10^{-2} mJy arcsec^{-2}. This is the mean of the total fluxes towards the three candidate moving clumps in the observed data (Greaves et al., 2005).

Proper motion of the disc was simulated by translating the foreground relative to the background for each of the simulated observations, by a distance corresponding to the epochs of individual real frames. In the observed data, a correction for the annual proper motion of ϵ Eridani (μ_α = -0.976″ yr^{-1}, μ_δ = 0.018″ yr^{-1}) (SIMBAD) was made by sorting and shifting the frames to a precision of 0.5″ bins in R.A. only (Greaves et al., 2005). This correction was also performed on the simulated observations, and so the background galaxies (fixed with respect to the sky) will appear to move at the rate of the proper motion but towards positive R.A., in a co-ordinate frame co-moving with the star.

Also simulated was the chopping procedure performed by the JCMT, used to remove sky fluctuations. 'Blank' regions of sky on either side of the field of interest are observed interleaved with the on-source observations, and subtracted to leave only astronomical signal; for comments on the limitations see Archibald et al. (2002). If background galaxies lie within the SCUBA field of view at either off-source position, "holes" with magnitude equal to half the brightness of the galaxies being chopped on to will appear in the final observed image. Due to variations in the chop direction, such holes will be blurred in the on-source residual frame and thus difficult to recognise. As chopping introduces extra fluctuations and modifies the background galaxy contributions, it was important to include it in the simulations.

The noise, background galaxies and foreground images were constructed for a 400 by 400 pixel square frame but the field of view of SCUBA on the JCMT is roughly circular with a radius of 72″. It was necessary to simulate this larger area of sky to allow the chopping procedure to be simulated. Flux values for each pixel within an area of sky were read into 2-D arrays at the position of the source, M, and the two off-source positions to the left, L, and right, R, of the source. The pixel fluxes used in the final images, I, were then calculated using

$$I(x,y) = M(x,y) - \frac{(L(x,y) + R(x,y))}{2}. \tag{3.2}$$

Chopping in azimuth was used for the real data, so that the left and right chop throws fell on different sky regions depending on the source elevation. This was accounted for in the simulations by varying the angle between the chop throw and the line of constant right ascension (horizontal in the images) randomly between -50° and 50°. In the observations, chop throws of 80″ (5% of images), 100″ (55%), and 120″ (40%) were used. A chop throw of 120″ was used for all of the simulated chopping.

Some small effects were neglected in the simulations: The disc is almost face-on to the observer, but inclined at ∼25° from the sky plane and so actually appears as an ellipse in the sky. Assuming a rotation rate of 2.75° per year, a clump moving along the direction of the minor axis of the ellipse will have a motion that is only ∼0.3″ less than a clump moving parallel to the major axis. Therefore, it was reasonable to approximate the ring as circular to simplify the rotation of the foreground image. The annual shifts in position due to parallax for ϵ Eridani are ±0.3″ and these were neither accounted for in the telescope tracking software nor included in the modelling. In the observed data 68% of the images co-added were taken between August-October and so the effect of smearing due to parallax errors will be less than 0.3″. The dust ring was also simulated as being centred on the star, neglecting the offset of 1.5-2″ identified by Greaves et al. (2005) and suspected to be forced by the inner planet. The bulk motions of the clumps are assumed to still follow circular orbits.

3.4.2 Simulation output

The real images are shown in Figure 3.2 and examples of the simulated images are shown in Figure 3.3. The simulated images recreate a ring with comparable brightness, size and morphology to that seen in the observations. The regions surrounding the ring also show comparable levels of noise and density of background objects. Differences between the two simulated images are at a similar level to those in the real data of Figure 3.2. Although the image structure looks complex, this is in part because the false-colour scale both includes a wide flux range (negative as well as positive signals) and also tends to enhance features with low levels of contrast, as discussed by Greaves et al. (2005).

The simulation procedure was also repeated to resemble a future observation that could be taken in 2007 with SCUBA-2 – a replacement camera for SCUBA with greater sensitivity, fidelity and field of view (Audley et al., 2004; Holland et al., 2003). SCUBA-2 is now scheduled to observe ϵ Eridani in late 2008, negligibly affecting the conclusions drawn here. For this simulation, the noise was set to zero as it will fall below the background confusion in an observation of only $\sim$1 hour. The chopping part of the simulated data algorithms was also disabled since SCUBA-2 will sample rapidly enough for sky fluctuations to be negligible and so chopping will not be required. (Chopping can be re-introduced in the data analysis where necessary for matching SCUBA-2 images of ϵ Eridani with those already taken with SCUBA.) Any candidate rotation of the disc identified here can thus be checked by extending the total timeline of observations to 10 years (from 1997 to 2007).

3.5 Clumpfind

Clumpfind is a clump finding procedure written by (Williams et al., 1994). It was initially designed to analyse the clumpy structure in a spectral line position-position-velocity data cube from radio observations of molecular clouds. However, for this clump analysis a 2D-version, rewritten in the Interactive Data Language (IDL) (courtesy of Jonathan Williams) was used.

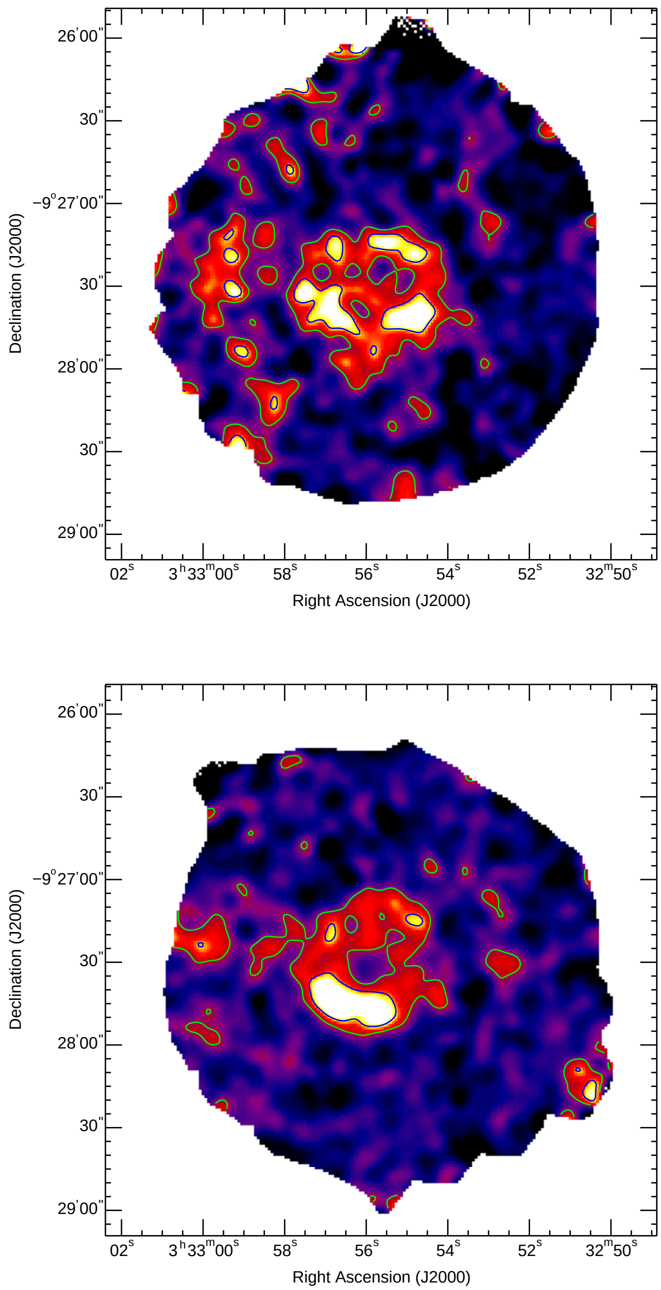

Figure 3.2: Observations of the ϵ Eridani debris disc taken with SCUBA on the JCMT. (Top) 1997-1998 dataset, (averaged over 22 images) in a $1''$ pixel grid in R.A., Dec coordinates (north being up, east being left), plotted using a linear intensity scale from -1×10^{-2} to 2.5×10^{-2} mJy arcsec^{-2}. (Bottom) 2000-2002 dataset (averaged over 34 images) with the same parameters. The green and blue contours outline regions of intensity above 1×10^{-2} and 2×10^{-2} mJy arcsec^{-2} respectively.

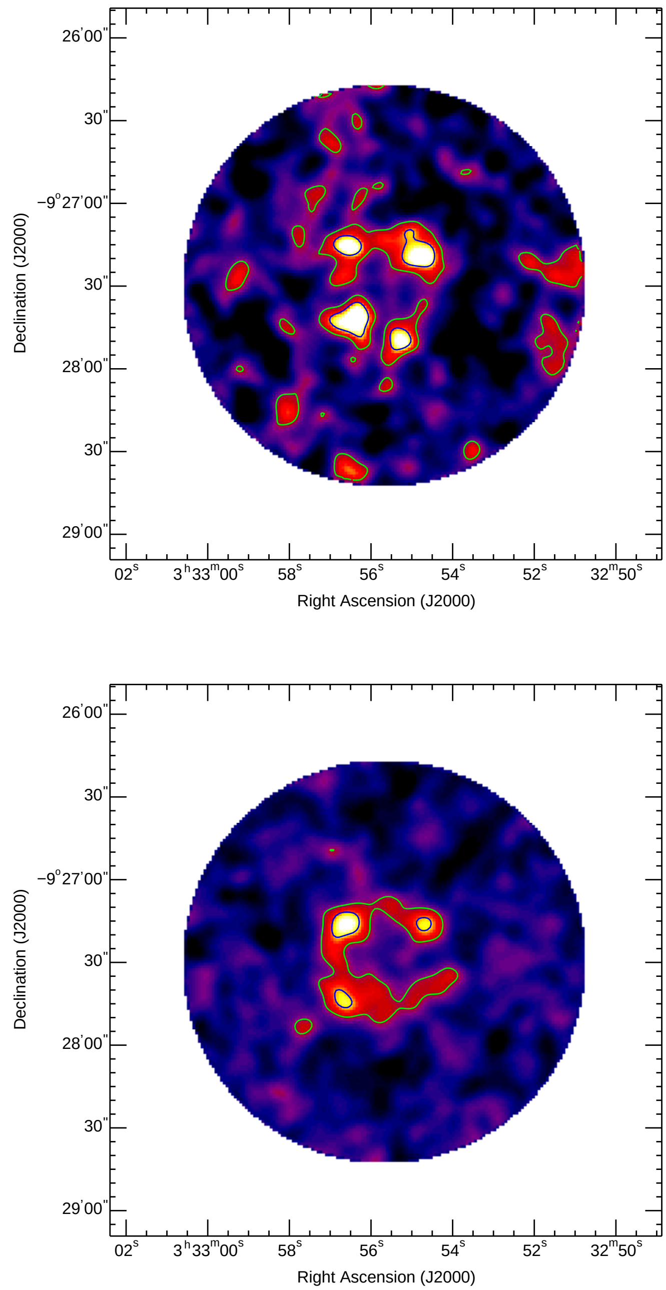

Figure 3.3: As for Figure 3.2 but for simulated SCUBA images with no rotation of the foreground clumps: (Top) example of simulated 1997-1998 image, (Bottom) the corresponding 2000-2002 image. Other parameters are as in Figure 3.2.

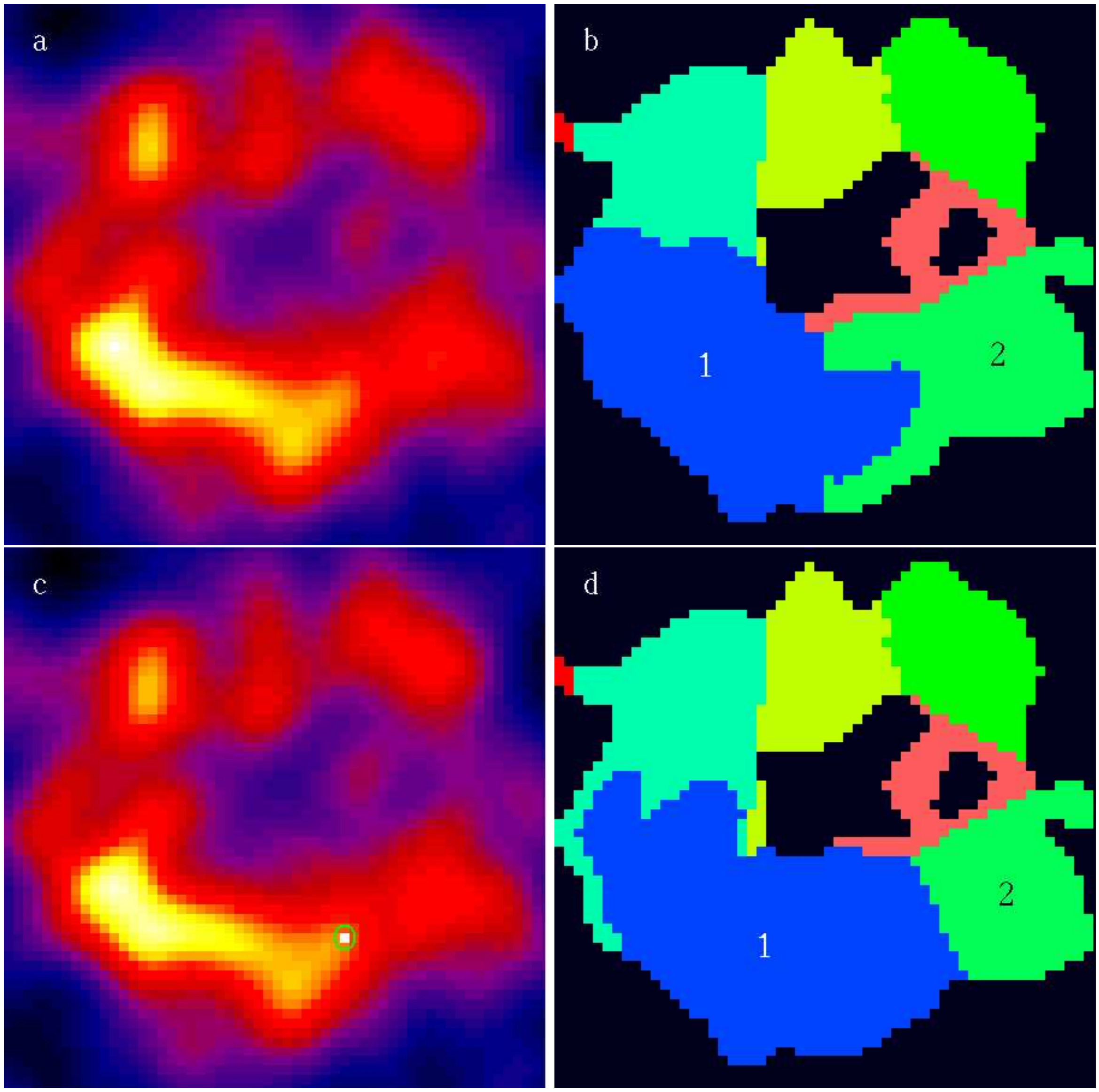

Figure 3.4: (a) Entire 850 μm dataset rebinned in $1''$ pixels in R.A., δ coordinates (north is up, east is left). (b) Clump assignment map for entire 850 μm dataset. (c) Entire 850 μm dataset but with the pixel value changed within the green circle so that it becomes the peak of clump 1. (d) Clump assignment map for entire 850 μm dataset with altered pixel value.

Clumpfind first contours the data by connecting pixels at the levels input by the user. It then identifies clumps from closed contours starting from the highest level down to the lowest. Where contours envelop a previous closed contour, the pixels between the two levels are assigned to that clump. But a more difficult situation arises when a contour surrounds two previously identified clumps. In this case, the pixels are shared using a "friends-of-friends" algorithm; the pixels are assigned to clumps based on how many of their 8 adjacent pixels (diagonals included) are already assigned to each of the clumps. The pixel is assigned to the clump to which most of its adjacent pixels belong. In the case where each competing clump has an equal number of adjacent pixels (4 each), the pixels are assigned to the clump whose peak intesity (maximum flux value) is closer.

Clumpfind outputs a clump assignment map, which is a 2D dataset with the same dimensions, but each pixel is a assigned a number instead of a flux and this denotes the clump to which it belongs. Clumpfind also writes an output log file, displaying clump properties such as position, size and flux.

Studying the clump assignment maps revealed that the "friends-of-friends" algorithm was not assigning shared pixels satisfactorily. Images (a) and (b) in Figure 3.4 show the clump assignment map created by clumpfind from the original data. The pixels on the west side of clump 1 have been incorrectly assigned to clump 2. It appears that in practice a lot of the pixels in the shared contours must have equal numbers of adjacent pixels belonging to each clump and therefore these pixels are assigned to clumps based on their proximity to the nearest clump peak. For this data, this is clearly unsatisfactory since the clumps are asymmetric and vary greatly in size, as shown in images (a) and (b) in Figure 3.4 (small clumps are favoured over larger ones, since their peaks are more likely to be closer to the pixel in question).

It was possible to test the pixel assignment by injecting data into the image using the KAPPA task CHPIX to change the position of a clump peak and observe changes in the clump assignment.This is illustrated in image (c) in Figure 3.4, where the position of the peak of clump 1 has been changed to the location incated by the green circle. After the pixel value and peak position have been changed, it is clear from image (d) that pixels are now not being assigned correctly on the east side of clump 1. This demonstrates the dependency of pixel assignment on the peak position of the clumps. As a result, Clumpfind is only reliable when clumps are clearly defined and contours are not shared.

3.6 Detecting a Rotation

The simplest method of measuring rotation would be to track individually identified clumps. However, as discussed in section 3.5, clump extraction algorithms (Williams et al., 1994; Bertin & Arnouts, 1996) are not well adapted to finding clumps and arcs within a ring. Hence, a χ^2-fitting technique was adopted instead to compare two images, with the advantage of using all the information in the image simultaneously. The χ^2 per pixel value for two images, I_1 and I_2, with measured noise σ_1 and σ_2, using only pixels in a box with its lower left and upper right corners defined by (x,y) cartesian co-ordinates (a_1, b_1) and (a_2, b_2), can be calculated using

$$\chi^2 = \frac{\sum_{x=a_1}^{a_2} \sum_{y=b_1}^{b_2} (I_1(x,y) - I_2(x,y))^2}{(a_2 - a_1 + 1)(b_2 - b_1 + 1)(\sigma_1^2 + \sigma_2^2)}. \tag{3.3}$$

The χ^2 per pixel values between the 2000-2002 dataset and the 1997-1998 dataset were calculated while the 1997-1998 dataset was shifted in right ascension and rotated relative to the 2000-2002 dataset, using the tasks "SLIDE" and "ROTATE" in the KAPPA software package (Currie, 2004). The minima in plots of χ^2 per pixel as a function of right ascension shift or rotation angle then identified the best solutions for each (independently). The region of the image included in the χ^2 fit was defined by a $70''$-square box, as this included all of the disc with as little off-source background as possible; extra background galaxies included in a larger box tend to cause the χ^2 fits to incorrectly favour a shift and rotation of zero.

For the simulated SCUBA-2 observation, the χ^2 per pixel values were calculated twice: once for the future 2007 observation compared to the 1997-1998 SCUBA dataset, and again for 2007 compared to the 2000-2002 SCUBA data. The two χ^2 values corresponding to the same shift or rotation rate were then averaged to create the final χ^2 per pixel curves. Simulations with no galaxies or noise were also performed, and verified that the true rotation values were recovered correctly.

There are three possible ways in which the regions of emission in the ring may be behaving:

1. The ring consists of only background galaxies and therefore the features are not tracking with the proper motion of the star or revolving around the star's position.

2. The ring features are tracking with the proper motion of the star but are revolving around the star at the Keplerian period of the ring which would not require a planet to explain the motion.

3. The ring features are tracking with the proper motion of the star and revolving around the star at the period of a planet at tens of AU.

To establish which of these explanations gives the best description of the data, the observed data were fitted for the proper motion of emission in the disc region, and then fitted to establish a rotation rate of the ring features. Then for comparison, 100 sets of simulated data were made with no proper motion or rotation of the foreground to quantify the random fluctuations due to noise, background galaxies and chopping on to background galaxies. This was then repeated but assuming the foreground was tracking with the proper motion of the star and with the foreground rotated at rates of $0°$ (i.e. no rotation), $1°$, $2°$, $4°$ and $10°$ per year (unrealistically large but included for comparison). The purpose of trying different rotation rates was to examine how well the true rate is recovered, given that non-moving background galaxies introduce a bias towards a χ^2 minimum around zero degrees.

3.7 Results and Discussion

Figure 3.5 shows χ^2 per pixel as a function of the annual proper motion and rotation rate of the 1997-1998 image relative to the 2000-2002 data. 5 examples of simulations are shown for comparison. Table 3.1 lists the statistics from the full sets of simulations, each set comprising of 100 comparisons of pairs of images.

3.7.1 Motion of the Disc

Figure 3.5 (left panel) shows that in the observed data, the emission in the ring region has shifted at a rate of $0.6''$ per year to the right (negative in R.A.), when tracked from the 1997-1998 to the 2000-2002 epoch. Greaves et al. (2005) argued that at least some of the disc features are tracking with the proper motion of the star, i.e. $1.0''$/yr to the right. The fact that the net motion measured is smaller may be explained by the presence of stationary background features behind the ring, which by themselves would produce a

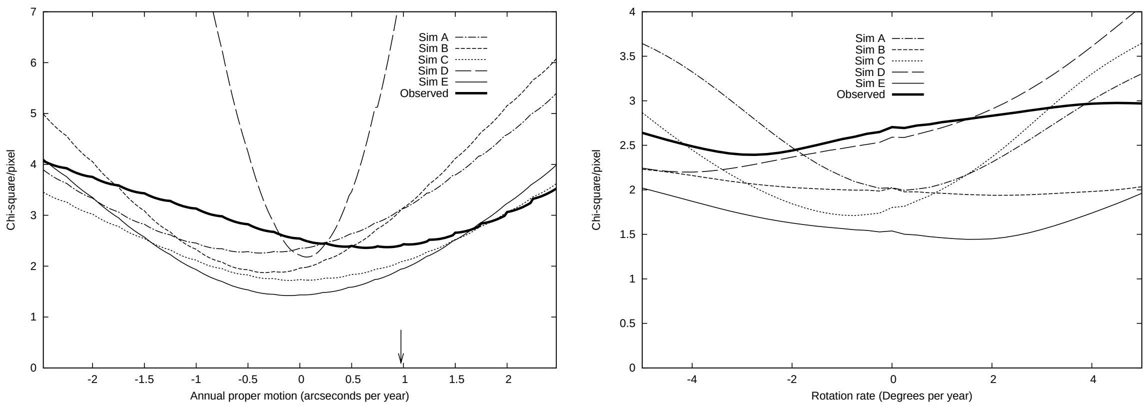

Figure 3.5: χ^2 per pixel curves for observed data and simulations. (Left) Fits for annual proper motion shift from the 1997-1998 to the 2000-2002 dataset. Thick curve shows observed data; other curves are 5 random simulations with no proper motion or rotation. Positive shifts are to the right (-ve in R.A.) and the arrow indicates the known proper motion of ϵ Eridani (μ_α = -0.976$''$ yr^{-1}). Small deviations in the curves are caused by slight imperfections in the linear interpolation. The narrow curve (Sim D) originates from a very bright galaxy in the ring, forcing a minimum that must be close to zero. (Right) Fits for annual rotation rates, comparing 1997-1998 and 2000-2002 datasets and with corrections made for proper motion. Thick curve shows observed data; thin curves are 5 random simulation pairs with proper motion corrections included but with no rotation.

minimum in the χ^2 curve at $0''$ per year. A result intermediate between $0''$/yr and $1''$/yr thus indicates a mixture of tracking and stationary features. The net value of $\approx 0.6''$/yr suggests that the majority of features in the ring region are truly associated with ϵ Eridani.

The simulations (Table 3.1) reproduce this result closely. An input proper motion of $1''$/yr is recovered on average as $\approx 0.7''$/yr of net motion (with little dependence on any assumed ring rotation). Thus the stationary galaxies do in fact reduce the net motion measured in the same sense as inferred in the real data. The standard deviation of the proper motion solutions is approximately $\pm 0.4''$/yr. Thus the real-data solution of $0.6''$/yr, differing by only $\approx 0.1''$/yr from the typical simulation result, is well within the scatter.

Further tests confirmed the validity of the simulations. When the observed data were corrected for the proper motion of the star, the solution obtained was $0.4''$ per year to the left (positive in R.A.). This is a measure of the amount of emission that is fixed in the sky and so moving to the left in the co-ordinate frame of the star. This is the value expected, as the difference between the $1''$/yr if all the emission moved with the star and the $0.6''$ actually measured. A set of simulations was also performed to check that a non-moving disc returned the correct result of $0''$ per year. The measured mean was very close to zero (Table 3.1) with a standard deviation of $\pm 0.28''$/yr. This is a measure of the fluctuations that can occur due to random noise and chopping onto background galaxies; it is somewhat smaller than the $\approx 0.4''$ obtained in the more complex cases with both stationary and moving flux contributions. Finally, it was verified that the small 'ringing' effect seen in the curves in Figure 3.5 does not affect the position of the minimum in the χ^2 curves. This ringing arises from a small jump at integer values, apparently in the bilinear interpolation of the "SLIDE" task in KAPPA. Plotting the curves using only integer values changed the average motions recovered by only $\sim 0.01''$.

Table 3.1: Proper motion shifts and rotations from χ^2 fitting of 6 simulated SCUBA datasets each consisting of 100 simulated 1997-1998 and 2000-2002 images with foreground background galaxies, noise and chopping included.

Simulation Set No.	Simulated Motion[a] ($''$ yr^{-1})	Average Motion ($''$ yr^{-1})	Motion σ ($''$ yr^{-1})	Simulated Rotation ($^\circ$ yr^{-1})	Average Rotation ($^\circ$ yr^{-1})	Rotation σ ($^\circ$ yr^{-1})	5σ Clipping Results (No. Excluded)	Average Min χ^2 Value
1	0	0.01	±0.28	0	-0.03	±1.23	5	1.92
2	+1	0.79	±0.38	0	-0.15	±1.58	4	2.03
3	+1	0.78	±0.42	-1	-0.68	±1.83	5	2.03
4	+1	0.73	±0.44	-2	-0.96	±1.87	2	2.06
5	+1	0.65	±0.47	-4	-1.92	±2.55	7[b]	2.14
6	+1	0.63	±0.47	-10	-4.83	±13.71	-[c]	2.42

[a] Positive values signify a direction negative in R.A.

[b] 4σ clipping used for these values

[c] σ clipping not possible due to broad distribution of results

3.7.2 Rotation of the Disc

The χ^2 fit between the observed 1997-1998 and 2000-2002 datasets (corrected for proper motion) shows a rotation of $\approx$2.75° per year counterclockwise (see Figure 3.5, right panel). This is in the same direction as but somewhat larger than the rotation of $\sim$1.5° suggested by Greaves et al. (2005). It is also larger than the rotation rate of 0.7°-1.3° per year predicted by Ozernoy et al. (2000) and Quillen & Thorndike (2002), assuming dust is trapped in resonances with a planet at $\approx$40-60 AU from the star. The Keplerian rate for clumps orbiting at $\approx$65 AU radius is 0.65° per year for a 0.9 $M_\odot$ star.

The simulated data are used as a guide to what rotation rates can be confirmed or ruled out. In the simulation results (Table 3.1), the χ^2 fit results from sets of 100 image-pairs showed that the rotations obtained were approximately Gaussianly distributed, for the cases where the rotation rate was 0°, 1° and 2° per year. There were, however, a few spurious results which involved an unphysical disc feature rotation rate (total rotations of >50°). These results occurred when a bright clump was randomly generated by the combination of noise and background galaxies and was fortuitously positioned in the dust ring to give a deeper minimum in the χ^2 curve corresponding to a large rotation angle. These outcomes ($\leq$ 5 per set of 100 simulations) did not fit into the Gaussian distribution and were removed by clipping at the 5σ level. After removing these points, the sample standard deviation was typically $\sim$1.5° of rotation per year. For rotation rates of 4° and 10° per year, the rotations obtained followed a broader distribution, and so no reliable measure of the rotation was obtained.

The true rotation rate is generally not recovered in the simulations, with an average annual rotation measured generally as about half of the input rotation. This can be understood as the effect of the stationary galaxies, which will introduce a bias towards a solution of zero. (When no rotation is input, a solution close to zero is in fact recovered.) Only simulations in roughly the -1σ tails of the distributions recover the true input rotation rate (Table 3.1). There is therefore a moderate probability that the rate measured in the real data, of $\approx$2.75° per year, is actually an underestimate for the true value.

Table 3.1 shows that for the simulated data with no rotation of the foreground, the sample standard deviation was 1.44° per year. As the measured rotation was 2.75° per year, this means that the null hypothesis (zero or very slow ring rotation) is ruled out at the $\approx 2\sigma$ level. However, the actual rotation rate can not be extracted from comparison with the simulations as the results overlap; that is, the standard deviations are wider than the changes in mean value between sets with different input rotation rates. Some estimate can be made of how plausible a measured rotation rate of 2.75° anticlockwise is within each simulation set. The probability of measuring at least this large a counterclockwise rotation is found to be 10-25% for rotation rates of 1-4° per year.

Tests were made to see if any further observational constraints reduced the simulation parameter space. In the real data, the brightest signal is 10 mJy within one beam. Galaxies brighter than this within the 70″ box are predicted to occur in only ≈5% of the simulations. Eliminating these might reduce the tendency towards solutions of zero rotation, but in fact an increase of approximately 20% was the largest change to any recovered rotation rate when this was done.

It was also verified that small defects seen in the curves about zero, probably arising from interpolation in the rotation process, did not significantly change the results. Removal of the defects only changed the rotation rate recovered of the non moving, non rotating case and only by ∼0.001° per year and the associated standard deviation by only ∼0.004° per year.

3.7.3 Future Observations

Table 3.2 shows the results for the simulated datasets with a third image with no noise included. This is intended to reflect observations that could be made with SCUBA-2 at 850μm in 2007, with noise that is negligible compared to random background galaxies. Chopping was re-introduced to allow matching of SCUBA and SCUBA-2 images, although testing showed that this only sigificantly reduced the random fluctuations in the minima in the 4° and 10° per year cases. The χ^2 minima were found by comparing this simulated SCUBA-2 dataset with the two simulated SCUBA predecessors, as described above. The projected 10-year timeline should refine the solutions for the disc motions, and so the annual errors are expected to be reduced.

Table 3.2: Proper motion shifts and rotations from χ^2 fitting of 6 simulated datasets including the SCUBA frames of Table 1 and a SCUBA-2 image to be obtained in 2007 (for which no noise is included).

Simulation Set No.	Simulated Motion[a] ($''$ yr^{-1})	Average Motion ($''$ yr^{-1})	Motion σ ($''$ yr^{-1})	Simulated Rotation ($^\circ$ yr^{-1})	Average Rotation ($^\circ$ yr^{-1})	Rotation σ ($^\circ$ yr^{-1})	5σ Clipping Results (No. Excluded)	Average Min χ^2 Value
1	0	0.00	$\pm$0.07	0	-0.05	$\pm$0.26	0	2.05
2	+1	0.81	$\pm$0.21	0	0.05	$\pm$0.64	0	3.07
3	+1	0.78	$\pm$0.22	-1	-0.52	$\pm$0.68	0	3.19
4	+1	0.75	$\pm$0.22	-2	-1.04	$\pm$1.08	1	3.11
5	+1	0.76	$\pm$0.25	-4	-2.48	$\pm$1.79	1	3.44
6	+1	0.76	$\pm$0.25	-10	-3.70	$\pm$6.00	-[b]	4.52

[a]Positive values signify a direction negative in R.A.

[b]σ clipping not possible due to broad distribution of results

The proper motion is now recovered at similar mean values to before ($\approx$0.7$''$ per year) but with lower standard deviations. The errors of $\approx \pm 0.25''$/yr are similar to the SCUBA-only non-moving simulation, suggesting this is a limit set by the fluctuations within the two SCUBA datasets from 1997-1998 and 2000-2002. The input rotation is not recovered more reliably than before but the dispersion of the results is smaller, significantly so in the cases of up to 2°/yr rotation. The number of doubtful results with very large rotations is also reduced (Table 3.2). However, the distributions of rotation values still overlap between different input rates, and so addition of a third-epoch SCUBA-2 image would not uniquely identify the true rotation rate. In fact, eliminating noise by comparing two hypothetical future SCUBA-2 observations, with mid-points 4 years apart, still did not resolve this ambiguity. It is concluded that χ^2 fitting alone can not identify an orbital period; the paradox inherent in trying to fit both moving and non-moving components with one rotation rate is likely to be responsible.

With the inclusion of the SCUBA-2 epoch, the case of no rotation could be ruled out at the $\approx 4\sigma$ level. The average rotation rate recovered was +0.04° per year with a sample standard deviation ±0.74°. Hence if the rotation rate of −2.75° per year estimated from the present data were to persist, this would be around the -4σ bound of this simulation. Further, a rotation rate of $\geq$1°/yr would be confirmed at around the 3σ level: that is, a continuing measurement of −2.75° per year would be just within the -3σ tail of the simulation with an input rate of 1°/yr. This would support the hypothesis that clumps orbit faster than the Keplerian rate at $\approx$65 AU radius, which is 0.65° per year for a 0.9 $M_\odot$ star.

It may also be possible to observe at 450 μm with SCUBA-2 and the improved resolution of 8$''$ at this wavelength may allow the rotation to be constrained more accurately. This would be optimised with two epochs of SCUBA-2 data a few years apart, and also a better knowledge of the galaxy counts at 450 μm. Observations of ϵ Eridani are now planned in SCUBA-2 guaranteed time so the timeline covered by the 450 μm data will span from 2000-2002 with SCUBA to late 2008.

3.8 Conclusions

A motion of the ϵ Eridani disc consistent with features tracking in the same direction as the proper motion of the star has been identified. The best fitting proper motion $\mu = 0.6'' \pm 0.4''$ per year is most probably less than the star's proper motion of $1''$ per year, suggesting that some of the features in the vicinity of the disc are likely to be background galaxies. The measured rotation rate of 2.75° per year counterclockwise is in the same direction but nearly twice as large as that suggested by Greaves et al. (2005); it could also be an underestimate as stationary galaxies tend to bias the rotation solution below the real amplitude. Comparisons with simulated data show that the measured rotation is significant at the $\sim 2\sigma$ level, and a future image with SCUBA-2 in 2007 could rule out no or very slow rotation at the $\sim 4\sigma$ level. The technique of χ^2 fitting is inherently limited by trying to find one solution that fits both stationary galaxies and moving ring features, hence a method that identifies individual clumps or a method capable of using the proper motion to distinguish the foreground and background images will be needed to measure the true rotation rate. This may be possible using the new CUPID (A Clump Identification and Analysis Package) software developed for SCUBA-2 (Berry et al., 2007).

Radial velocity detections of a planet are restricted to finding planets out to only a few AU from the star. In the case of ϵ Eridani, finding a planet out to tens of AU via radial velocity measurements will be extremely difficult since the period of the planet is deduced to be >100 years, and the magnitude of the Doppler wobble is reduced by the nearly face-on inclination ($\sim 25°$) of the disc. However, this viewing angle also means that ϵ Eridani provides a unique opportunity to track the motion of the substructure within the disc. This is the first ever analysis attempting to track clumps rotating in a dusty disc. Future observations with SCUBA-2 can confirm the rotation of clumps in resonance with a planet at tens of AU, while imaging with submillimeter interferometers such as SMA and ALMA could radically shorten the timescale to identify such motions.

CHAPTER 4

A Survey of Young Stellar Objects in the Rosette Molecular Cloud

This chapter is based on a paper published in Monthly Notices of the Royal Astronomical Society by:
Poulton, C.J., Robitaille, T.P., Greaves, J.S., Bonnell, I.A., Williams, J.P., Heyer, M.H. (2008, MNRAS, 384, 1249)

4.1 Abstract

A survey of the Rosette Molecular Cloud (RMC) using both the Infrared Array Camera (IRAC) and Multiband Imaging Photometer for Spitzer (MIPS) onboard the Spitzer Space Telescope is presented. A region of active star formation covering an area approximately 1° by 1.5° including several previously known clusters was mapped. Spectral energy distributions (SEDS) fitted to the data combined with that from 2MASS were used to identify Young Stellar Objects (YSOs) with infrared (IR) excesses. It was found that roughly 50% of the sources are forming in clustered environments and 7 clusters of IR excess sources were identified including 4 that were previously unknown. The ionisation front associated with the young open cluster NGC 2244 is identified in Brackett-α emission and the evidence for triggering of star formation associated with its expansion is investigated. Although the position of several of the clusters of IR excess sources are coincident with the ionisation front, the bulk of the youngest YSOs are located far from the ionisation front, in clusters located along the midplane of the cloud. Although triggering from the HII nebula is a possible origin for some of the recent star formation, the majority of the active star formation is occurring in already dense regions of the cloud not compressed by the

expansion of the HII region.

4.2 Introduction

4.2.1 The Collect and Collapse Model

As an HII region expands, it compresses the molecular cloud into a dense ridge at the nebula/cloud interface. This ridge is subject to fast instabilities occurring on short timescales due to kinematic, gravitational and magnetic processes and also to the long timescale gravitational collapse. The result is fine scale structure produced by the short timescale instabilities which are pulled together into cores by the long timescale gravitational collapse along the ridge. Miyama et al. (1987) showed that the collapse first produces filaments within which the cores form. The cores produced will generally contain enough mass that cluster formation rather than individual star formation will follow. Elmegreen (1985, 1992) showed that when the cloud is compressed in one dimension and then collapses in a perpendicular direction, the core density of the cores is predicted to be greater than the initial density of the cloud by a factor C^3, where C is the one dimensional compression factor. The resulting mechanisms governing the collapse of the cores are expected to be the same but the whole process accelerated due to the enhanced densities produced by the compression.

The internal motions within the ridge act to delay the gravitational collapse so star formation will only occur a significant period of time after the formation of the ionising cluster and when the HII region began expanding. The observational signature of the "collapse and collect" model is therefore to observe young stellar objects of a similar age at the nebula cloud interface, much younger than the stars in the ionising cluster with no stars of an intermediate age in between. However, this is complicated by several factors:-

- The small timescale instabilities can sometimes form self gravitating clumps that will move off the front of the layer and appear ahead of the ionisation front. This occurs because the deceleration of the front is greater than the self-gravitational acceleration perpendicular to the front (Elmegreen, 1989; Nishi, 1992).
- Bulk motion of the cores formed can cause them to collide or merge with pre-existing clumps and also pre-existing clumps can cause irregularities in the shock front. The

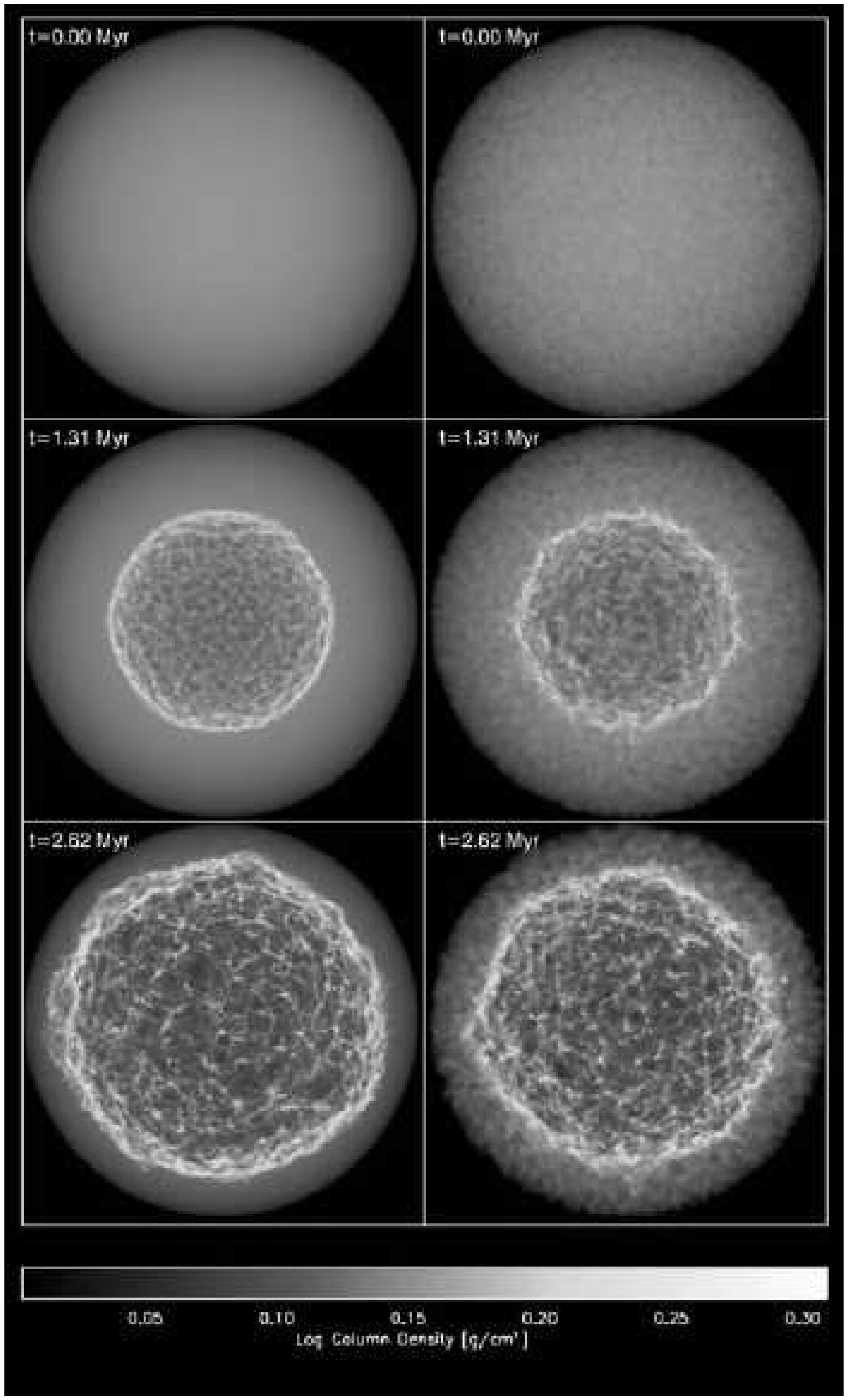

Figure 4.1: Figure 5. Comparison of column-density maps (viewed along the line of sight) from an SPH simulation using 1.3 10^6 particles for three epochs of an HII region expanding into a smooth (left column) and noisy (right column) medium. (Figure from Dale et al. (2007a)).

latter leads to transverse motions leading to the formation of large clumps in the ridge without the action of self gravitation, i.e. cores form sooner than they would were the expansion into a smooth medium.

- Parts of the cloud are compressed in a direction not entirely perpendicular to the observers line of sight and what is observed is a two dimensional projection of a three dimensional front. Therefore, at least some triggered cluster formation should appear to occur within the cloud.

Smoothed particle hydrodynamics (SPH) simulations of the "collect-and-collapse" model into a medium with local fluctuations in density of a factor of 2 in the initial gas distribution show that self gravitating cores are formed both along and behind the nebula cloud interface (see Figure 4.1). Deharveng et al. (2005) surveyed 17 HII regions and found signatures of induced star formation at the nebula/cloud interface for Sh 104 and RCW 79 but not behind the expanding front.

4.2.2 The RMC as an example of triggered star formation.

The Rosette Molecular Cloud (RMC), at a distance of 1600 pc, is a well known region of active star formation and has been the subject of many studies (e.g. Blitz & Thaddeus (1980); Cox et al. (1990); Block et al. (1993); Williams et al. (1995); Phelps & Lada (1997); Heyer et al. (2006)). It has been cited as an example of sequential triggering of star formation (Elmegreen, 1998) as proposed by Elmegreen & Lada (1977); Lada (1987) due to the compression of the cloud by the expanding HII region associated with NGC 2244, a young open cluster at the centre of the Rosette nebula. The evidence supporting this claim is the presence of several embedded clusters located along the ionisation front (Phelps & Lada, 1997) as well as further into the cloud, appearing to form in a structured manner (Li & Smith, 2005b). The main aim of this chapter is to assess to what extent the "collect and collapse" triggering process can account for the star formation currently observed in the Rosette Molecular Cloud.

4.2.3 Fitting to model SEDs

New data from the Spitzer Space Telescope and the Two Micron All Sky Survey (2MASS) provides wavelength coverage from 1 to 70 μm with improved sensitivity and resolution than that of previous infrared observatories. This allows surveys of sources in star forming regions to identify Young Stellar Objects (YSOs) with infrared excesses.

In this chapter, the observed fluxes are fit using a large number of precomputed SED models covering a large range of stellar masses and evolutionary stages (Robitaille et al., 2006). This method has the merit of using all of the available information and quantifies the uniqueness of fit by establishing the range of parameters that can be used to model the SED of each source.

Values for physical parameters for each YSO are derived by fitting the data to YSO SED models. The stage classification scheme described by Robitaille et al. (2006) is adopted and is based on physical parameters but is intended to be analogous to the traditional classification scheme of Lada (1987) to distinguish between the evolutionary stages of each YSO. These evolutionary stages are defined not by the slope of the SED but from the range of envelope accretion rates and disc masses computed for each YSO candidate. It is therefore possible to estimate the evolutionary stage of the YSOs in the field and attempt to differentiate between sources with envelopes (Stage I) and those with dusty discs only (Stage II). It is important to note that a Stage II object viewed edge-on may exhibit a SED consistent with a Class I object using the classification scheme of Lada (1987) but will likely be fainter than other IR excess sources nearby. Similarly, an object classified as Stage I using physical parameters viewed pole-on may exhibit a Class II SED. For a large number of sources the data can be fit with either a Stage I or II SED and these ambiguous cases are referred to as Stage I/II.

The boundaries between stage classifications in this system are somewhat arbitrary, as is the case for the original classification scheme but the aim is the same, that is to distinguish between young stars with disks and envelopes, young star with disks only and stars with no disks (no IR excess). The relative number of sources occupying each stage is found to be approximately consistent with those determined from colour-colour plots using IRAC colours Allen et al. (2004) and the numbers in each stage also consistent with the period that each protostar is predicted to spend in each class.

Since the primary objective of this chapter is to assess to what extent the star and cluster formation in the Rosette Molecular Cloud is induced by the expanding ionisation front from NGC 2244, a simpler distinction is employed. The youngest sources are identified as those with SEDs that can only be fit with models that have an envelope accretion rate greater than 0, approximately equivalent to Class I sources.

Using this information, any significant clusters of IR excess sources are identified and the number of these sources that appear to be forming in relative isolation is calculated. The evidence for triggered cluster formation in the RMC instigated by the expansion of the HII region around NGC 2244 as suggested by Phelps & Lada (1997) is examined.

4.3 Observations and Data Reduction

The Rosette Molecular Cloud was surveyed with both the Infrared Array Camera (IRAC) in bands 1 (3.6 μm), 2 (4.5 μm), 3 (5.8 μm) and 4 (8.0 μm) and the Multiband Imaging Photometer for Spitzer (MIPS) at wavelengths of 24 μm and 70 μm. The region mapped was approximately 1° by 1.5° and covered the region to the southwest of NGC 2244, previously mapped in ^{13}CO (Williams et al., 1995) and also J, H and K bands by Phelps & Lada (1997). Coverage of NGC 2244 using IRAC and MIPS was also recovered from the Spitzer archives (Fazio, 2005; Balog et al., 2007).

Archived photometry for the region surveyed was also retrieved from the Two Micron All Sky Survey (2MASS) at wavelengths in the J (1.24 μm) , H (1.66 μm) and K_s (2.16 μm) bands. The ^{13}CO $J = 1 - 0$ datacube from Heyer et al. (2006) was used to trace H_2 column density and examine the clumpy structure of the cloud and the dynamics of the gas.

4.3.1 IRAC

The exposure time for each 5.2' x 5.2' IRAC frame was 12s and three dithered integrations were obtained for each position giving point source completeness down to 0.6, 0.5, 0.6 and 0.7 mJy for the IRAC bands 1-4 respectively. This corresponds to completeness down to stellar masses of 0.2, 0.2, 0.3 and 0.4 $M_\odot$ in each IRAC band, based on the fluxes of the models in Robitaille et al. (2006). The mean full width at half-maximum (FWHM) of the Point Response Function (PRF) from observations of a star at 25 different locations on the array is 1.66″, 1.72″, 1.88″ and 1.98″ for IRAC bands 1, 2, 3 and 4 respectively[1]. Preprocessing was also executed on the basic calibrated data (bcd) frames of the IRAC data

[1]Spitzer Observer Manual, http://ssc.spitzer.caltech.edu/documents/som/

as described in Chapter 2. Given the uncertainties in point source extraction, photometric corrections up to ≈10% (e.g. array location) were included whilst smaller errors such as the 2% effect associated with the source position within a pixel were neglected.

4.3.2 MIPS

The exposure time was 30s for each 5.2' x 5.2' MIPS 24 μm frame and was 10s for each 5.2' x 2.6' MIPS 70 μm frame. Point source extraction was complete down to 2 mJy for the MIPS 24 μm band and sources were detected down to ≈100 mJy in the MIPS 70 μm band. The telescope point spread function (PSF) full width at half maximum is 6$''$ at 24 μm and 18$''$ at 70 μm. Removal of latents in the MIPS data was achieved using the Image Reduction and Analysis Facility (IRAF) by division of the individual frames with the median image calculated with values from the same array positions in all the frames.

Data taken near the ecliptic plane are likely to include asteroids, which can be confused with reddened YSOs and are visible in the MIPS 24 μm image. The regions imaged here lie approximately 4° from the ecliptic plane and thus the presence of asteroids is possible. Asteroids can be distinguished from YSOs by blinking between frames taken in two different epochs to reveal their rapid motions across the sky. Thus it was confirmed that all of the YSO candidates identified were not asteroids.

Non-filtered images were used to create a MIPS 70 μm mosaic. This meant that some small artifacts were not removed from the data but ensured that the photometry in regions of extended emission was preserved and thus could be used to obtain upper limits at 70 μm. The coverage in the MIPS 70 μm data is incomplete due to a cabling problem that compromised the outputs of half the array and a large time lapse, during which the spacecraft orientation changed between subsequent observations; this effect has produced holes in the final mosaic.

4.4 Point Source Extraction and Bandmerging

The Spitzer Mosaicking and Point Source Extraction (MOPEX) package (Makovoz et al., 2006) was used for background matching and also to remove cosmic radiation hits via dual outlier detection (spatial and temporal filtering). MOPEX was also used to mosaic the frames together to produce the final images and for point source detection. Point source detection was performed on a background subtracted signal-to-noise ratio image where the Gaussian noise was estimated using a 45 by 45 pixel sliding window. This allowed sources to be reliably detected in regions with bright diffuse emission.

Point source estimation was performed by PRF (Point Response Function) fitting of the detected sources using a custom program that used the detection list from MOPEX for IRAC band 1 to find sources in the rest of the IRAC bands and the MIPS 24 μm mosaic. When a source detectable in IRAC band 1 was not detectable in other bands, an upper limit was calculated at those coordinates. MIPS 70 μm fluxes and upper limits were estimated using only the positions of the MIPS 24 μm sources.

A custom program was written for bandmerging, requiring point sources in different bands to lie within 2 pixels of each other (2.4$''$ for 2MASS and IRAC bands, 4.9$''$ for MIPS 24 μm and 8$''$ for MIPS 70 μm) to be matched. For IRAC sources with no corresponding MIPS 24 μm source upper limits for the MIPS 24 μm flux were established as these still proved useful in constraining the SED and thus the parameter space occupied by each source.

4.5 Identification and Classification of YSOs

The final IRAC and MIPS 24 μm mosaics are shown in Figure 4.2. Figures 4.3 and 4.4 show detailed images of the regions around the 7 clusters identified by Phelps & Lada (1997) and are referred to as clusters PL1-7 in this paper.

IRAC band 4 covers a wavelength range including several Polycyclic Aromatic Hydrocarbon (PAH) emission features and the IRAC band 2 coverage includes the Brackett α transition at 4052.5 nm. A normalised difference image was created by scaling and then subtracting the IRAC band 4 image from the IRAC band 2 image using a similar method to that described in Terebey et al. (2003). The HISTAT and CDIV commands in the starlink software package KAPPA were used to find the median pixel values in each image (0.85 and 23.04 for IRAC bands 2 and 4 respectively) and scale the IRAC band 4 image (by multiplying the pixel values by a factor of 0.85/23.04). The resulting image is shown in Figure 4.5 and traces Brackett α emission, indicating the position of the ionisation front associated with NGC 2244.

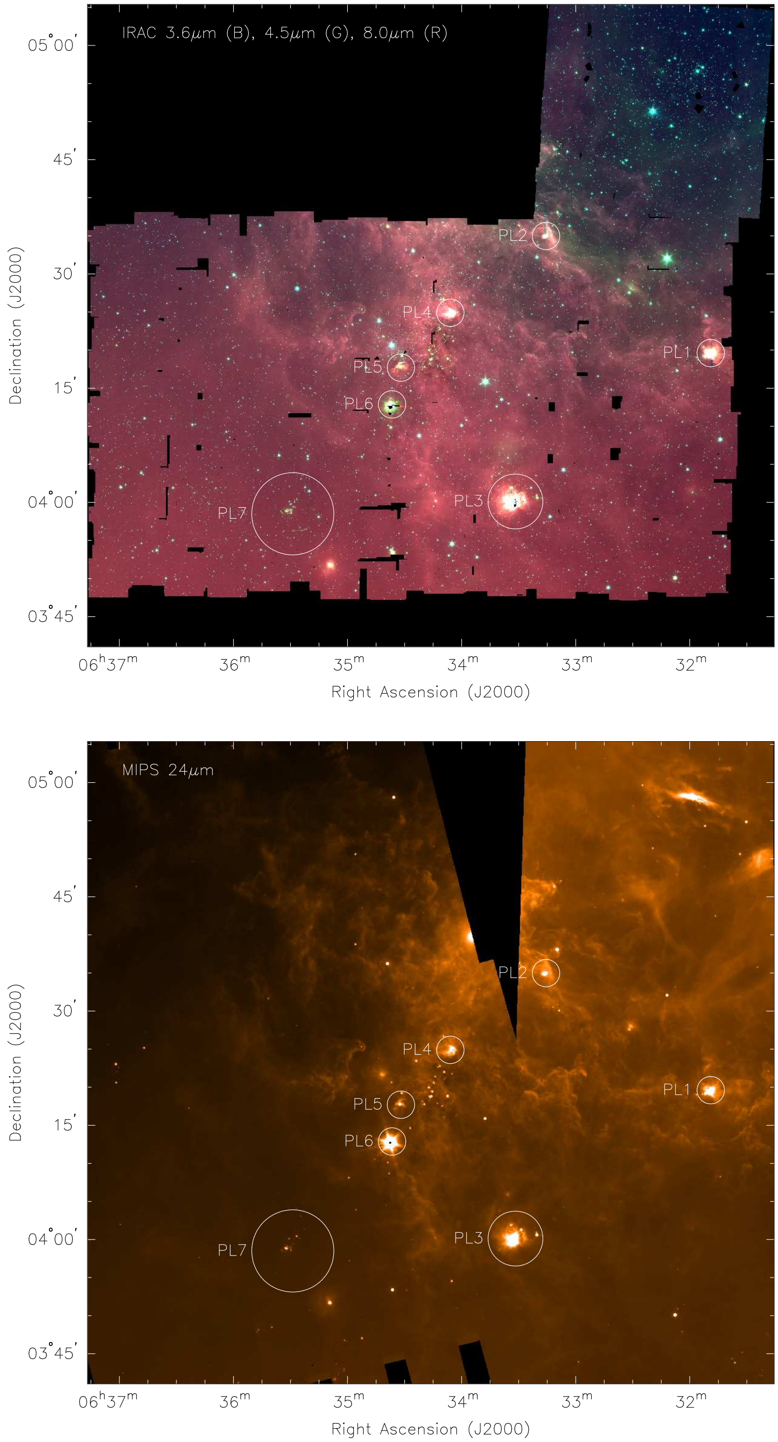

Figure 4.2: Top panel: False colour IRAC image of NGC 2244 and the Rosette Molecular Cloud, Blue: IRAC band 1 (3.6 μm) Green: IRAC band 2 (4.5 μm) and Red: IRAC band 4 (8.0 μm) Bottom panel: MIPS 24 μm mosaic of the Rosette Molecular Cloud. Insets indicate the positions of the clusters identified by Phelps & Lada (1997) and are shown in more detail in Figures 4.3 and 4.4.

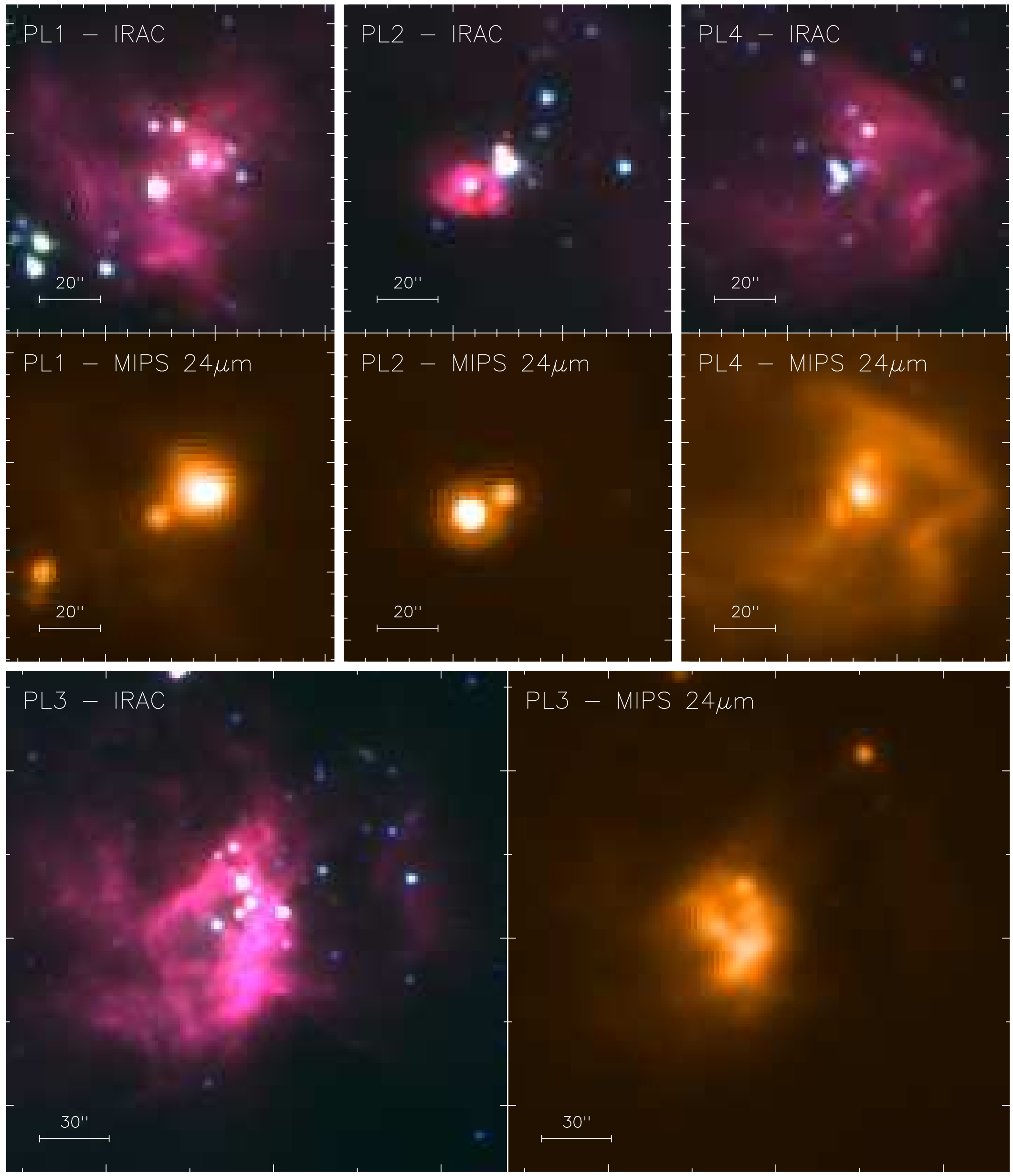

Figure 4.3: Detailed images of the regions around clusters PL1-4 as identified by Phelps & Lada (1997) with positions indicated in Figure 4.2. The IRAC data is depicted in false colour images; Blue: IRAC band 1 (3.6 μm), Green: IRAC band 2 (4.5 μm) and Red: IRAC band 3 (5.8 μm)

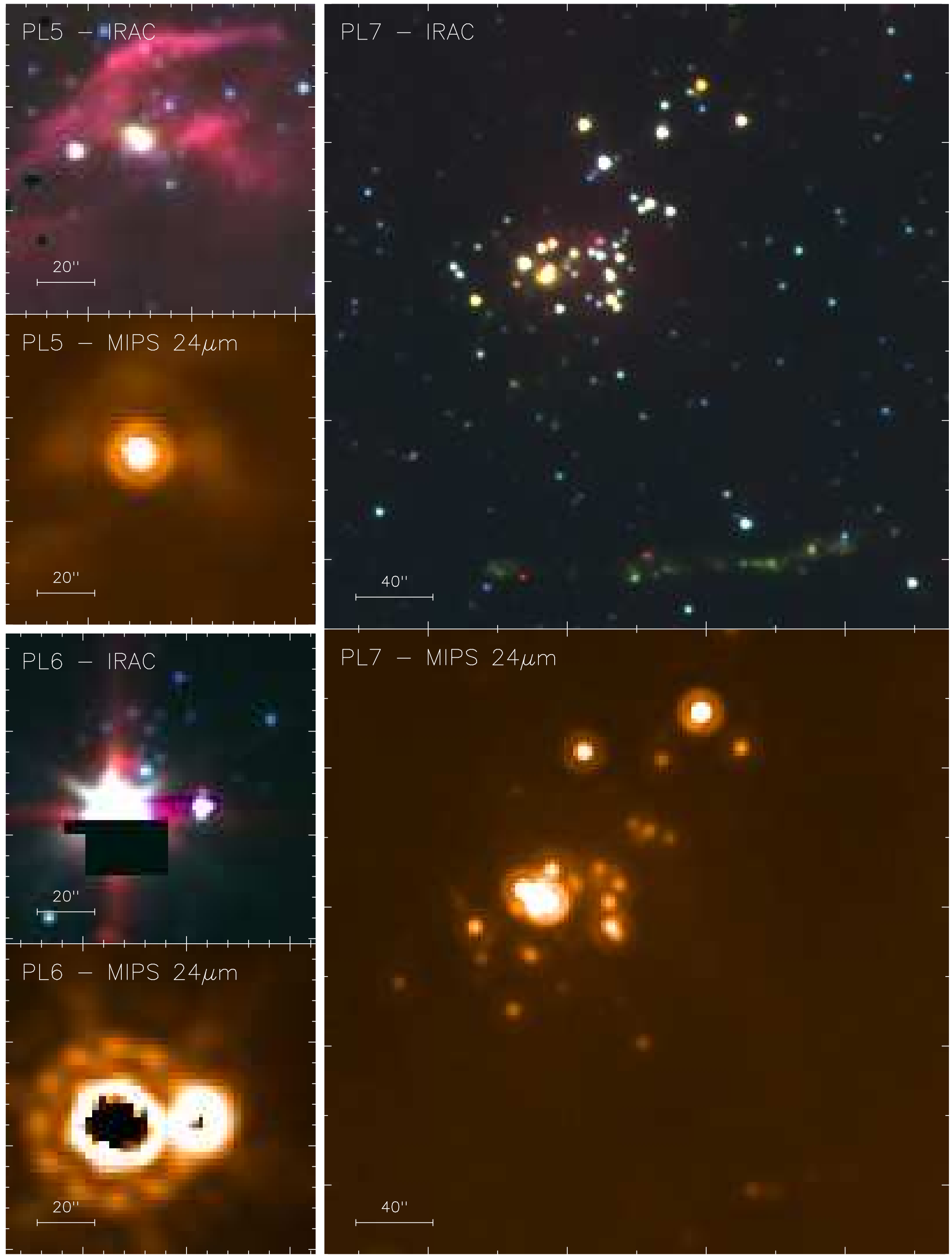

Figure 4.4: Detailed images of the regions around clusters PL5-7 as identified by Phelps & Lada (1997) with positions indicated in Figure 4.2. The IRAC data is depicted in false colour images; Blue: IRAC band 1 (3.6 μm), Green: IRAC band 2 (4.5 μm) and Red: IRAC band 3 (5.8 μm). An outflow appears to be visible in the IRAC image below cluster PL7. Blank pixels in the IRAC images for clusters PL5 and PL6 result from incomplete coverage. Blank pixels in the MIPS image for cluster PL6 result from saturation by the bright source AFGL 961.

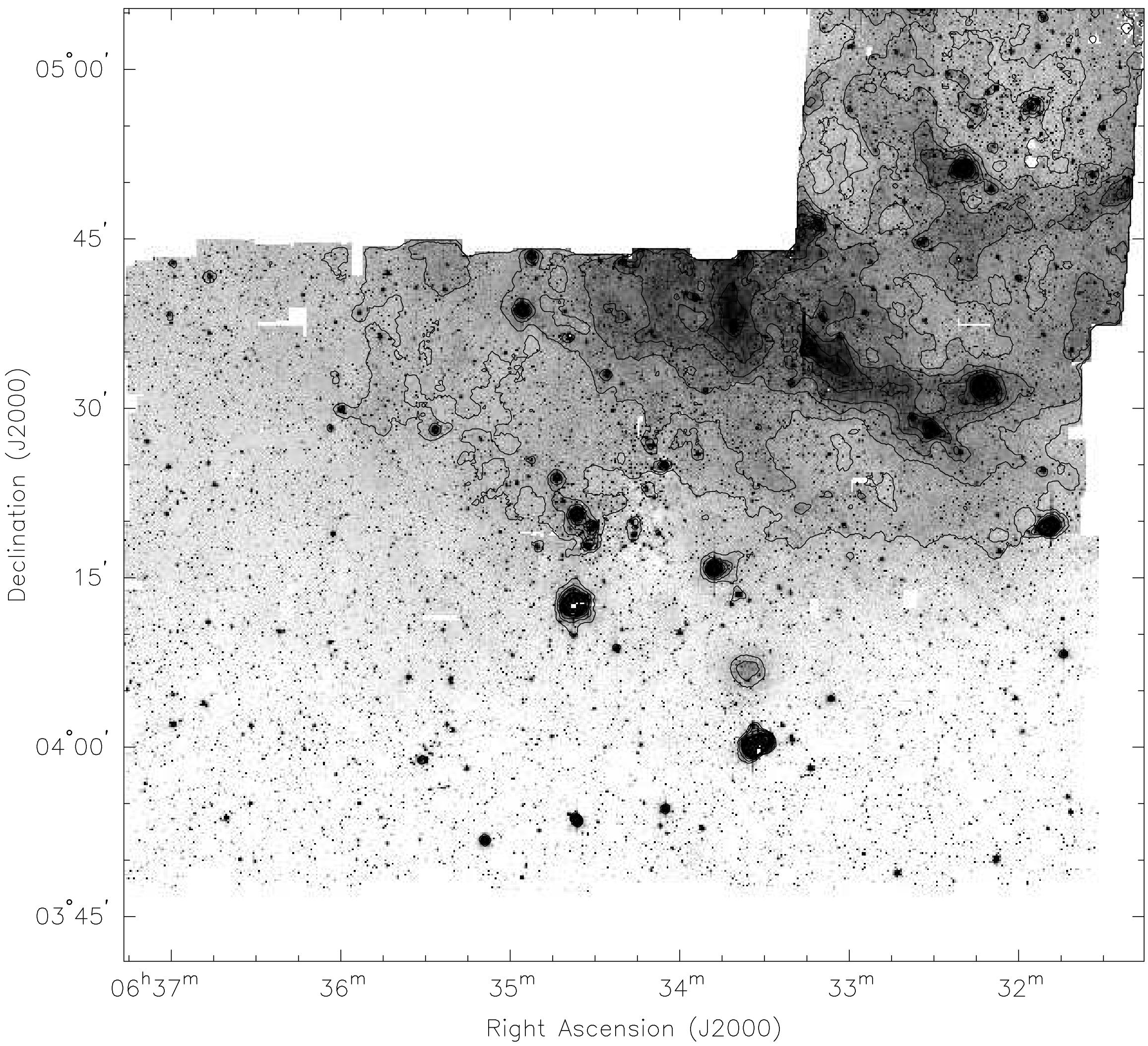

Figure 4.5: Normalised difference image created by subtraction of a scaled IRAC band 4 image from the IRAC band 2 image. Image is shown using reverse grey-scale with contours; dark areas indicate regions of bright H Brackett α emission and trace the ionisation front associated with the open cluster NGC 2244, located at 6h31m52.80s +4d55m48.0s.

4.5.1 SED Fitting

In the subsequent analysis, any fluxes with a signal-to-noise lower than 5 in JHK and IRAC 3.6 and 4.5 μm, and lower than 10 in IRAC 5.8 and 8.0 μm are discarded. Any IRAC fluxes where the position of the source was within 3 pixels of a saturated or blank pixel were also discarded, since saturated pixels often produce artifacts in nearby pixels that can result in false point sources being detected. Fluxes measured from sources including or near saturated pixels are also underestimated. As the observations were not taken in high dynamic range mode these fluxes could not be easily be corrected and therefore were not used when bandmerging.

For the purposes of SED fitting only sources with at least four valid fluxes out of JHK, IRAC and MIPS 24 μm were considered. The SED fitting tool described in Robitaille et al. (2007) was used. This tool uses linear regression to fit stellar photosphere or YSO model SEDs to observed fluxes, quantifying the goodness of fit by a χ^2 value.

The bandmerged sources were first fit against standard stellar photosphere models (Brott & Hauschildt, 2005) to eliminate foreground/background stars not associated with the RMC. The criterion for a source to be well fit by a stellar photosphere was that the χ^2 per data point for the best fit should be less than 3. This cutoff is arbitrary, but visual inspection of the fits shows that this cutoff is adequate for the purposes of this survey. Sources not well fit by stellar photosphere models (which will be referred to as *non-stellar*), are then likely to be either sources with real near and/or mid-IR excesses, or sources for which bad data is causing the stellar fits to have large χ^2 values.

Before fitting the non-stellar sources with YSO models, the IRAC and MIPS photometry was manually checked by inspecting the residual images, along with the SED, to determine if any over or under-estimated fluxes were present, and removed any such data points. The bad data points were typically a result of imperfect point source extraction either through incorrect deblending or a poor estimate of the flux using PRF fitting (often due to clumpy and bright diffuse emission). Sources for which data points were removed had their remaining data points refit against stellar model SEDs, filtering out any sources that could now be fit well.

Finally, the remaining non-stellar sources were fit using the grid of 200,000 model YSO SEDs (Robitaille et al., 2006). For each source, all models with a $\chi^2 - \chi^2_{\rm best}$ per data point of less than 2 were considered (in a similar way to Robitaille et al. 2007) to estimate ranges of parameters providing a good fit for each model. In order to classify the sources, values of the envelope accretion rate $\dot{M}$ were used to discriminate between sources which could be fit well only by models with $\dot{M} > 0$, and sources where the range of envelope accretion rates allows both zero and non-zero values of $\dot{M}$. The former are likely to be the youngest sources (Class I), as their SEDs cannot be explained by disk-only models, while the latter are more evolved sources (Class II), or sources for which the data does not constrain the evolutionary stage.

Of the 59005 IRAC sources, 15964 sources had the 4 data points passing the signal-to-noise ratio cuts and were not located within 3 pixels of a saturated source. Of those, 14969 (93.7%) were well fit by stellar photospheres. Checking the photometry by inspection of the remaining 995 non-stellar sources resulted in a further 146 sources being fit by stellar models and 89 sources being discarded due to only having 3 data points after removal of bad data. Finally, 751 of the non-stellar sources were well-fit by YSO models (χ^2 per data point < 3), and 9 sources were not well fit by stellar or YSO models. Of the latter, at least four have an SED which is compatible with that of a background galaxy. Of the 751 YSO candidates, 37 could not be fit by disk-only models. These are likely to be the youngest sources in the sample.

Figure 4.6 shows typical SEDs for a selection of YSO candidates at various evolutionary stages, showing all model fits with a $\chi^2 - \chi^2_{\rm best}$ per data point of less than 2. The spatial distribution of the YSO candidates and the subset of embedded YSOs is shown in Figure 4.7 overlaid on a velocity map derived from ^{13}CO spectral line emission by Heyer et al. (2006).

Figures 4.8 and 4.9 show colour-colour plots made using the 4 IRAC bands. Stellar sources, YSO candidates with an unconstrained evolutionary stage, and YSOs requiring envelopes to model their SEDs generally occupy the corresponding regions of the IRAC colour plane previously used to classify YSOs (Megeath et al., 2004; Allen et al., 2004). There are 3078 sources in the catalogue with flux values in all four IRAC bands, a requirement to use the classification scheme outlined in Megeath et al. (2004). Using this scheme, 551 IR excess sources are identified of which 70 are Class I sources, 23 are Class I/II sources and 458 are Class II sources. SED fitting only requires 4 data points in any band to classify a source and thus finds $\sim$35% more IR excess sources than using an IRAC colour-colour

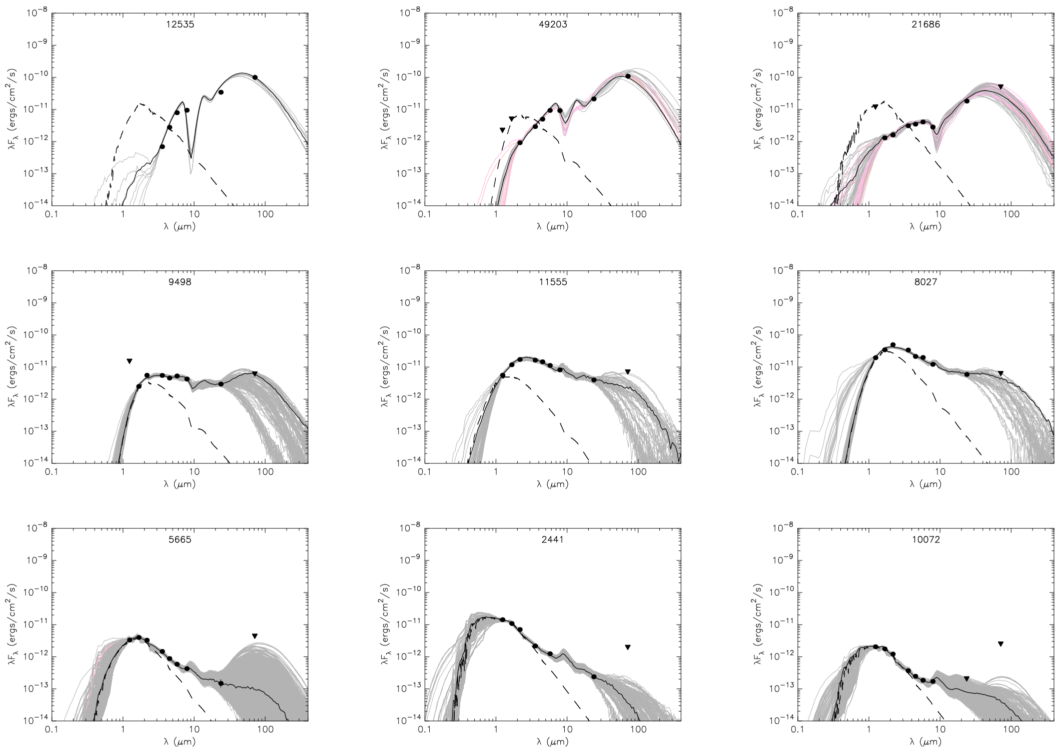

Figure 4.6: SEDs for nine of the 751 YSO candidates. The top three sources are three of the 37 sources whose SED cannot be fit by disk-only models, and are therefore likely to be young. The three middle sources are typical disk sources, and the bottom three sources are also disk sources, albeit at a more advanced stage of evolution. The black dots show the JHK, IRAC, and MIPS 24 μm fluxes, the triangles show upper limits, the solid line shows the best fitting SED model, and the grey lines show subsequent fits with $\chi^2 - \chi^2_{\rm best}$ per data point < 2.

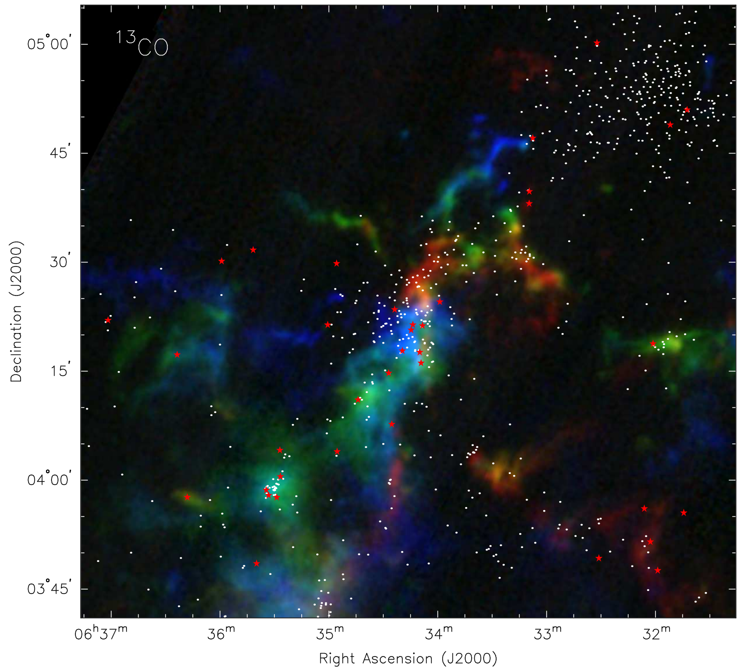

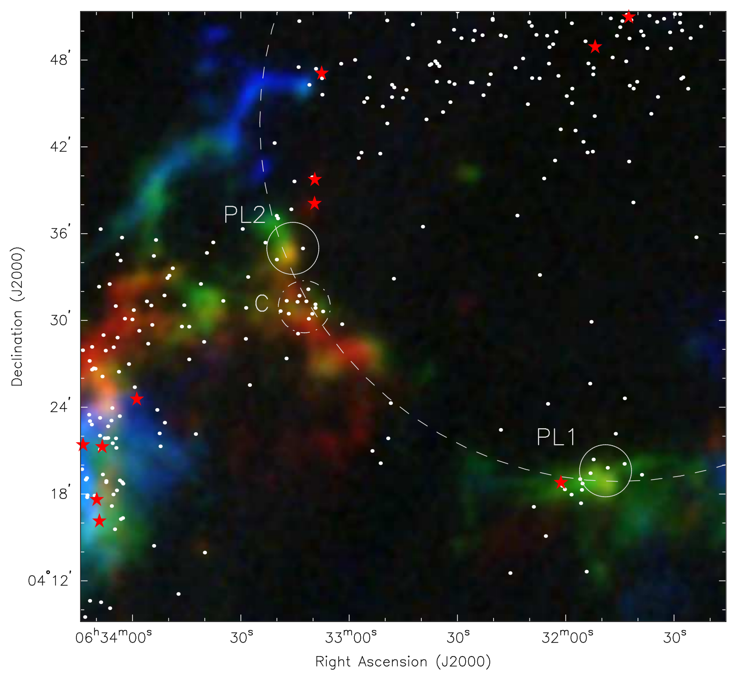

Figure 4.7: Spatial distribution of IR excess sources identified from SED fitting superimposed on a velocity map derived from ^{13}CO spectral line emission (Heyer et al., 2006). Filled red stars mark the position of IR excess sources whose SEDs cannot be fit by disk-only models, white dots indicate the positions of IR excess sources whose SEDs can be fit by disk-only models. Each colour corresponds to a range of velocities; Red: 14 to 21 km/s, Green 11 to 15 km/s, Blue: 8 to 12 km/s. The lower panel shows the detail near the nebula/cloud interface (shown as a dashed line) and the positions of clusters PL1-2 and a previously unknown cluster C, identified in this survey.

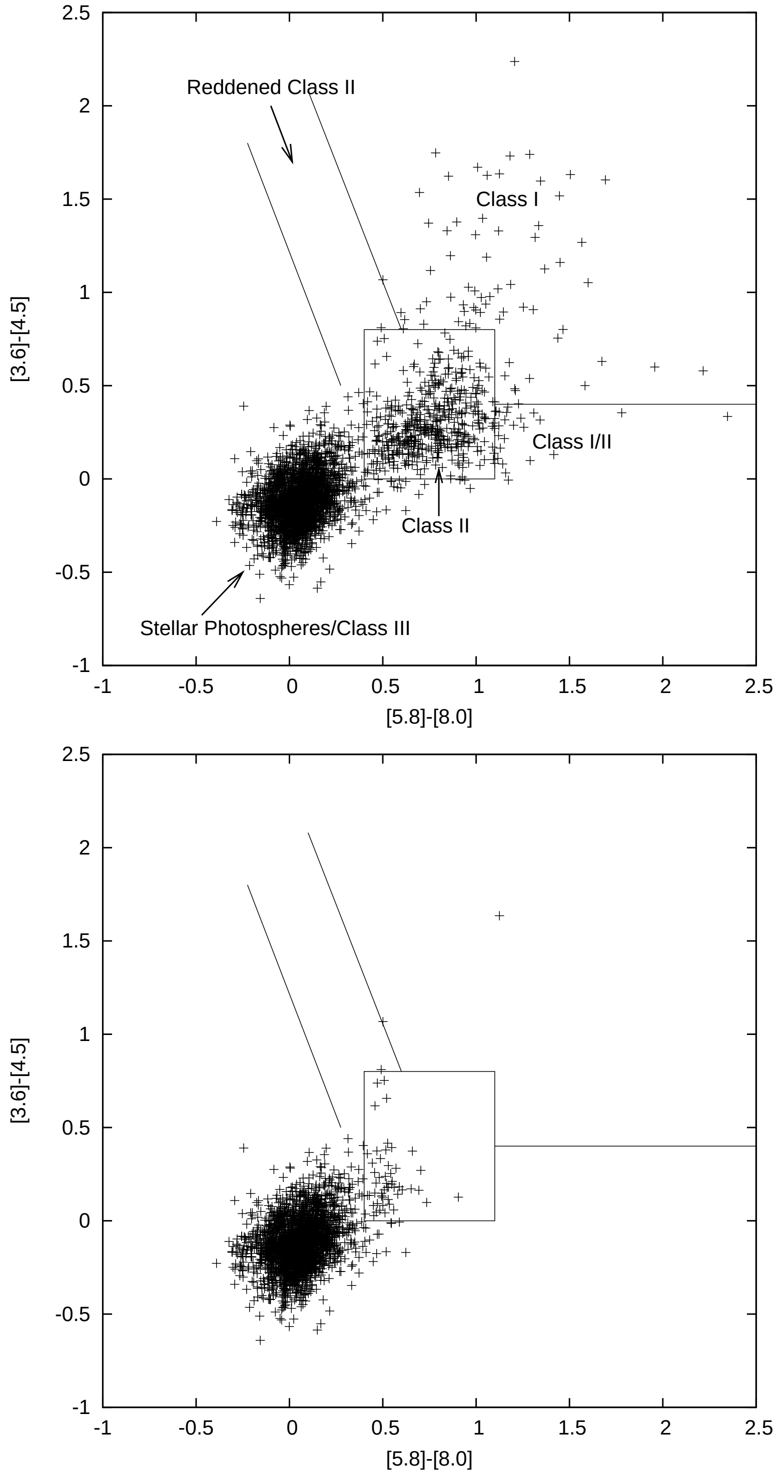

Figure 4.8: IRAC colour-colour plots for point sources using the four IRAC band fluxes. The lines outline the loci of the IRAC colour plane that are used to classify the sources, based on the selection criteria of Allen et al. (2004) and Megeath et al. (2004) as indicated by the labels in the upper panel. Upper panel: All point sources in the field identified in all 4 IRAC bands. Lower panel: Sources with SEDs fit with stellar photospheres.

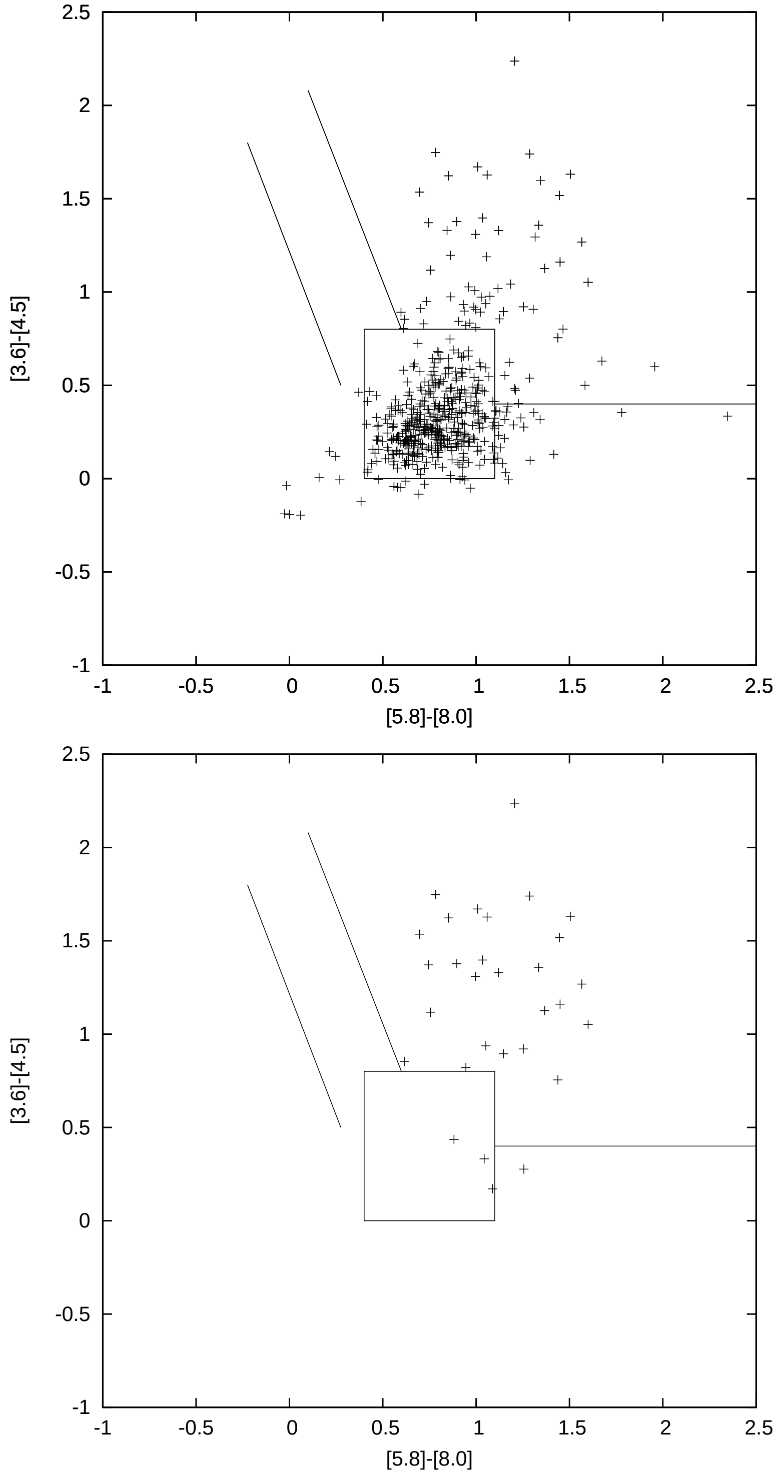

Figure 4.9: IRAC colour-colour plots for point sources using the four IRAC band fluxes. The lines outline the loci of the IRAC colour plane that are used to classify the sources, based on the selection criteria of Allen et al. (2004) and Megeath et al. (2004) as indicated by the labels in the upper panel of Figure 4.8. Upper panel: Sources with SEDs requiring at least a disc to model the infrared excess. Lower panel: Sources with SEDs requiring an envelope to model the infrared excess.

plot requiring 4 IRAC points. Some of the IR excess sources identified using IRAC colours are also known to be contaminated by extragalactic sources (e.g. Winston et al. (2007)). In general, the numbers of IR excess sources and of embedded YSOs found by the two techniques are consistent to within a factor of ~ 2.

4.5.2 Limitations of the Survey

There are several completeness issues affecting this survey. Firstly, requiring that at least 4 data points are used to fit a SED curve to the data means that detection of IR excess sources is limited by the IRAC band 4 mass limit of 0.4 $M_{\odot}$. Point source extraction is more difficult in IRAC bands 3 and 4 due to extended Polycyclic Aromatic Hydrocarbon (PAH) emission so the survey is more incomplete at these wavelengths.

Approximately 88% of binaries are too close to be resolved into separate point sources in IRAC band 1 (Duquennoy & Mayor, 1991), thus the total number of young stars is underestimated. Also, any Spitzer analysis is limited to YSOs with disks or envelopes, that is Class I and II sources that exhibit an IR excess. Haisch et al. (2001b) found that while the fraction of YSOs with disks in embedded clusters is initially very high (80%), it rapidly decreases with increasing cluster age, so that within 3 Myr one half of the stars within the clusters have lost their disks with an overall disk lifetime of 6 Myr in their cluster sample. Li & Smith (2005a) obtained an age estimate of ~1 Myr for clusters 1 and 2 by comparison with K_s luminosity functions of embedded clusters with known ages (Lada & Lada, 1995) and this suggests that the disk frequencies in the RMC should be high (>80%). Sources may exhibit other indicators of youth such as bright X-ray emission or variability (Allen et al., 2005) but this survey only detects those with an IR excess. Thus, $< 20\%$ of young stars could be missed due to being discless.

Finally, clusters PL1-5 are surrounded by bright extended emission in all IRAC and MIPS bands, most likely from hot dust. Overcrowding is also a problem when sources are too close to be resolved into individual point sources. This is the case for many of the sources in the Phelps & Lada (1997) clusters in the MIPS 24 μm band (see Figures 4.3 and 4.4). Cluster PL6 is dominated by and includes several pixels saturated by the bright binary AFGL 961. Therefore, in all but PL7 of the Phelps & Lada (1997) clusters the efficiency of the point source extraction is reduced for all IRAC and MIPS bands and the survey is more incomplete in these regions than the rest of the cloud.

To quantify the magnitude of all the effects described above requires identification of YSOs from star counts which has the merit of not discriminating against sources without an infrared excess (Allen et al., 2005). A cut of 0.4 mJy was applied to the IRAC band 1 fluxes to reduce the contamination from field stars since most of the YSOs found from SED fitting have IRAC band 1 fluxes above this value. Then subtracting the background density of stars estimated from parts of the field not coincident with the molecular cloud, the completeness of the survey was estimated within a radius of 1 pc around the Phelps & Lada (1997) clusters. The percentage of IR excess sources found from SED fitting compared to the number implied from the star counting method varies from 0% in PL2 (0 sources compared to 15 sources) to 83% in PL7 (24 compared to 29 sources). This demonstrates that the survey does not include most of the sources belonging to clusters PL1-6. A more accurate assessment of completeness around clusters PL1-6 requires an estimation of the position dependent contamination by field stars as briefly discussed in Chapter 6.

4.6 Spatial Distribution of Protostars

4.6.1 Local Stellar Densities

This study of star formation in the RMC also seeks to answer the question of whether stars form dominantly in a clustered environment or in isolation in the RMC. Therefore a clear definition of which stars are considered to be in a clustered environment and which are not is required.

The local surface density for each IR excess source was calculated using the method outlined by Megeath et al. (2005). Local stellar surface density, σ, is given by:-

$$\sigma = \frac{5}{\pi R^2} \tag{4.1}$$

where R is the separation to the 5th nearest IR excess source and is calculated assuming a distance of 1.6 kpc to the RMC.

A cumulative frequency plot of the local stellar densities computed at the position of each of the IR excess sources found in this survey and for a random distribution is shown

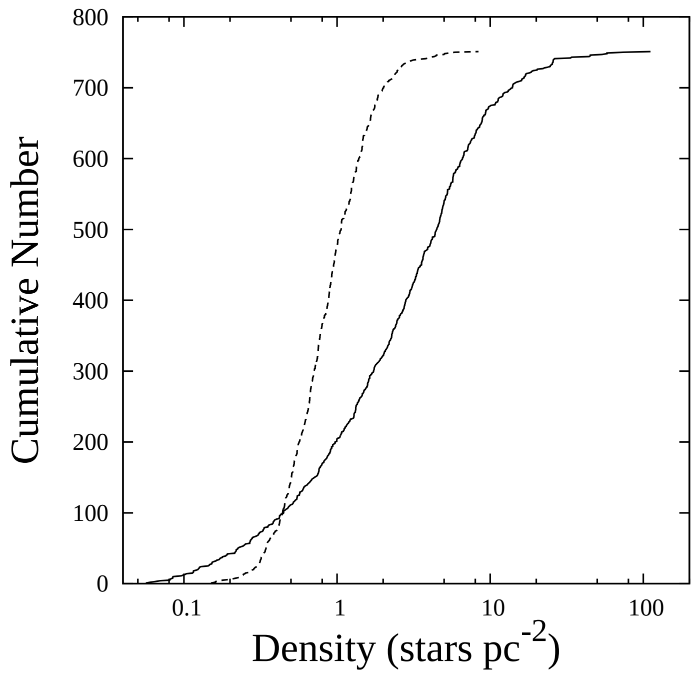

Figure 4.10: Solid line: Cumulative frequency plot of the local stellar densites computed at the position of each IR excess source. Dashed line: Cumulative frequency plot of the local stellar densities computed for the same number of sources randomly and uniformly distributed in the same area of sky.

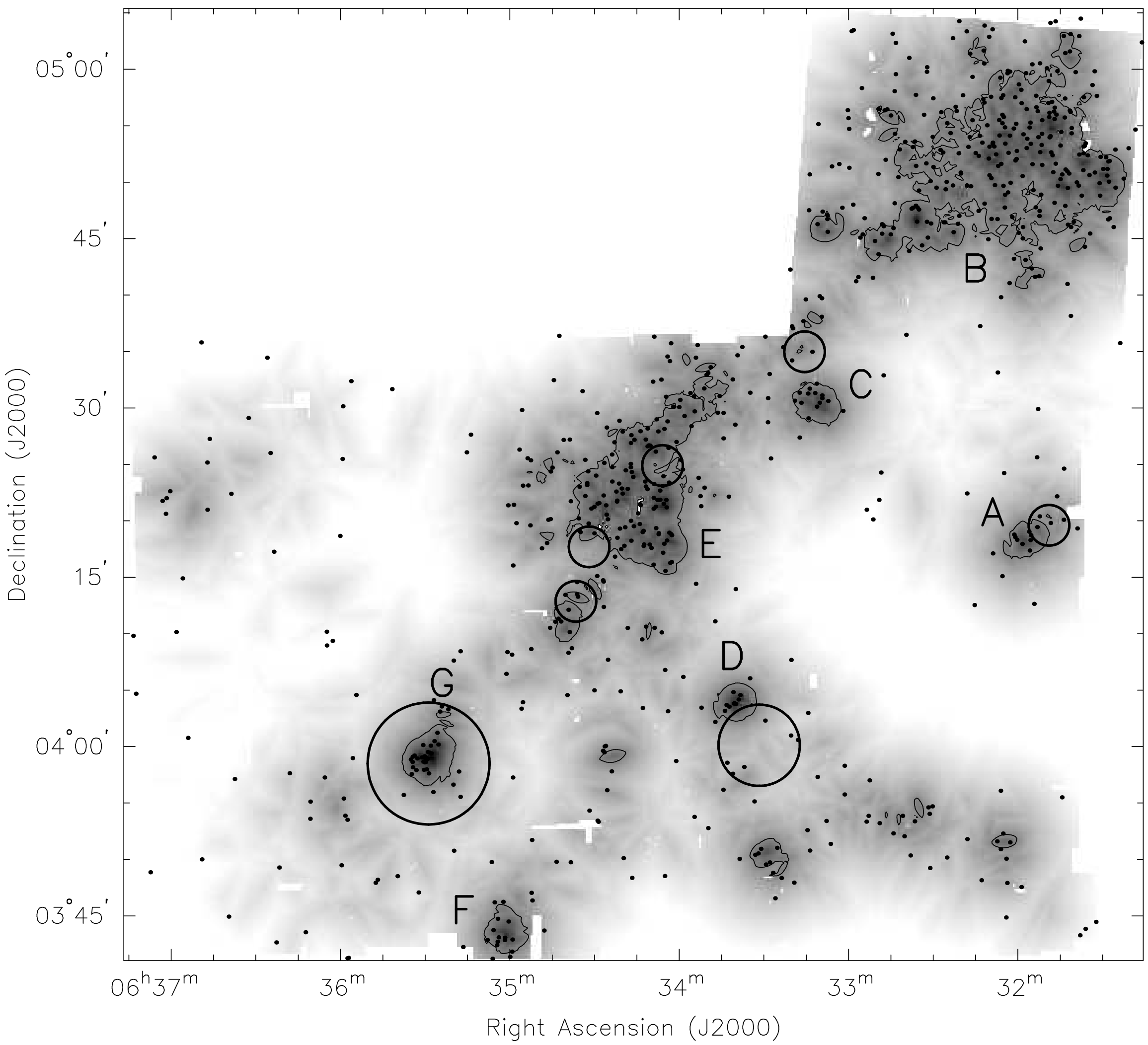

Figure 4.11: Contours overlaid on IRAC band 1 field indicating local stellar densities for the 751 IR excess sources found using SED fitting. The black line highlights the 2.5 stars pc^{-2} contour. Small dots show the position of the IR excess sources, unfilled circles show the position of the seven clusters identified by Phelps & Lada (1997) and letters A-G mark the position of clusters identified in this survey. The size of the circles indicates the area of the image covered in the detailed images of the clusters in Figures 4.3 and 4.4.

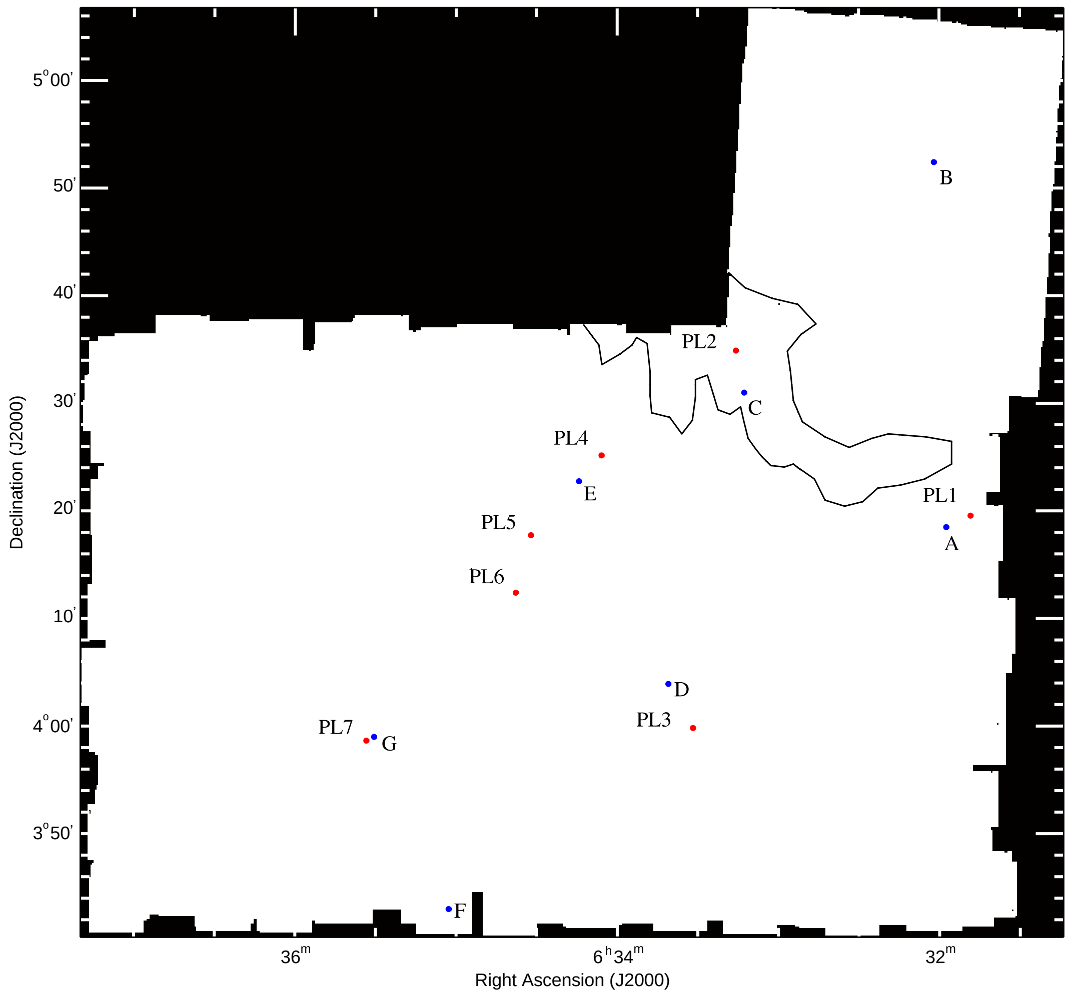

Figure 4.12: Schematic showing the positions of clusters A-G identified in this survey (blue circles) relative to clusters PL1-7 identified by Phelps & Lada (1997) (red circles) and the ionisation front identified from H Brackett α emission (black outline).

in Figure 4.10. The random distribution displays a small spread in local stellar surface densities, as indicated by the dashed line. However, the solid line shows that a significant fraction of the IR excess sources exhibit higher local stellar surface densities indicating the presence of clusters of young stars in the sample.

A similar procedure was followed to make a map of stellar surface density shown in Figure 4.11 by finding the 5th nearest neighbour to each pixel centre using Equation 4.1. The local stellar densities of IR excess sources computed for the Rosette are in general a factor of 10 smaller than those found in more nearby star forming regions such as the Orion Molecular Clouds at a distance of 450 pc. Megeath et al. (2005) define a cluster as 10 or more IR excess sources within a region of the cloud with local stellar surface densities of greater than 10 stars pc^{-2}. Due to the incompleteness issues discussed in Section 4.2, it is necessary to relax the requirements of Megeath et al. (2005) to define a cluster in this survey.

For a sample of points distributed randomly across the same area, 99% of the pixels have a value less than approximately 2.5 stars pc^{-2}. This contour is drawn on Figure 4.11 and clusters are defined as 7 or more IR excess sources bound by this contour since clusters of this size do not occur in the random sample of points. Approximately 50% of the IR excess sources are in regions where the local stellar density is in excess of 2.5 stars pc^{-2} and thus exhibit some level of clustering compared to the sample of random points distributed uniformly over the same area.

The properties of the clusters identified are summarised in Table 4.1 and Figure 4.15 shows the detail of the new clusters found in this survey. The positions of the clusters identified in this survey relative to clusters PL1-7 identified by Phelps & Lada (1997) and the ionisation front identified from H Brackett α emission are shown in Figure 4.12. Clusters PL2, PL3, PL5 and PL6 are not recovered using this definition of clustering and only one side of cluster PL1 is recovered. This is due to the incompleteness issues in these areas as discussed in section 4.2 but for PL2, PL3 and PL5, clusters of IR excess sources are found nearby (within 2 pc). Clusters C and D are located close to the same ^{13}CO clumps as PL2 and PL3 respectively but the brightest MIPS sources in cluster E and cluster F are aligned with ^{13}CO clumps previously not thought to be associated with a young cluster (Williams et al., 1995; Phelps & Lada, 1997). The high stellar surface density in cluster G (Table 4.1) suggests that it may be a more tightly bound cluster with

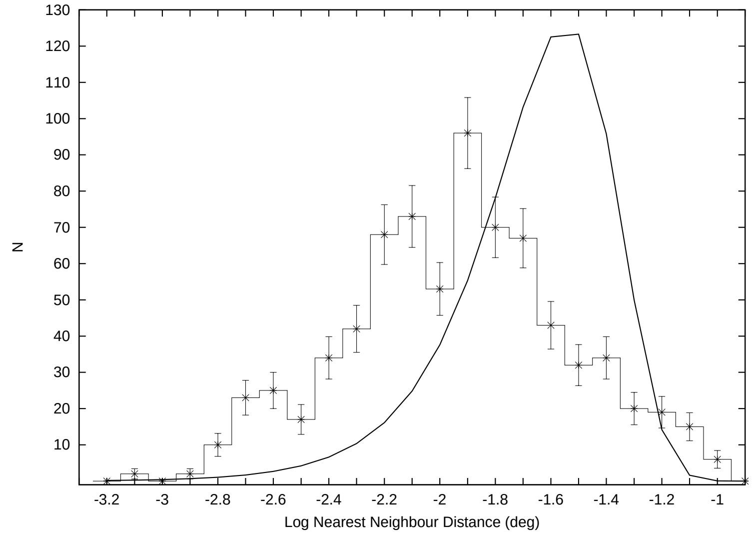

Figure 4.13: Number distribution of the projected separation distance between nearest neighbours for the 751 IR excess sources found in the field. The solid line is the expected distribution for a random (Poisson) distribution for the same number of objects over an identical area. Error bars are calculated from square root number statistics.

more stars found in a smaller area. However, the higher density could also result from its position in a region with lower extended emission from PAHs and hot dust resulting in the survey being more complete here than in the rest of the cloud.

4.6.2 Nearest Neighbour Distribution

The nearest neighbour distribution is defined as the frequency distribution of angular separations of each IR excess source to its nearest neighbour. This distribution emphasises any fragmentation scale or scale associated with gravitational confinement (Li & Smith, 2005c). The log of the separation from each IR excess source to its nearest neighbour was computed and then binned to construct the histogram in Figure 4.13. Pairs of IR excess sources with separations closer than $\sim 1.8''$ (equivalent to a spatial separation of $\sim$3000 AU) were counted as one object to eliminate the majority of binary stars. The distribution expected for a random sample of points uniformly scattered in the same area was determined using Poisson statistics (Gomez et al., 1993). The distribution shows an excess of neighbouring stars with separations between $7''$ and $25''$ above that expected for a uniform distribution of point sources.

Assuming the nearest neighbour pairs have a random distribution of orientations

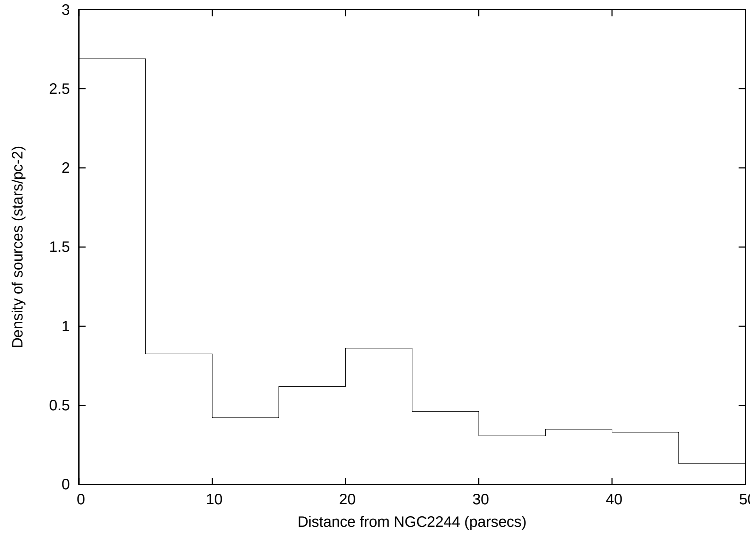

Figure 4.14: Histogram of IR excess source surface densities within annuli centred on NGC 2244 using radii in 5 pc bins. There is an over density of IR excess sources at distances of 15-25 pc from NGC 2244, approximately 5-10 pc ahead of the ionisation front and the nebula/cloud interface.

then the true separation is larger than the projected separation by a factor $4/\pi$ (Gomez et al., 1993). The median nearest neighbour separation is $\sim 40''$, which after applying the above correction and assuming a distance of 1.6 kpc to the Rosette corresponds to a separation of 0.38 pc. This is comparable to but near the upper extent of the median separations observed in other star forming regions (Gomez et al., 1993), although this value is an upper limit due to the incompleteness in the survey discussed in Section 4.2.

The sonic scale sets the spatial regime at which turbulence can no longer generate density fluctuations by shocks and should be reflected in the spatial separation between protostellar cores and the resultant YSOs. The value of the median separation of nearest neighbour pairs is close to the sonic scale of 0.33 pc derived by Heyer et al. (2006), assuming a kinetic temperature of 10 K. This value of the sonic scale is also an upper limit since it is derived for the entire cloud which may be more representative of the initial conditions than the field of view where the ionisation front and UV heating have modified the state of the gas.

Table 4.1: Properties of the clusters of IR excess sources found using local stellar densities. The numbers in brackets indicate the number of Class I sources in each cluster. The cluster locations are shown in Figure 4.11 and images of each of the new clusters are shown in Figure 4.15.

Cluster ID	R.A. h:m:s	dec °:′:″	Number of IR Sources (Class I)	Area (pc^2)	Density (stars pc^{-2})	Distance from PL cluster (pc)	Notes
A	6:31:57.466	4:18:29.92	9 (1)	2.12	4.25	0.50	Part of PL1
B	6:32:01.985	4:52:25.25	176 (2)	43.34	4.06	-	Region around NGC 2244
C	6:33:12.684	4:31:00.52	12 (0)	2.60	4.62	1.82	New cluster, Near PL2
D	6:33:40.980	4:03:56.12	9 (0)	2.16	4.16	1.91	New cluster, Near PL3
E	6:34:14.237	4:22:46.42	107 (7)	23.99	4.46	-	Includes new cluster and PL4
F	6:35:02.791	3:43:00.62	12 (0)	3.93	3.06	-	New cluster
G	6:35:30.550	3:59:00.60	27 (4)	2.49	10.84	0.16	Identified as PL7

4.6.3 Two Point Correlation Function

The clustering properties of a set of points can be described using a two point correlation function. Gomez et al. (1993) was the first to apply this technique to investigate the clustering properties of YSOs in Taurus. Li & Smith (2005c) also followed a similar procedure for 2MASS point sources in the Rosette Molecular Cloud, noting significant clustering for sources with a H - $K_S > 0.7$ colour constraint.

The two point correlation function is a measure of the excess number of pairs in the observed distribution over a random distribution of the same number of point sources over the same area. The log of the angular separations, θ are binned between log θ and log θ + d log θ in intervals of 0.2, to find the number of pairs in each bin $H_d(\theta)$. The same procedure is followed for a random sample of points distributed over the same area, with the number of coordinate pairs denoted by $H_r(\theta)$. The two point correlation function, $\Phi(\theta)$ is then defined as

$$\Phi(\theta) = \frac{H_d(\theta)}{H_r(\theta)} - 1. \tag{4.2}$$

The signature of excess of pairs at any given separation is when $\Phi(\theta) > 0$. For an unclustered set of sources, the function $H_d(\theta)$ will be similar to the random distribution $H_r(\theta)$ and the two point correlation function will be close to a straight line at $\Phi(\theta) = 0$.

Clustering is observed as an overdensity of small separations as shown in Figure 4.16. The two point correlation function is positive for values of log θ below -0.5.

The two point correlation function can be fit with a power law $\Phi(\theta) \propto \theta^{\alpha}$ with α = -2.3 for values of log θ < -0.7, which is larger than the value of -1.2 calculated for Taurus-Auriga (Gomez et al., 1993).

4.7 Evidence for Triggering

Triggering processes are often thought to be dominant in sustaining and dispersing on-going star formation (Elmegreen, 1998; Lada, 1987). Elmegreen & Lada (1977) proposed that star formation is triggered sequentially in molecular clouds through pressures from HII regions.

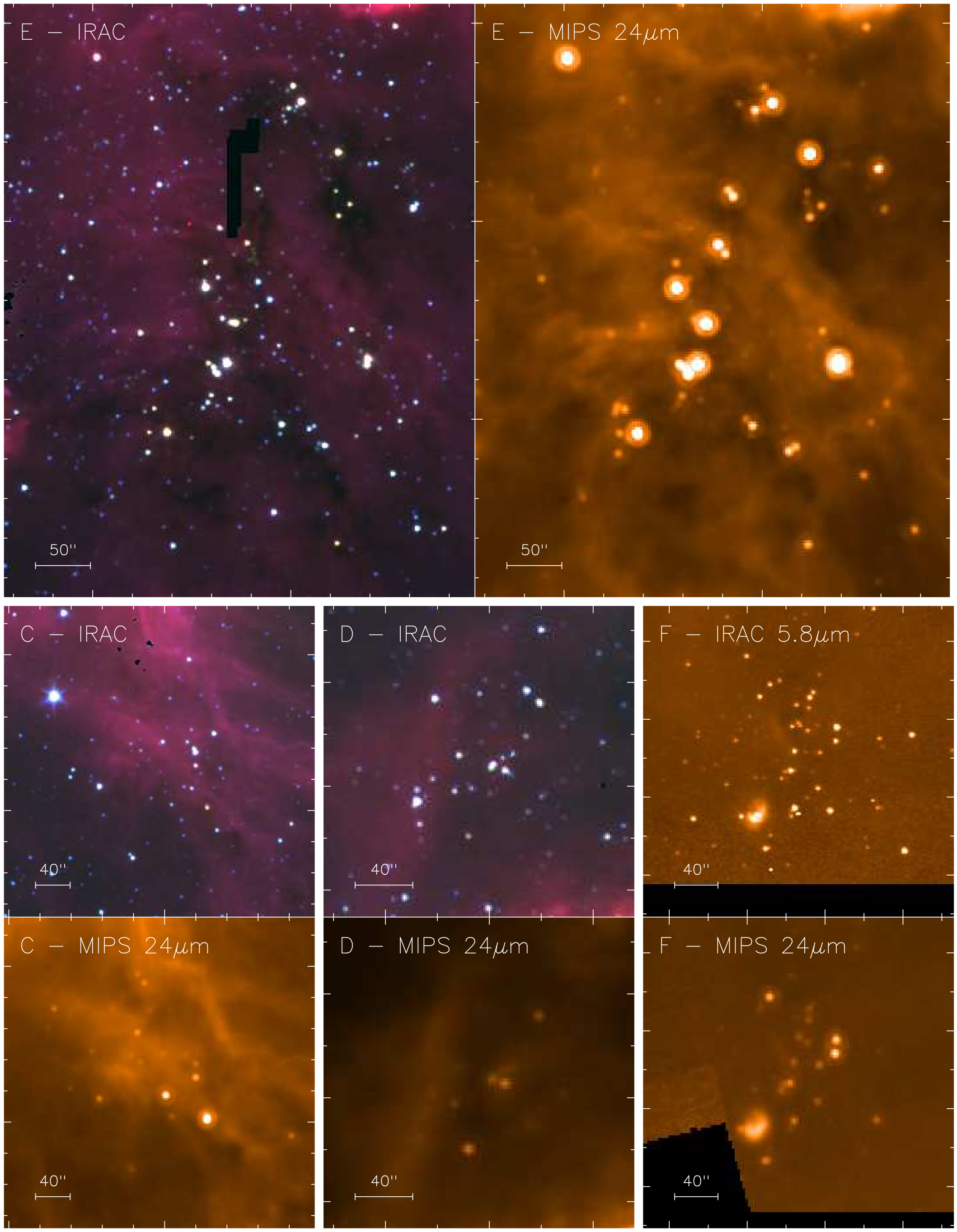

Figure 4.15: Detailed images of the new clusters of IR excess sources identified in this survey and with their positions identified in Figure 4.11. The IRAC data is depicted in false colour images for clusters C, D and E. Blue: IRAC band 1 (3.6 μm), Green: IRAC band 2 (4.5 μm) and Red: IRAC band 3 (5.8 μm).The IRAC image for cluster F is shown only in IRAC band 3, due to its location outside of the IRAC band 2 and 4 field of view.

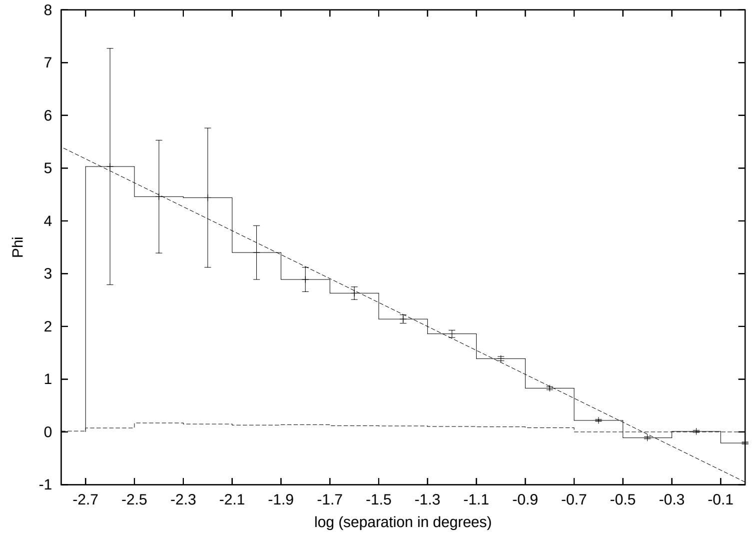

Figure 4.16: The two point correlation function for the YSOs (bars outlined with solid line) and standard stellar sources (bars outlined with dashed line). The error bars correspond to $\sqrt{N}$ statistics. The dashed line indicates the line of best fit for the YSOs values calculated for log(separation) $<$ -0.7.

The Rosette Molecular Cloud has been cited as an example of intermediate scale triggering by the expansion of the HII region moving the neutral cloud, accumulating the material into a dense neutral ridge at the nebula/cloud interface (Elmegreen, 1998). This is based on the suggestion of Phelps & Lada (1997) that the spatial location of the clusters close to the ionisation front associated with NGC 2244 implies that their formation may have been induced. A signature of this process would be to observe the IR excess sources (particularly those YSOs requiring an envelope to model their SEDs) both along the ionisation front and within the HII region (Dale et al., 2007a). An age gradient may also exist such that the formation of sources along the ionisation front has been induced recently and therefore younger sources will be observed here than closer toward NGC 2244.

An external trigger may be responsible for initiating the collapse of the cloud outside of the ionisation front and the formation of the dense clumps and filaments observed there in ^{13}CO. Triggering on a more local scale, such as winds or outflows from one cluster to an adjacent cluster is also possible although only one jet was detected. Here only triggering associated with the expansion of the HII region associated with NGC 2244 is considered.

The ionisation front is an expanding shell driven by the OB stars in NGC 2244. Balog et al. (2007) note that sources that are located at the nebula/cloud interface but behind the cavity would actually be projected so that they appear within the cavity so the enhancement of star formation could appear blurred. In the normalised IRAC band 2 minus IRAC band 4 difference image (Fig. 4.5), the H Brackett α transition tracing the ionisation front is indicated by regions of bright emission. Plotting mean emission within annuli centred on NGC 2244 shows an excess of emission between 10-15 pc.

Figure 4.14 shows the IR excess surface densities calculated for sources enclosed within annuli with radii bin widths of 5 pc, centred on NGC 2244. The over density of IR excess sources observed within 10 pc of NGC 2244 (cluster B) contain a lower proportion (approximately 2%) of Class I sources than both other star forming regions (Chen et al., 1995) and the rest of the Rosette Molecular Cloud (approximately 7%, see Table 4.1) consistent with the findings of Balog et al. (2007). This suggests star formation is nearing completion in the cavity itself.

An over-density of IR excess sources is not observed 10-15 pc from NGC 2244, at the approximate location of the ionisation front and the nebula/cloud interface where cluster formation triggered by the expanding HII region would be expected to be concentrated. Clusters A, C, PL1 and PL2 are located here, coincident with a ring of clumps visible in ^{13}CO (Fig. 4.7) and this cluster formation is consistent with triggering by compression of the molecular cloud by the expanding HII region. Only 3 of the IR excess sources in these clusters belong to the group of young sources whose SEDs cannot be fit by disk only models. However, the dense cores of clusters PL1 and PL2 may contain very young sources not detected in this survey and the possible detection of a parsec scale outflow found in SII emission near cluster A (Phelps & Ybarra, 2005) suggests active star formation may still be occurring here.

An over-density of IR excess sources is apparent in the 15-25 pc bins in Figure 4.14, corresponding to the large agglomeration of stars in clusters E and PL4, coincident with the brightest clumps in ^{13}CO emission. Comparison of the number of IR excess sources lying within radii of 15-25 pc of NGC 2244 with the background number of IR excess sources within radii of 10-45 pc shows that the density of IR excess sources within radii of 15-25 pc is higher by approximately 60%. This part of the cloud also contains 8 of the youngest sources shown in Figure 4.7 suggesting that this region is the hotbed of active star formation in the RMC. This is 5-10 pc ahead of the brightest H Brackett α emission and the edge of the cavity cleared around NGC 2244. The dense ridge seen in ^{13}CO emission in Figure 4.7 is aligned parallel to the direction in which the ionisation front is expanding. In contrast, if the expanding HII region was responsible for accumulating the cloud into a dense ridge, that ridge would run along the ionisation front with active cluster formation taking place at the edge of the HII region and/or within the cavity, allowing for projection.

Phelps & Lada (1997) proposed that clusters PL3-6 maybe also be triggered by the compression of the high density clumps by UV photons penetrating deeper into the cloud due to inhomogeneities present in the RMC (Blitz & Stark, 1986; Block, 1990). However, Phelps & Lada (1997) also note that clusters PL2, PL4, PL5, PL6 and PL7 are located along the midplane of the cloud and may have formed by fragmentation of the cloud. Many of the youngest sources and clusters C and F are also located close to the midplane of the cloud identified by Williams et al. (1995). Therefore, it is plausible that an external trigger is responsible for the collapse of the cloud into a dense ridge and the ensuing star formation within it and that compression of the material by the ionisation front associated with NGC 2244 plays a minimal role in the onset of star formation.

Clusters D, F and G have formed well beyond the influence of NGC 2244 which demonstrates that not all of the star formation in the RMC is triggered by the ionisation front. In particular, cluster G contains 4 of the IR excess sources which require an envelope model to fit their SEDs implying that star formation is still active here. If star formation is still ongoing here, it supports the argument that the formation of clusters E and PL3-6 was also not instigated by the NGC 2244 ionisation front.

4.8 Summary

A survey of the Rosette Molecular Cloud star forming region is presented. Fitting model SEDs to observed fluxes, 751 YSOs with IR excesses are identified in the field. Sources were identified as protostellar objects with infalling envelopes (Stage I) if their fluxes could not be fit by SEDs from disk-only models.

Local stellar surface density calculations and nearest neighbour distributions of the IR excess sources show that they are clustered when compared against the same number of random points uniformly distributed over the same area. Requiring a cluster to consist of at least 7 members in a region with a local stellar density of at least 2.5 stars pc^{-2}, 7 clusters of various sizes are identified in the field containing approximately 50% of all the IR excess sources. This survey is incomplete around 6 of the clusters identified by Phelps & Lada (1997) which are surrounded by bright extended emission. The Stage I objects are scattered among the clusters, not associated with any one part of the field.

Two distinct populations of YSOs with IR excesses are observed, those in the nebula i.e. within approximately 15 pc of NGC 2244 and in the cavity cleared by the expanding HII region, and those beyond the ionisation front, residing in the molecular cloud. The former population is markedly older with only 2% of sources being identified as Class I sources compared to a proportion of 7% in the latter population. Within 15 pc of NGC 2244, star formation is thus nearly complete, in contrast to parts of the clouds at larger distances.

It is likely that CO clumps aligned along the Brackett α emission have been compressed by the expanding ionisation front associated with NGC 2244, instigating cluster formation. The dense ridge of material observed in ^{13}CO, 10-15 pc ahead of the nebula/cloud boundary is confirmed as the hotbed of star formation in the RMC; and is oriented perpendicular to the direction expected if accumulation of the cloud and triggering via the "collect and collapse" model is important.

The presence of clusters containing YSOs with IR excesses more than 20 pc from the nebula/cloud interface show that star formation is occurring in the RMC beyond the influence of NGC 2244 and its expanding HII region. Thus, the collapse of the cloud, formation of the dense ridge and the resulting hotbed of star formation can be plausibly explained by the action of an external trigger without the need for accumulation of the cloud by the NGC 2244 ionisation front.

CHAPTER 5

A Survey of IR Excess Sources in the W4 Loop

5.1 Abstract

Mid-infrared data for W4 and SCUBA data for the star forming region AFGL 333 are presented. Young stellar objects with infrared excesses were identified by calculation of spectral indices using 2MASS 2 μm and MIPS 24 μm data. Whilst some clusters of young sources are coincident with the loop of emission to the south of the cluster OCl 352, consistent with a scenario of triggered star formation in a swept-up shell, several young sources are found to be forming outside of this ring. The dust temperature and mass of AFGL 333 are estimated and the result implies a star formation efficiency of $\sim$4% in the W4 loop. The contribution to the Galactic star formation rate from similar sized shells in the galaxy is estimated to be $\approx$2.5%.

5.2 Introduction

The W4 HII region is part of a larger complex located in the Perseus arm of our Galaxy that also includes the HII regions W3 & W5 and the supernova remnant HB 3 as shown in Figure 5.1. At the heart of the W4 region is the open cluster OCl 352, containing 145 stars (Strobel, 1992), 8 of which are O-type stars (Massey et al., 1995). The region above OCl 352 is a cone-shaped void observed in neutral hydrogen by Normandeau et al. (1996) which is generally referred to as the W4 superbubble (Oey et al., 2005). Below OCl 352, toward the galactic plane is a cavity outlined in intense Hα emission (Dennison et al., 1997) which is coincident with the ring of emission observed in this chapter and will be referred to as the W4 loop.

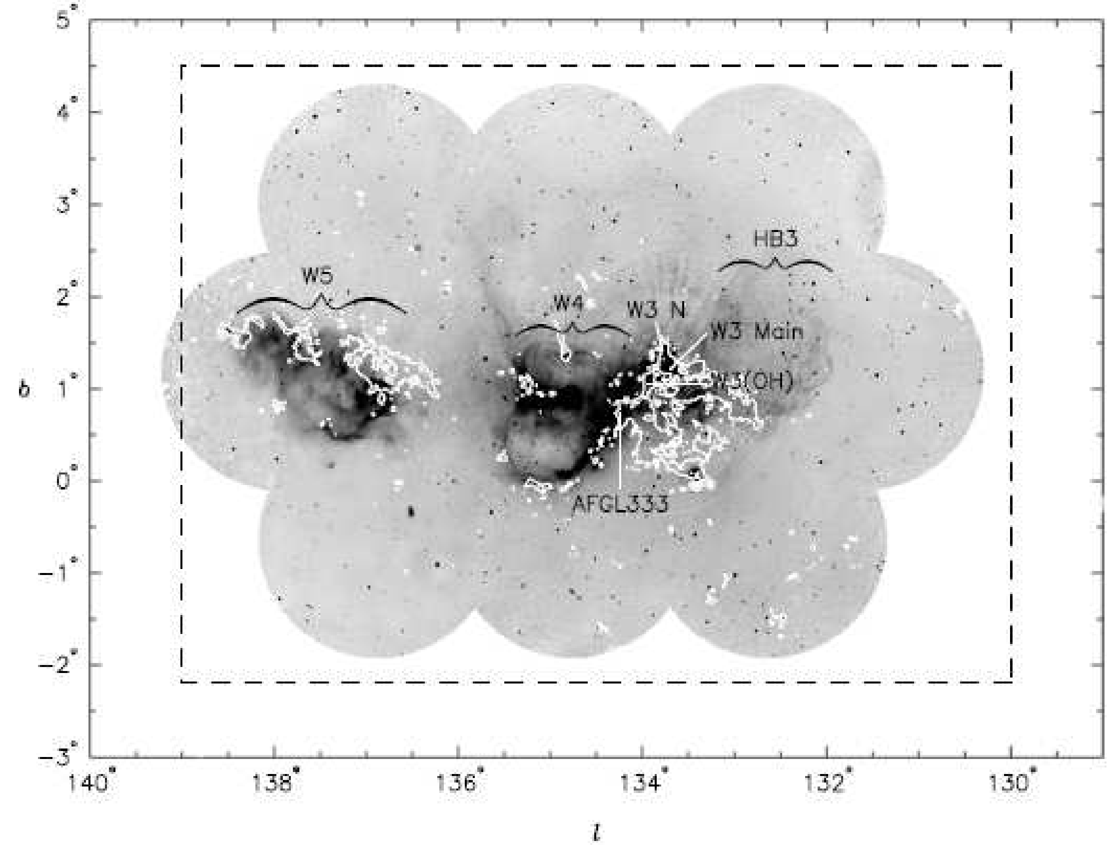

Figure 5.1: A 21 cm image of the region encompassing the W3, W4 & W5 HII regions from the DRAO Galactic Plane Survey (Normandeau et al., 1997) with contours of the ^{12}CO (1-0) integrated intesity overlaid from Carpenter et al. (2000)

It has been suggested that supernovae or winds from massive stars in clusters in the Galactic plane can produce expanding superbubbles in the interstellar medium (ISM) that can burst out of the Galactic disk to produce outflows into the Galactic halo (Tenorio-Tagle & Bodenheimer, 1988; Norman & Ikeuchi, 1989) known as Galactic "chimneys". The region void of HI above OCl 352 has been considered a candidate for a such an object and as such is also sometimes referred to as the W4 "chimney" (Reynolds et al., 2001; West et al., 2007). Recent observations of this region by West et al. (2007) show that it is in fact a superbubble 164 pc wide and extending 246 pc above the Galactic midplane with a closed top that is likely in the process of fragmenting and evolving into a "chimney". Reynolds et al. (2001) also discovered a loop of HII reaching 1300 pc from the Galactic midplane extending far above the W4 "chimney" and appears to be associated with the W3/W4/W5 HII region complex.

The age estimates of OCl 352 range from 1.3-2.5 Myr (Dennison et al., 1997) to 3.7-4.3 Myr (Normandeau et al., 1996). Normandeau et al. (1996) proposed that the stellar winds from the O stars in OCl 352 are responsible for clearing the region above the cluster of neutral hydrogen. The age of the superbubble is estimated to be $\sim$2.5 Myr by Basu et al. (1999) who argue this is consistent with the idea that the superbubble is blown by stellar winds from a cluster which is too young for supernovae to have occurred.

The W4 loop located below OCl 352 is visible in infrared, radio continuum and Hα emission (Terebey et al., 2003). Dennison et al. (1997) argue that the lower ring of bright Hα emission, coincident with the edge of an arc in CO emission found by Digel et al. (1996), represents gas heated and photoionised by the UV radiation from OCl 352. Terebey et al. (2003) consider the W4 loop as the lower part of the W4 superbubble structure with its smaller size presumed to be due to stalled expansion into more dense material. This is in agreement with Basu et al. (1999) who modelled the W4 superbubble and loop as a wind blown bubble expanding in a vertically stratified medium with a steep density gradient. West et al. (2007) argue that the W4 loop is a distinct component from the superbubble since the region above OCl 352 is cleared of HI whilst the lower region is not, but still consider it likely that the W4 loop is driven by winds from OCl 352. (Normandeau et al., 1996) argue that the ionised gas to the south of W4 is either formed from ionising radiation from the present generation of stars or may also be an old, background, low density HII region formed from a previous generation of stars. In this chapter, the possibility that the W4 loop may have in fact been formed from the expansion of a supernova remnant and not driven by winds from OCl 352 is not discounted. This is based on the morphology of the clouds; the main ring of emission is roughly circular centred near R.A. = $02^h32^m53.216^s$, decl. = $+60°58'38.45''$ with OCl 352 located on the northern rim of the ring.

Elmegreen (1998) states that expanding shells or rings can become gravitationally unstable and form clumps in the swept up material which then form clouds, some of which may evolve further to produce embedded clusters. Mueller & Arnett (1976) suggested that star formation can propagate on larger scales, not restricted to the original cloud. OB associations are thought to generate giant expanding shells that can accumulate sufficient material, leading to the occurrence of gravitational instabilities and subsequently the formation of new molecular clouds out of which new stars can form (Tenorio-Tagle & Bodenheimer, 1988). The mechanism of collapse is similar to that of the collect and collapse scenario described in Chapter 4 in which an expanding HII region can move material into a dense ridge. Tenorio-Tagle & Bodenheimer (1988) argue that the evolution of a multisupernova remnant can also sweep up and compress large quantities of material to high densities.

It has generally been accepted that the expanding W4 HII region has induced star formation in the eastern part of the W3 region of the complex, specifically the star forming regions named W3 Main, W3(OH), W3 N and AFGL 333 (Lada et al., 1978; Thronson et al., 1980). It is also possible that this star formation was already taking place before the HII region expanded into the W3 region and the dense material has just slowed the expansion of the HII region. Thronson et al. (1980) argued that if the star formation was not triggered then it should be spread evenly throughout the W3 region. The fact that the star formation is taking place preferentially in the Eastern part of the cloud suggests that it is in fact induced by the expansion of the W4 HII region (Thronson et al., 1980; Carpenter et al., 2000).

Oey et al. (2005) also point out that two superbubbles expanding into each other demonstrate sequential star formation but not strong evidence for triggered star formation. Oey et al. (2005) estimate that the OB association IC 1795 at the centre of the W3 region has an age intermediate between that of W4 and the young star forming regions W3 Main, W3(OH), W3 N. Therefore, they argue a three stage process in which W4 triggered the formation of IC 1795 which subsequently triggered the formation of the younger regions located around the W3 HII region.

AFGL 333 is a cloud filament located in the north-west rim of the W4 loop. Sakai et al. (2006) suggest that AFGL 333 is chemically younger than W3(OH) and suggest that while star formation has started taking place, the southern most cloud contains a few dense cores that are good candidates for starless cores where high or intermediate mass star formation might take place in the future.

In this chapter, a 24 μm map of the W4 HII region is presented and 850 μm data for AFGL 333. The main objective of this chapter is to survey the W4 loop and identify YSO candidates in the field using estimates for the spectral indices. The temperature of the dust in the star forming region AFGL 333 is also calculated to produce an estimate for the mass of the clouds and star formation efficiency in the W4 loop.

5.3 Observations and Data Reduction

5.3.1 MIPS

The W4 loop was surveyed with the Multiband Imaging Photometer for Spitzer (MIPS) at a wavelength of 24 μm. The region mapped was approximately 2.1° by 1.9° and included partial coverage of the AFGL 333 cloud.

The exposure time was 30s for each 5.2' x 5.2' MIPS 24 μm frame. Point source extraction included sources down to 1 mJy and the telescope point spread function (PSF) full width at half maximum is $6''$ at 24 μm.

5.3.2 SCUBA

The Submillimetre Common-User Bolometer Array (SCUBA) (Holland et al., 1999) at the James Clerk Maxwell Telescope on Mauna Kea, Hawaii was used to observe an area of $15'$ by $12.5'$ around AFGL 333 in August 2001 using the SCUBA "scan map" observing mode using $30''$, $44''$ and $68''$ chop throws in RA and Dec (Jenness et al., 1998). A fully sampled map comprising of 12 images was generated at $7.5''$ sampling, with a total integration time of $\sim$1 hour. The diffraction-limited FWHM beam size at 850 μm was $\sim 15''$, but the data have been smoothed using a $7''$ Gaussian to give an effective beam of $17''$. The data were reduced using the SCUBA User Reduction Facility (Jenness & Lightfoot, 1998) and are rebinned in a right ascension−declination frame with 2″ cells. Calibration maps were made to an accuracy within 10% using secondary calibrators CRL 618 & CRL 2688, giving flux conversion factors of 2 Jy V^{-1} $arcsec^{-2}$. Zenith atmospheric opacities were ∼0.1 at 230 GHz (1.3 mm), equivalent to ∼0.4 at 850 μm.

Pointing accuracy was ∼5″ at high elevation, which is small compared with the resolution obtained with 7.5″ sampling and a beam size of 15″ at 850 μm (FWHM). Each bolometer and map was weighted according to its noise levels.

5.3.3 Archived Data (2MASS & IRIS)

Data at wavelengths of 12 μm, 25 μm, 60 μm and 100 μm from the Improved Reprocessing of the IRAS Survey (IRIS) covering the same region was retrieved from the NASA/IPAC Infrared Science Archive. Archived photometry for the region surveyed was also retrieved from the Two Micron All Sky Survey (2MASS) at wavelengths in the J (1.24 μm) , H (1.66 μm) and K_s (2.16 μm) bands.

5.4 Point Source Extraction and Bandmerging

The Spitzer Mosaicking and Point Source Extraction (MOPEX) package (Makovoz et al., 2006) was used for background matching and also to remove cosmic radiation hits via dual outlier detection (spatial and temporal filtering). The "overlap" script used to apply correction offsets to frames near bright sources introduced a gradient across the mosaic as shown in Figure 5.2 and so was not used when producing the final mosaics. This resulted in approximately 10% offsets in the vicinity of two bright sources compared to the rest of the mosaic. The effect on measuring point source fluxes was negligible compared to the errors involved with the point source extraction process.

MOPEX was also used to mosaic the frames together to produce the final images and for point source detection. Point source detection was performed on a background subtracted signal-to-noise ratio image where the Gaussian noise was estimated using a 45 by 45 pixel sliding window. The detection threshold was set at the 5σ level with a minimum number of pixels per source of 4 to recover the faintest sources that were apparent from inspection of the image.

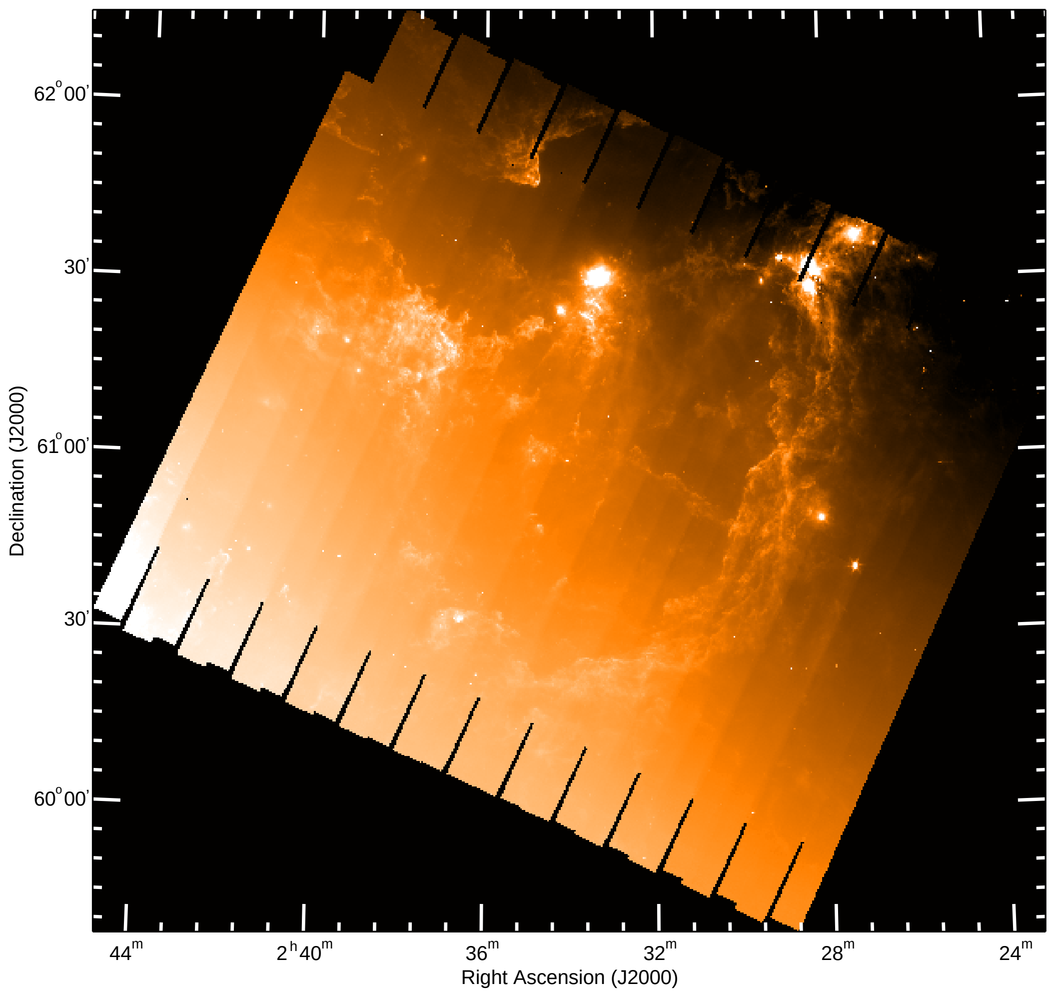

Figure 5.2: The 24 μm mosaic after offsets are applied to each frame using the overlap script in MOPEX. The intensity scale is linear from 0 to 60 MJy/sr.

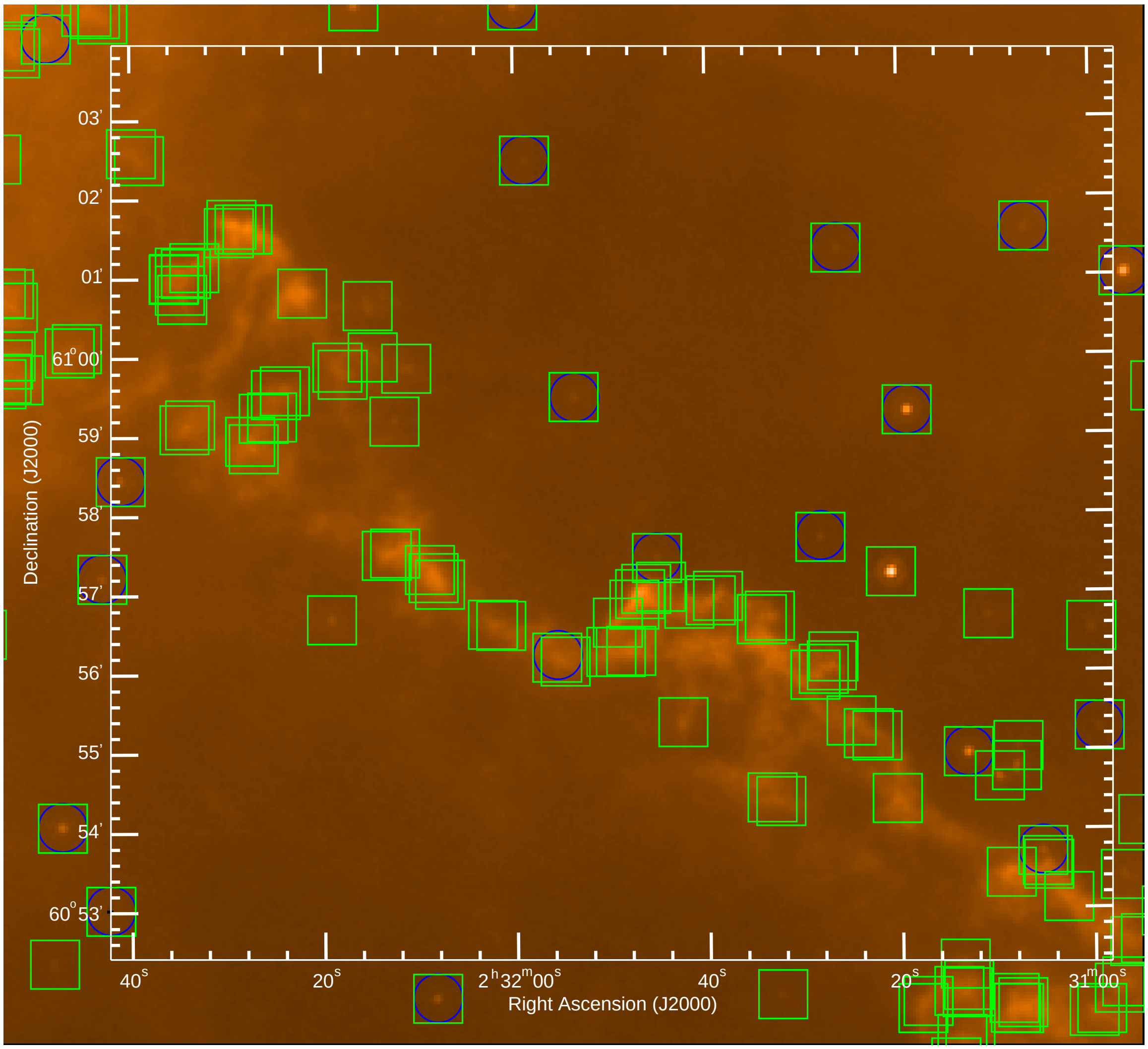

Figure 5.3: Detail of point source detections overlaid on part of the MIPS 24 μm image. The intensity scale is linear from 17 to 50 MJy/sr. Green squares show the positions of point source detections in the MIPS 24 μm image using MOPEX. Sources enclosed by blue circles also have matching 2MASS K Band detections found during bandmerging. Only sources with detections at both wavelengths were included in the detection list.

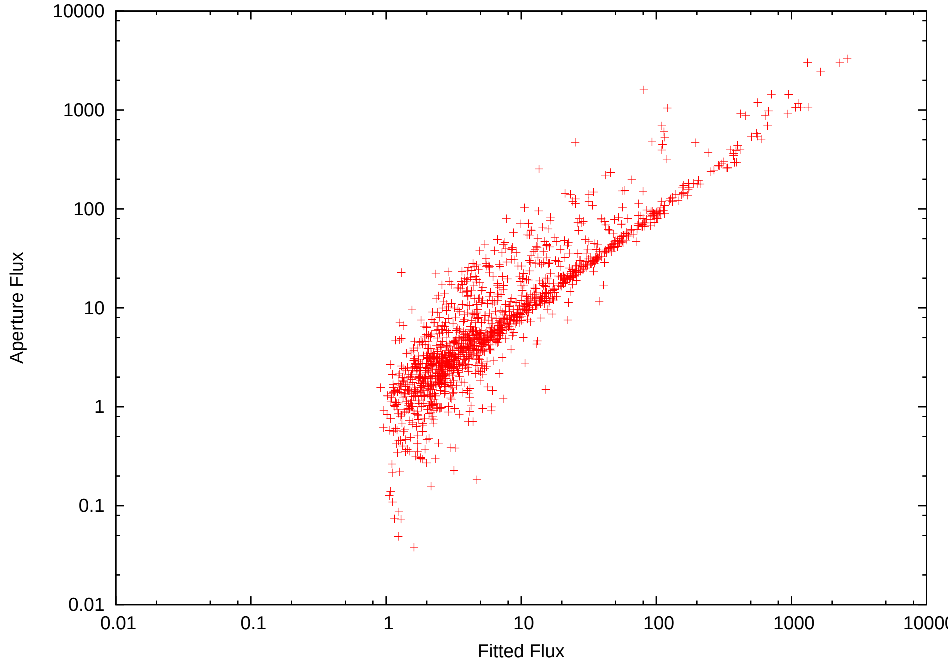

Figure 5.4: Aperture fluxes versus fitted fluxes for points sources detected in both the MIPS 24 μm image and 2MASS 'K' band image.

Although MOPEX provided the best reliability for detecting the faintest point sources, it also resulted in many false detections in the diffuse emission of the loop. Many of these false detections were eliminated later at the band merging stage. A custom program was written and used for bandmerging; requiring point sources in different bands to lie within 1 pixel of each other (2.45$''$ for MIPS 24 μm) to be matched. Some 2MASS K_s band point sources coincided with multiple false detections in the MIPS 24 μm image mostly due to incorrect deblending associated with bright sources. In these cases only the MIPS 24 μm point sources closest to the 2MASS position were included in the bandmerging.

For MIPS 24 μm sources with no corresponding 2MASS detection the source was removed as a false detection as shown in Figure 5.3. This step may remove young sources with a very steep SED, which may be detectable in the MIPS 24 μm mosaic and but not in 2MASS and this is discussed in Section 5.5.1. Some false detections also remained after the bandmerging step where 2MASS detections were closely aligned with the false detection in the MIPS 24 image and these were removed later by inspection of each individual MIPS point source detection.

Point source estimation was performed by both PRF (Point Response Function) fit-

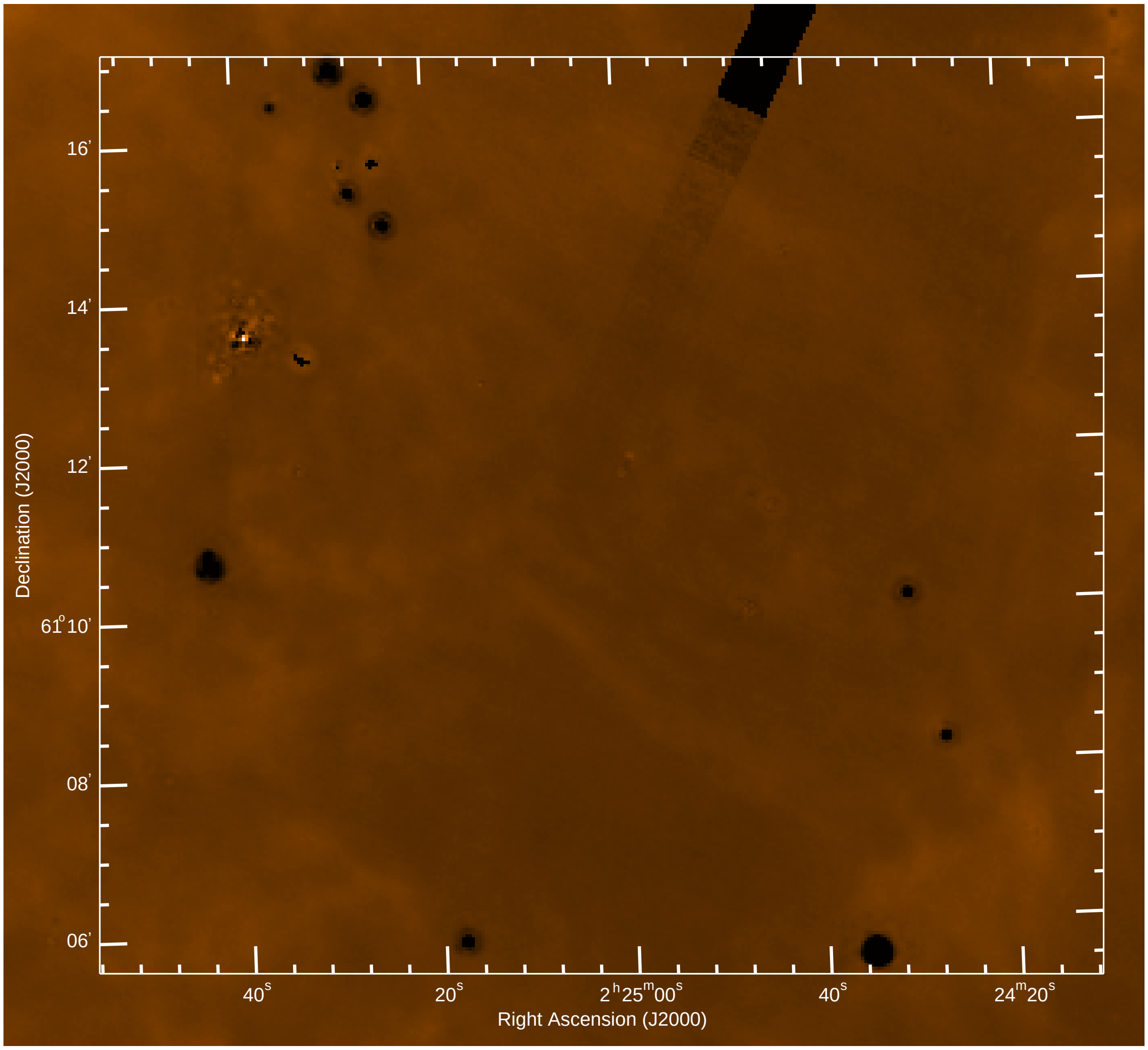

Figure 5.5: Detail of poor residuals observed in the MIPS 24 μm image with fitted fluxes subtracted; the dark spots result from sources whose fitted flux is overestimated. The intensity scale is linear from 17 to 60 MJy/sr.

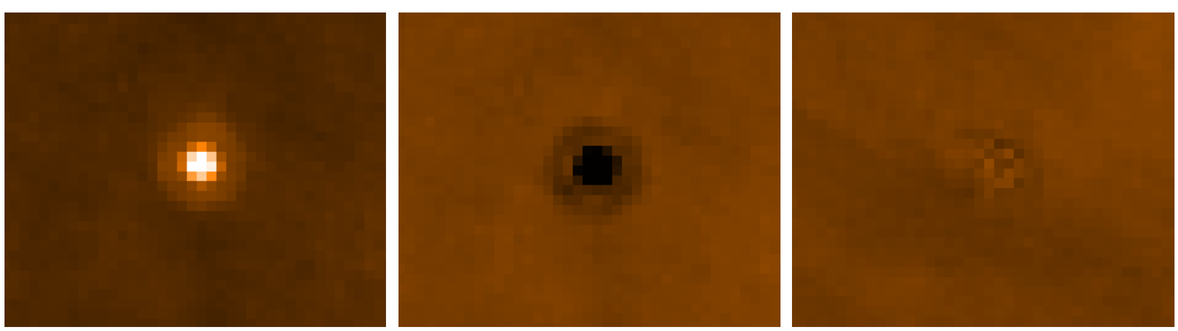

Figure 5.6: Left panel: A source detected using MOPEX. Centre Panel: A poor residual image following subtraction of an over-estimated PRF fit. Right Panel: An improved residual image following manual adjustment of the PRF fit.

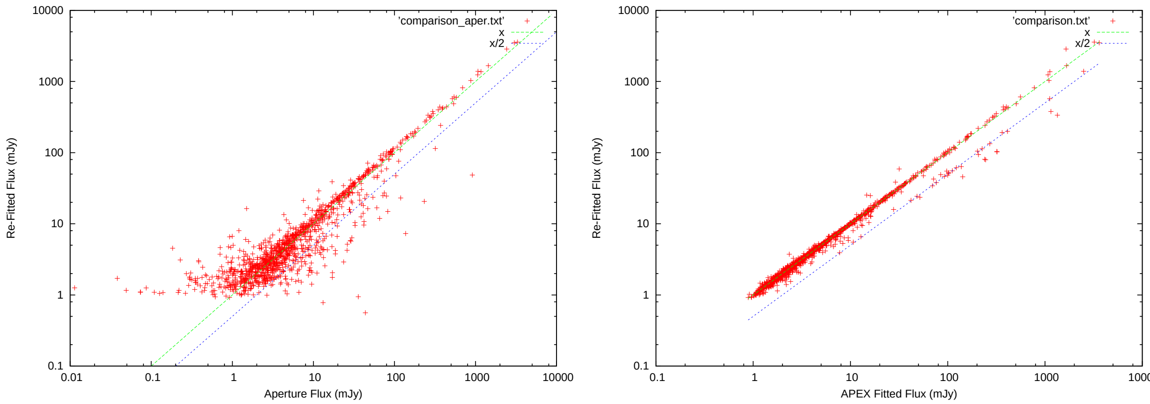

Figure 5.7: Refitted fluxes computed using custom program (courtesy of Tom Robitaille) to obtain flat residuals for each source, plotted against APEX aperture fluxes (left) and APEX fitted fluxes (right). The y=x and y=x/2 lines are also shown.

ting and aperture photometry of the detected sources using APEX with the final detection list following bandmerging. For the 2MASS sources with multiple matching MIPS 24 μm detections the fitted fluxes for each detection were summed to calculate a total 24 μm flux for the source that included each of the incorrectly deblended sources. For aperture fluxes, only the flux of the point source closest to the 2MASS position was used as using many apertures close to the source would result in over estimation of the flux. Figure 5.4 shows the aperture fluxes plotted against the fitted fluxes.

There are many sources where the aperture and fitted fluxes disagree by a factor of 10 or more. Figure 5.5 shows part of the point source subtracted image produced by APEX using the fitted flux values. Many poor residuals are observed as dark spots where the fitted fluxes have been significantly overestimated by APEX. Since the fitted fluxes appeared unreliable, aperture fluxes were used to obtain preliminary results but as many of the sources appeared adjacent to each other or in regions of bright diffuse emission it was likely that many of the aperture fluxes were also unreliable.

A custom program (courtesy of Tom Robitaille) was used to check the photometry of each source. Thumbnail images of each source and its corresponding residual were individually checked to ensure the detection was real and that each source had a corresponding smooth residual image following subtraction of the fitted photometry. In cases where the point source was real but the fitted flux was incorrect or misaligned, the position and brightness of the fitted PRF were adjusted to produce smooth residuals as shown in Figure 5.6. The adjustments to the position were less than 1 pixel (2.45$''$) and the corrections to the flux were less than 10%.

5.5 Identification and Classification of YSOs

The final MIPS 24 μm mosaic is shown in Figure 5.8. The 12 μm, 25 μm, 60 μm and 100 μm images retrieved from IRIS are shown in Figure 5.10. Figure 5.9 shows the detail around the star forming region AFGL 333 for SCUBA 850 μm and MIPS 24 μm.

Without IRAC data providing coverage in the 3-8 μm range, it is not possible to reliably fit radiative transfer model SEDs to the data or to produce colour-colour plots (e.g. Allen et al. (2004)). Robitaille et al. (2006) show that for 200,000 model SEDs produced using radiative transfer codes, only protostars with disc mass to star mass ratios greater than 10^{-6} have a K_s band - 24 μm spectral index greater than -2 as shown in Figure 5.11. Similarly, only protostars with an envelope accretion rate of 10^{-9} $M_{star} yr^{-1}$ will exhibit a spectral index greater than 0. Classifying sources using the 2-24 μm spectral index is subject to degeneracy; some models have envelope accretion rates greater than 10^{-9} $M_{star} yr^{-1}$ with non-positive spectral indices. Nevertheless, determining a spectral index for each source in the field will still give an indication of the stage of star formation for each part of the field on a cluster by cluster basis.

8116 sources were detected before bandmerging in the MIPS 24 μm image. After bandmerging, 1431 sources were found to also have a detection in the 2MASS K_s band, with the remaining sources discarded as false detections. Preliminary results were obtained using APEX aperture photometry. 78 sources had negative fluxes, these were typically faint detections in regions with high levels of clumpy background emission for which the background estimation was very likely poor. Closer inspection of these sources revealed that they were in fact false detections for which a spectral index could not be calculated and so they were discarded. From classification of the remaining 1353 sources using the K_s band to MIPS 24 μm spectral indices, 179 Class I sources, 477 class II sources and 697 Class III sources were identified in the field.

The custom refitting program was then used to manually check the point source detection and extraction. Inspection of the detections resulted in 114 sources being removed as false point source detections located in either diffuse emission or parts of bright sources. A further 34 sources had residuals that were over-subtracted near the centre of

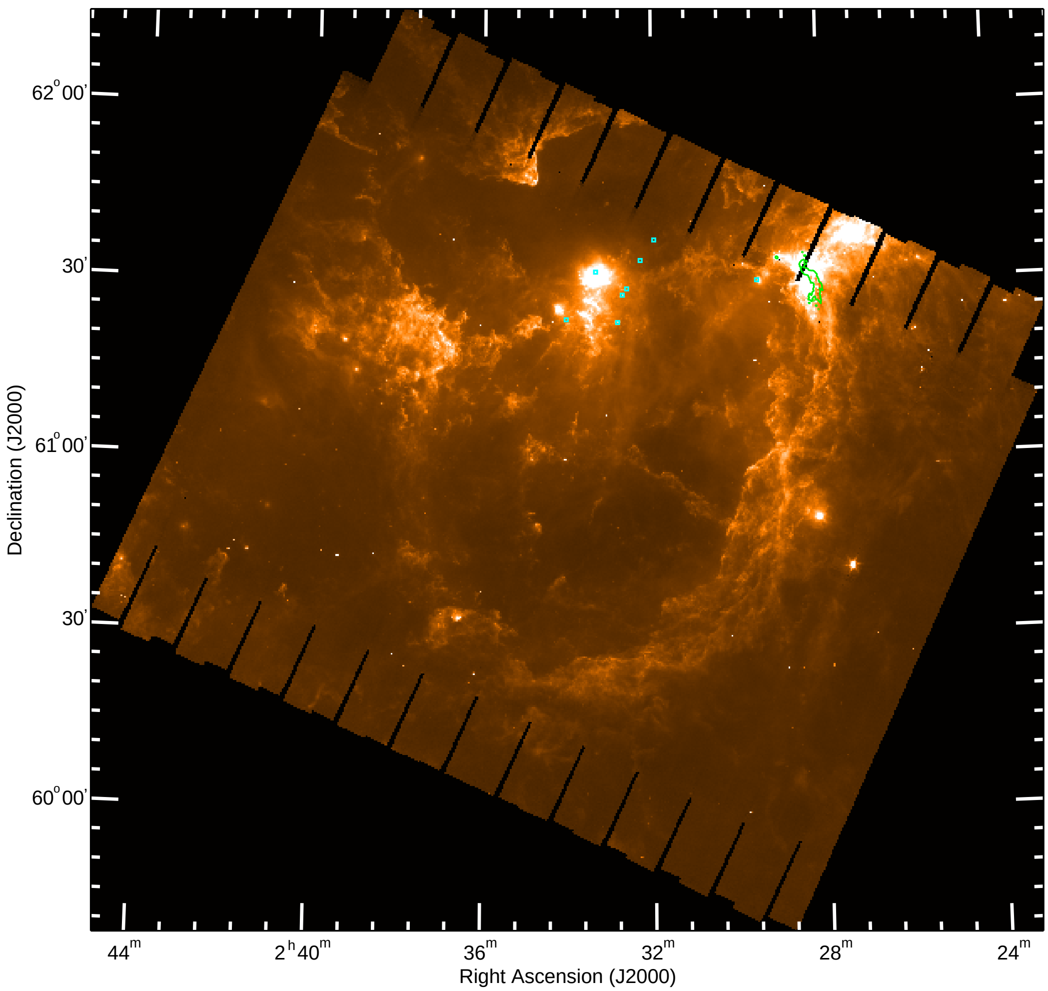

Figure 5.8: MIPS 24 μm mosaic of the entire region around W4 mapped in the survey, orientated with north pointing upwards. The intensity scale is linear from 17 to 60 MJy/sr. The contour indicates the position of AFGL 333, shown in more detail in Figure 5.9. The light blue squares indicate the positions of the O stars in the field.

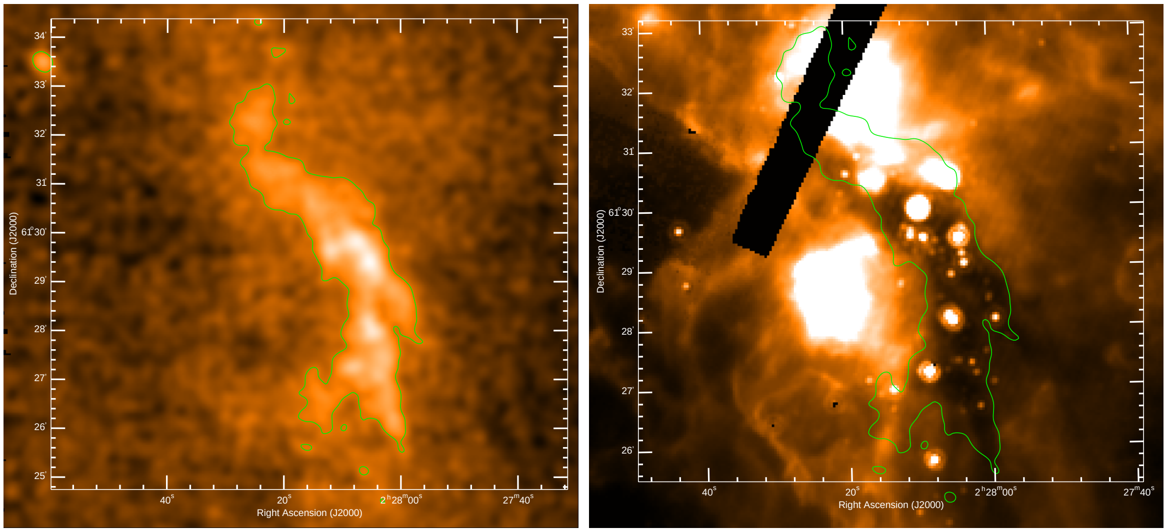

Figure 5.9: Detailed images of AFGL 333 used later when determining a dust temperature for the region. Left panel: SCUBA 850 μm image using a linear intensity scale from -85 to 298 MJy/sr. Right panel: MIPS 24 μm image using a linear intensity scale from 30 to 130 MJy/sr. Contours on both images trace regions with a flux density greater than 85 MJy/sr in the SCUBA 850 μm image.

the source but under-subtracted around it; these were identified as extended sources and were not included in the survey. Also not included were 16 sources within 3 pixels of the edge of the image and 5 blended sources for which it was not possible to reliably fit a PRF to the source. The remaining 1262 sources were used; corrections to either the flux or position were applied to 220 of the sources, with the remaining 1042 sources not requiring any correction.

A comparison of these refitted fluxes to both the aperture fluxes and fitted fluxes from APEX is shown in Figure 5.7. Despite the poor residuals observed resulting from subtraction of the PRF fits determined using APEX in Figure 5.5, the fitted fluxes from APEX are in reasonable agreement, with a few sources with fluxes computed using APEX a factor of $\sim$2 larger than the refitted fluxes. The aperture fluxes do not agree so closely, particularly for fainter sources, with several sources disagreeing with the refitted fluxes by a factor greater than 10. This is probably due to poor estimation of the background in regions with high levels of diffuse emission.

Using the refitted fluxes 65 Class I sources, 498 Class II sources and 699 Class III (no IR excess) sources were found in the field. A comparison of the spectral indices

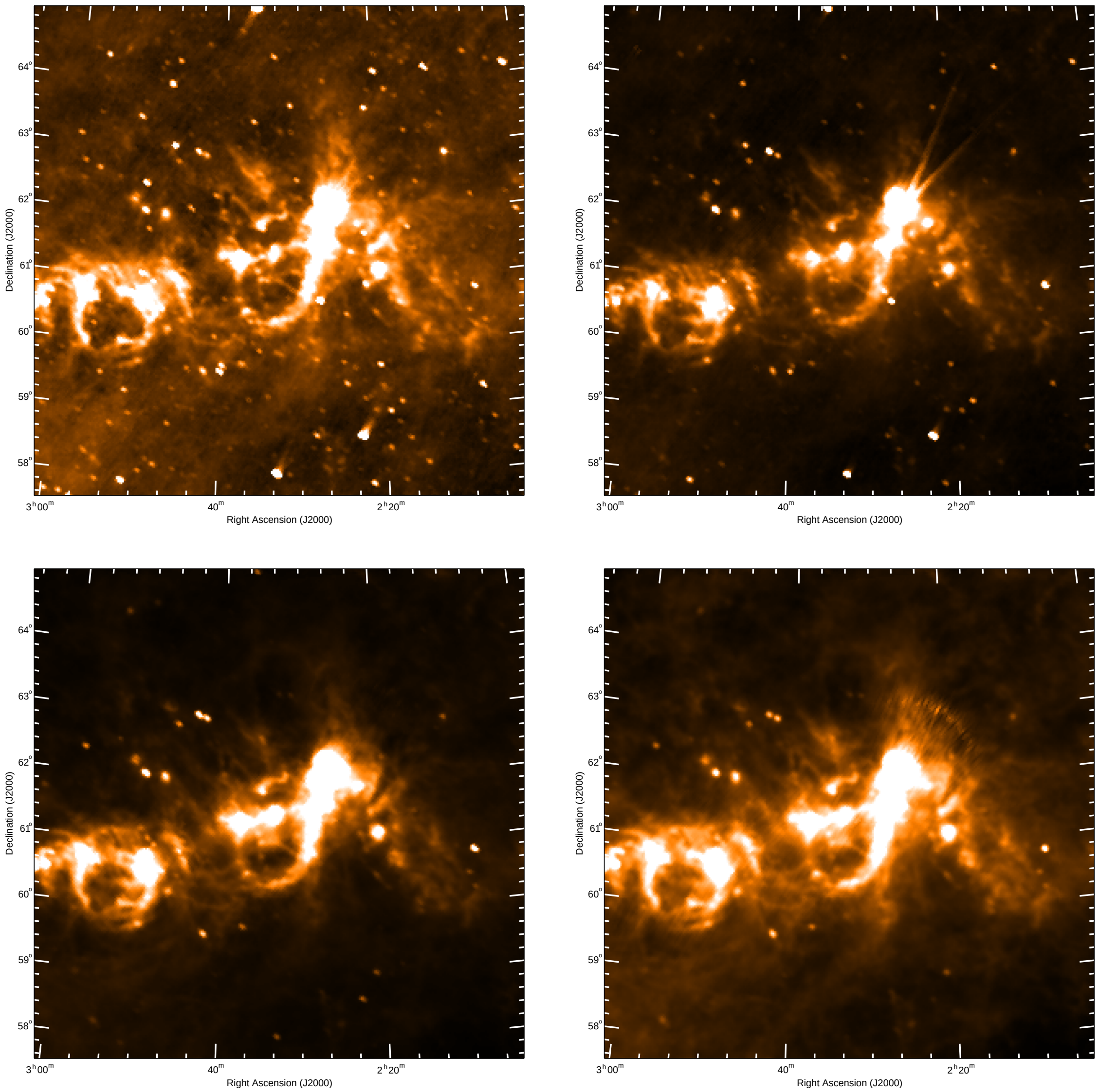

Figure 5.10: Images retrieved from the IRIS archives, Upper Left: 12 μm image using a linear intensity scale from 1 to 8 MJy/sr. Upper Right: 25 μm image using a linear intensity scale from 2 to 20 MJy/sr. Bottom Left: 60 μm image using a linear intensity scale from 3 to 100 MJy/sr. Bottom Right: 100 μm image using a linear intensity scale from 15 to 200 MJy/sr. The region covered includes W5, W4 and W3 as shown in Figure 5.1

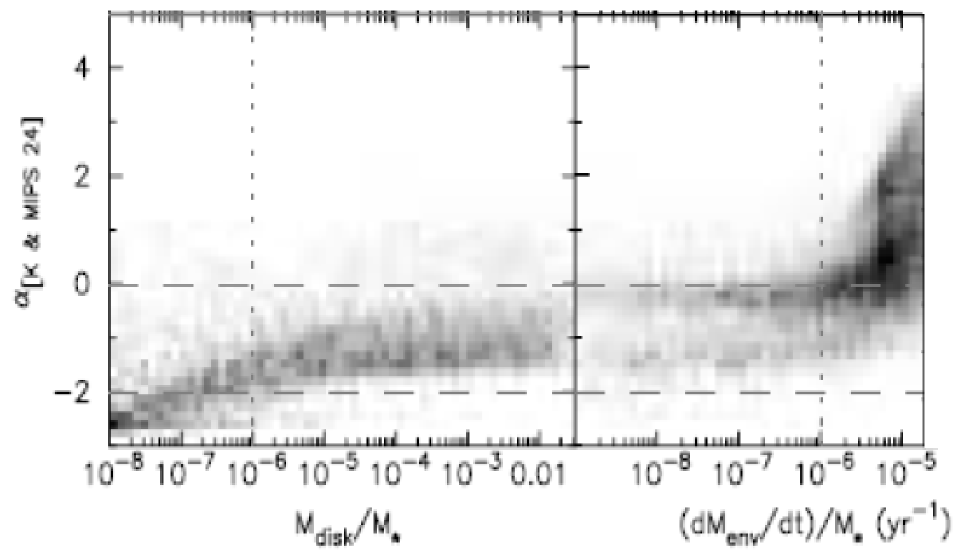

Figure 5.11: Spectral index plotted against disk mass for disk-only models (left) and envelope accretion rate for disk and envelope models (right) from Robitaille et al. (2006). The grey scale indicates the number of models using a linear scale. The dashed horizontal lines show the separation between Class III, II and I sources based on their spectral indices calculated using K_s band and MIPS 24 μm fluxes. (Figure from Robitaille et al. (2006)

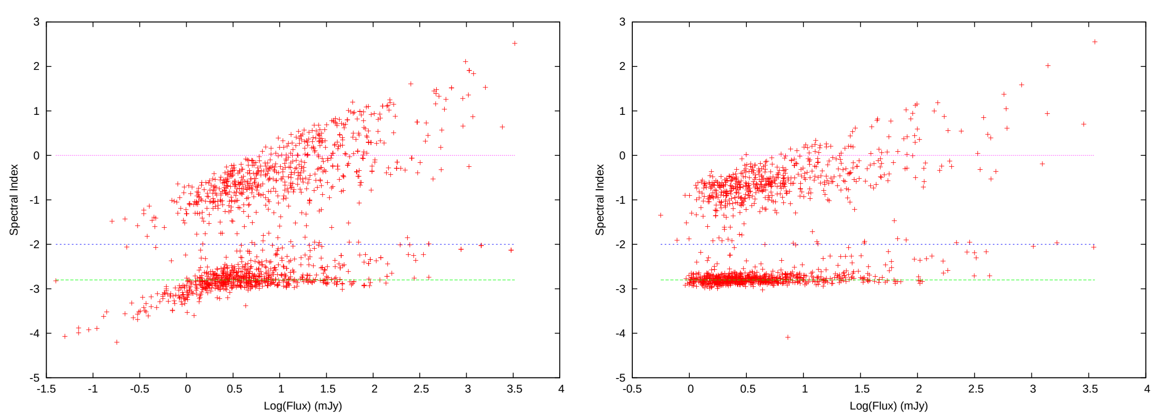

Figure 5.12: Spectral Index for each source plotted against the MIPS 24 μm flux using the APEX aperture flux (left) and the refitted flux (right). The lower horizontal line indicates a spectral index of -2.8; the source located nearby are likely stellar sources with no IR excess, the other horizontal lines show the boundaries between Class I, II and non-IR excess sources.

computed for each source plotted against 24 μm flux using both aperture fluxes and the refitted fluxes is shown in Figure 5.12. This demonstrates how the classification of sources is better defined using the refitted fluxes. The lower number of Class I sources identified after applying the corrections implies that many of the false detections in the diffuse emission were misidentified as Class I sources. The spatial distribution of each class is shown in Figures 5.13 and 5.14. Defining Class I and II sources as IR excess sources, 563 YSO candidates are found in the field using the final corrected fluxes. The faintest IR excess sources identified in the field had fluxes of 0.27 mJy in the 2MASS K_s band and 0.56 mJy in the MIPS 24 μm band.

5.5.1 Limitations of the Survey

The SED fitting technique used in Chapter 4 is conservative at defining a source as Stage I. For example, a disc viewed edge-on may exhibit a positive spectral index and thus be classified as Class I whilst the SED fitter may identify a number of models with or without envelope accretion, depending on the viewing angle and thus classify the same source as Stage I/II (Robitaille et al., 2006). An edge-on disc may exhibit a Class I SED but will typically be an order of magnitude fainter than if it were viewed pole-on. The Class I sources identified in this survey have a distribution of K_s band fluxes with a median the same order of magnitude as for that of the Class II sources which implies that the majority of Class I sources are not edge-on discs.

For comparison, the 751 IR excess sources identified in the RMC were reclassified using only the spectral indices calculated from the K_s band and MIPS 24 μm fluxes. Of the 751 sources, 409 sources did not have either valid K_s band or MIPS 24 μm fluxes and therefore could not be classified, 303 were classified as Class II sources and 39 were classified as Class I sources. Recall from Chapter 4 that 37 sources could only be fit by models with envelopes and 714 sources could be fit with disc models (some could be fit by either envelope or disc-only models). This demonstrates that using only the 2-24 μm spectral indices to classify the sources recovers very young sources (Class I) adequately but more than half of the Class II sources are not recovered. Thus, the fact that the proportion of Class I sources to the total number of IR excess sources is approximately 11% in the W4 survey compared to an analogous value of $\sim$5% in the RMC, very likely results from incompleteness in recovering the Class II sources using only 2-24 μm spectral indices.

From inspection of the MIPS 24 μm mosaic near AFGL 333 approximately 35 sources can be identified but only 8 of these sources had matching 2MASS K_s band fluxes following band merging. Therefore, around AFGL 333, the completeness is ~25% that of the MIPS 24 μm detection rate; this represents the worst case since the sources in this region are more deeply embedded than elsewhere in the field.

This survey is also not sensitive to young sources that do not exhibit an IR excess, however, as discussed previously in Chapter 4, for young clusters ~ 1Myr old, the disc frequencies are expected to be high (>80%) (Haisch et al., 2001b), with disc lifetimes of ~6 Myr. Given the age of ~1-4 Myr estimated for OCl 352 (Normandeau et al., 1996; Dennison et al., 1997) and the fact that any star formation in the field is expected to have occurred after the formation of OCl 352, then any clusters of YSOs could reasonably be expected to be $< \sim$3 Myr old and thus have disc frequencies >50% (Haisch et al., 2001b).

5.6 Spatial Distribution of IR Excess Sources

In Figure 5.14 the Class I and II sources are not spread evenly throughout the field and some sources appear to be arranged in distinct clusters. By following similar calculations used to quantitatively assess the degree of clustering in the RMC, direct comparisons can be drawn between the two star forming regions.

Figure 5.15 shows the nearest neighbour distribution for the Class I and II sources constructed by determining the log of the separation for each IR excess source to its nearest neighbour. Poisson statistics were used to compute the nearest neighbour distribution for a random sample of points distributed uniformly across the field (Gomez et al., 1993). The IR excess sources identified in the field show a significant excess at separations from $9''$ to $57''$ compared to the random sample of points.

The fifth nearest neighbour can be used to compute the local stellar surface density at each of the IR excess sources which can be used to quantify to what degree the protostar is forming in a clustered environment (Gutermuth et al., 2005). A cumulative frequency plot for the local stellar densities computed for each IR excess source and for a random sample of points is shown in Figure 5.16. The IR excess sources exhibit a larger spread

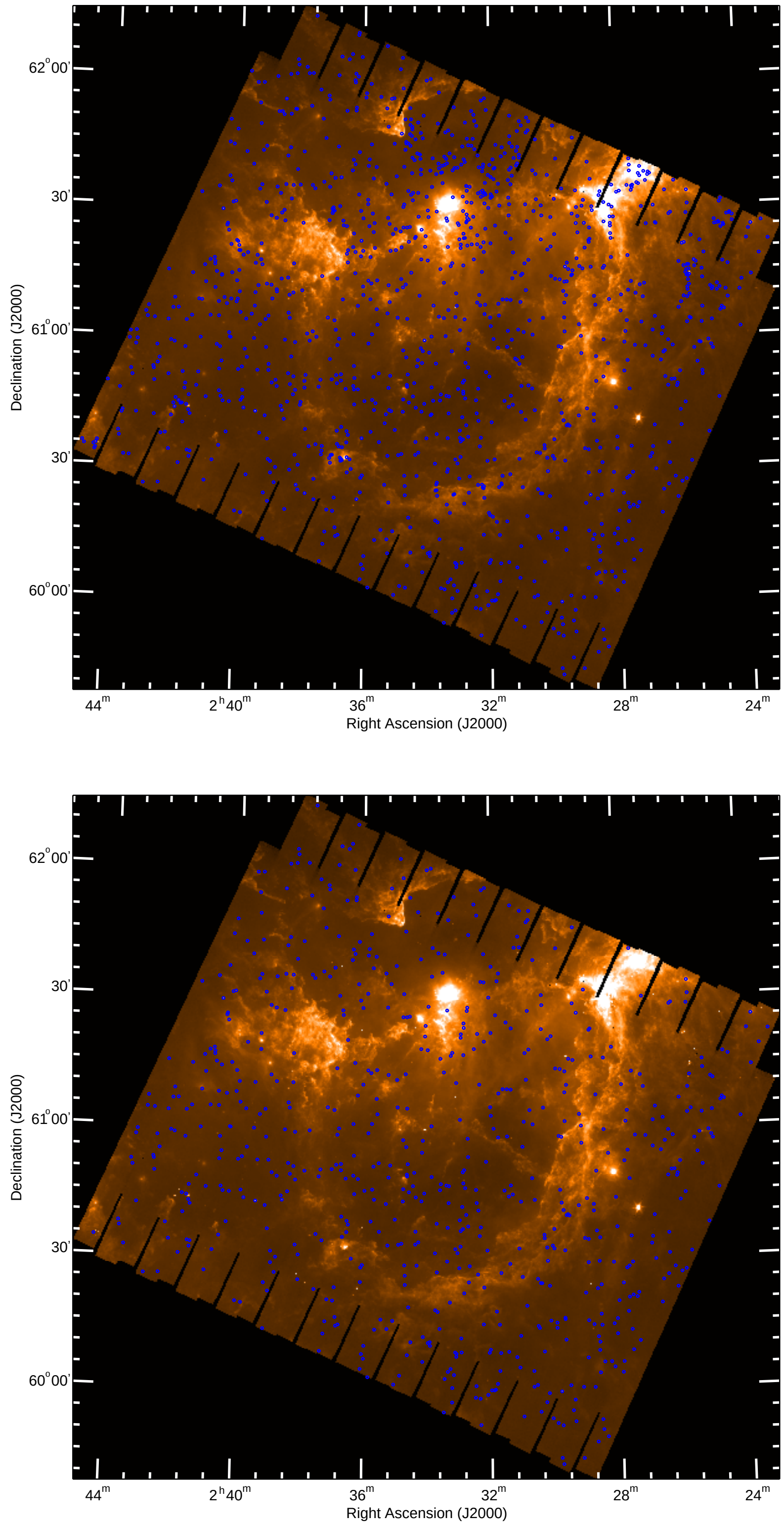

Figure 5.13: Spatial distribution of the sources identified in the field and classified using K - 24 μm spectral indices overlaid on the MIPS 24 μm image. The intensity scale is linear from 17 to 60 MJy/sr. Upper Panel: All sources with point source detections in K_s band and 24 μm. Lower Panel: Sources with spectral indices between -3 to -2 (Class III).

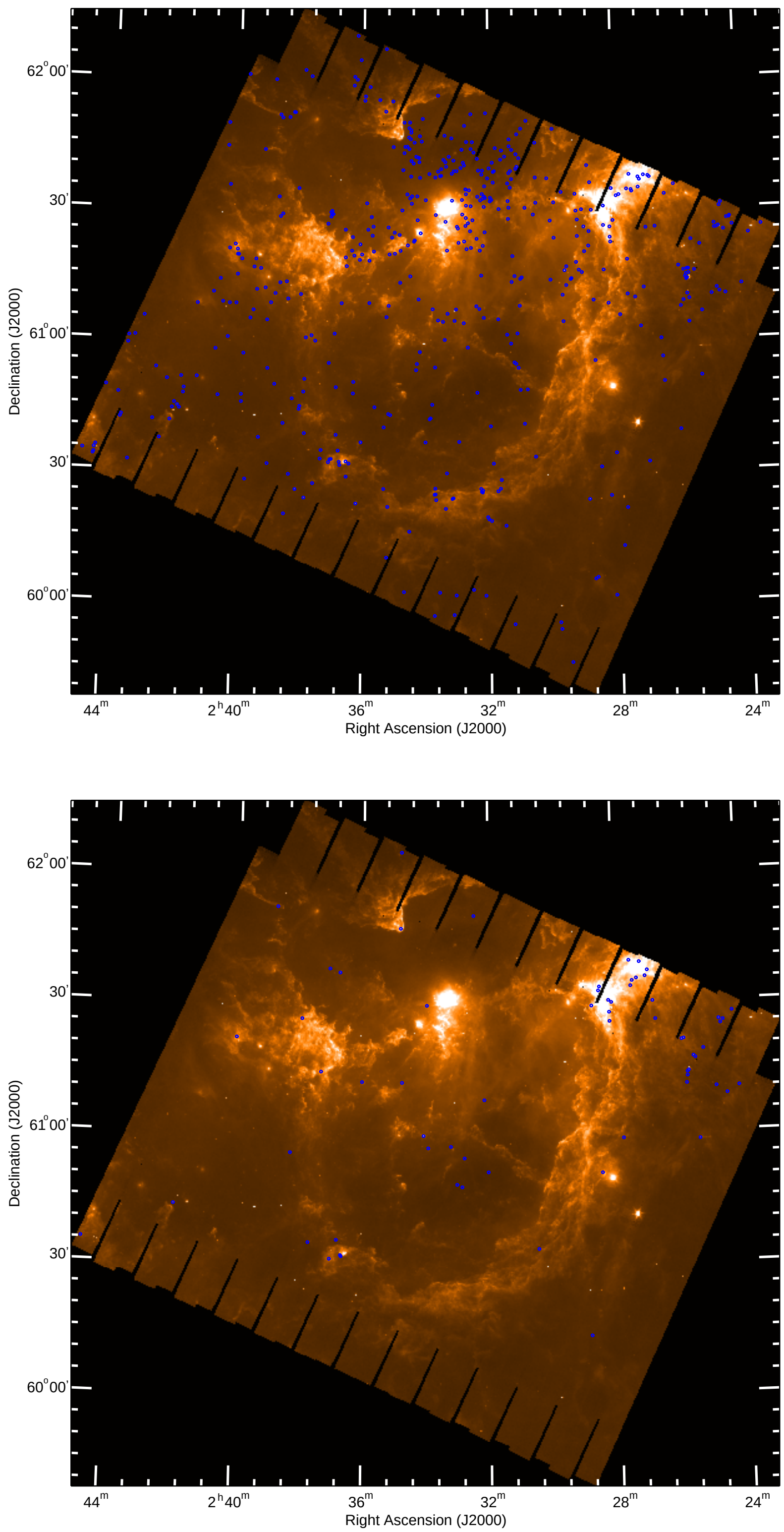

Figure 5.14: Spatial distribution of the sources identified in the field and classified using K - 24 μm spectral indices overlaid on the MIPS 24 μm image. The intensity scale is linear from 17 to 60 MJy/sr. Upper Panel: Sources with spectral indices between -2 and 0 (Class II). Lower Panel: Sources with positive spectral indices (Class I).

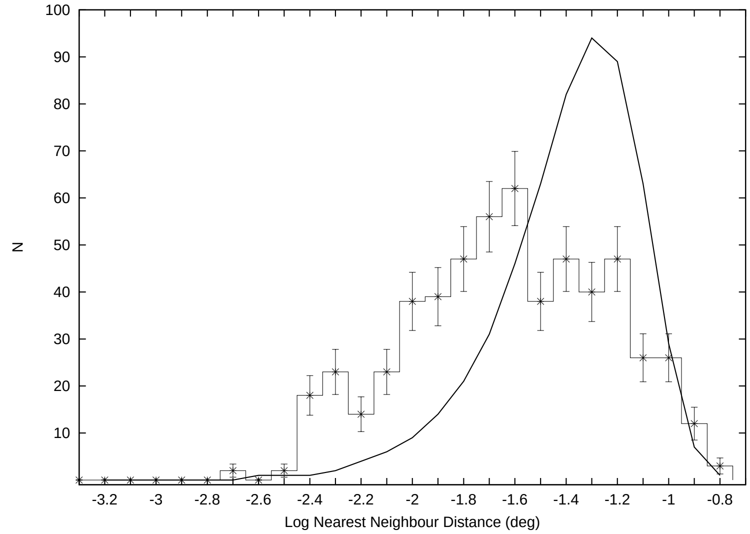

Figure 5.15: Number distribution of the projected separation distance between nearest neighbours for the 563 IR excess sources found in the field. The solid line is the expected distribution for a random (Poisson) distribution for the same number of objects over an identical area. Error bars are calculated from square root number statistics.

of local densities compared to the sample of points randomly distributed throughout the field. This demonstrates that a siginificant proportion of the sources are confined to certain regions of the field resulting in higher local stellar densities.

Figure 5.17 was constructed by computing the local stellar densities at each pixel in the image using the fifth nearest neighbour to the pixel centre. The local stellar densities of IR excess sources computed for the W4 loop are smaller by approximately a factor of 10 than for the Rosette Molecular Cloud. This can be accounted for by the difference in the distance of 1600 pc to the RMC and and 2300 pc to W4 and also the limitations of the survey associated with the absence of IRAC data. Therefore, as for the Rosette, it is necessary to define a cluster in terms of the local stellar densities and limitations of the survey specific to W4.

Figure 5.17 also shows the results for a similar analysis for a random sample of points uniformly distributed across the same area. 99% of the pixels have a value less than 0.35 stars pc^{-2} and this value is adopted as the contour used to define clusters in the field. Only groups of points of 5 or less members bound by this contour are present in the random sample and so groups of 6 or more IR excess sources bound by this contour are identified as clusters in the real data.

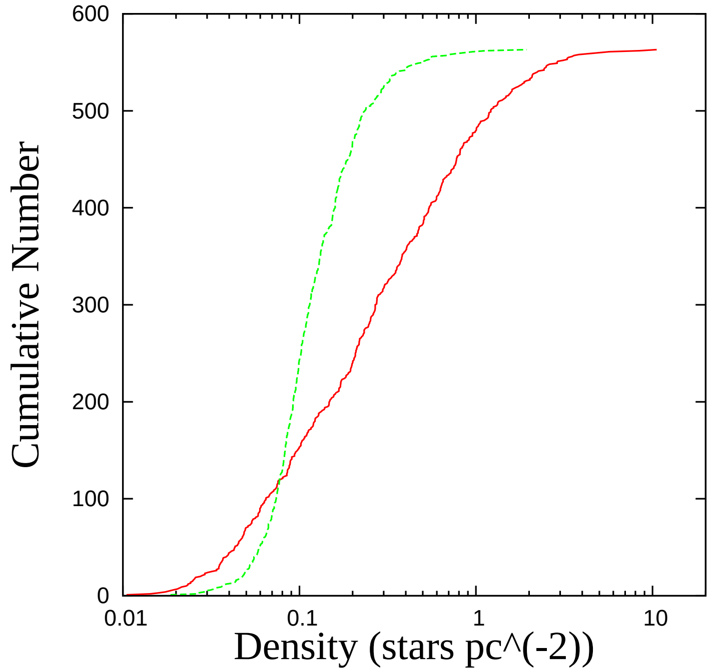

Figure 5.16: Cumulative frequency plot of the local stellar densities computed at the position of each IR excess source. Solid Line: Using the the real IR excess sources detected in the survey. Dashed line: Using the same number of sources randomly and uniformly distributed in the same area of sky.

Table 5.1: Properties of the clusters of IR excess sources found using local stellar densities. The numbers in brackets indicate the number of class I sources in each cluster. The cluster locations are shown in Figure 5.21 and images of each of the clusters are shown in Figure 5.18.

Cluster ID	R.A. h:m:s	dec $^{\circ}$:$'$:$''$	Number of IR Sources (class I)	Area (pc^2)	Density (stars pc^{-2})	Distance from W4 loop centre (pc)	Notes
I	02:24:31.453	+61:25:54.76	13(4)	19.64	0.66	44.36	NW
II	02:25:41.712	+61:13:45.93	19(6)	28.43	0.67	36.32	W, Elongated
III	02:27:41.357	+61:32:33.88	29(11)	52.47	0.55	33.83	Southern clump is AFGL 333
IV	02:29:17.414	+61:15:41.41	6(0)	9.53	0.63	20.83	Inside of loop near AFGL 333
V	02:32:50.920	+61:37:39.79	102(1)	169.37	0.60	26.10	Agglomeration, North of OCl 352
VI	02:36:50.807	+60:32:42.05	14(4)	20.76	0.67	26.04	Southern part of loop
VII	02:37:01.444	+61:28:40.41	6(0)	11.74	0.51	28.34	E, just outside of loop
VIII	02:40:02.934	+61:20:40.24	6(1)	12.45	0.48	37.68	E of loop

Eight clusters of IR excess sources are observed in the vicinity of the W4 loop and their properties are summarised in Table 5.1 and the detail of the clusters I, II, IV, VI, VII and VIII is shown in Figure 5.17. Cluster III consists of two groupings of sources bound by one contour of which the southern clump represents AFGL 333 and Cluster V is the agglomeration of IR excess sources north of OCl 352 and the detail of these two clusters is shown in Figure 5.19.

5.7 Star Formation Efficiency in the W4 Loop

The submillimetre spectrum of a cool cloud of temperature, $S_\nu(T)$, can be fit by a modified blackbody curve:-

$$S_\nu(T) \propto B_\nu(T)\nu^\beta \tag{5.1}$$

where S_ν(T) is the blackbody intensity and β is the index giving the frequency dependence of the emissivity $Q(\nu)$, varying between 1 and 2 (Hildebrand, 1983).

Hildebrand (1983) showed that the mass, M, of a cloud can be calculated using:-

$$M = \frac{S_\nu D^2 C}{B_\nu(T)} \tag{5.2}$$

where D is the distance to the cloud, S_ν is the measured flux at frequency ν and C is the coefficient for the estimate of the cloud mass. C is given by:-

$$C = \frac{(4/3)a\rho}{Q(\nu)}\frac{M_g}{M_d} \tag{5.3}$$

where a is the dust grain size, $Q(\nu)$ is the emissivity of the dust grains with a ν^β dependence, M_g is the mass of the gas and M_d is the mass of the dust in the cloud.

Figure 5.9 shows a contour tracing flux densities greater than 8×10^{-3} mJy/pixel for AFGL 333 in the SCUBA 850 μm image. This contour was used to define the region in which the flux of AFGL 333 was measured in the IRIS 12, 25, 60 and 100 μm images. The MIPS 24 μm image was not used to measure the flux as the coverage in this region was incomplete (see Figure 5.9). However, the flux measured in the incomplete MIPS 24 μm map agreed within 2% of the flux measured in the same area in the 25 μm IRIS image, implying that the IRIS fluxes for this region are accurate to within a few percent.

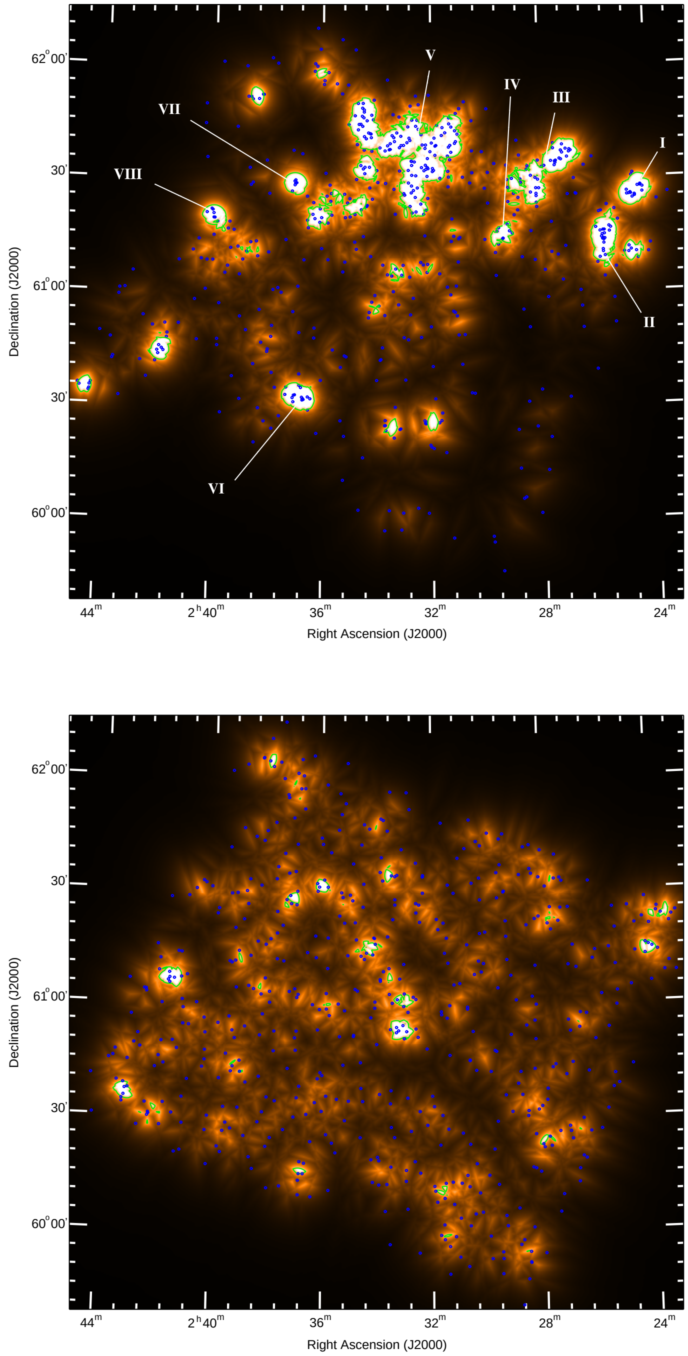

Figure 5.17: Upper panel: Contours overlaid on stellar density maps covering the MIPS 24 μm field indicating local stellar surface densities for the 563 IR excess sources found from the determination of spectral indices. The intensity scale is linear from 0 to 0.5 stars pc^{-2}. Blue dots show the position of the IR excess sources and the green line highlights the 0.35 stars pc^{-2} contour used to identify the clusters labelled. Lower panel: Density map for a random sample of 563 points distributed over the same area for comparison.

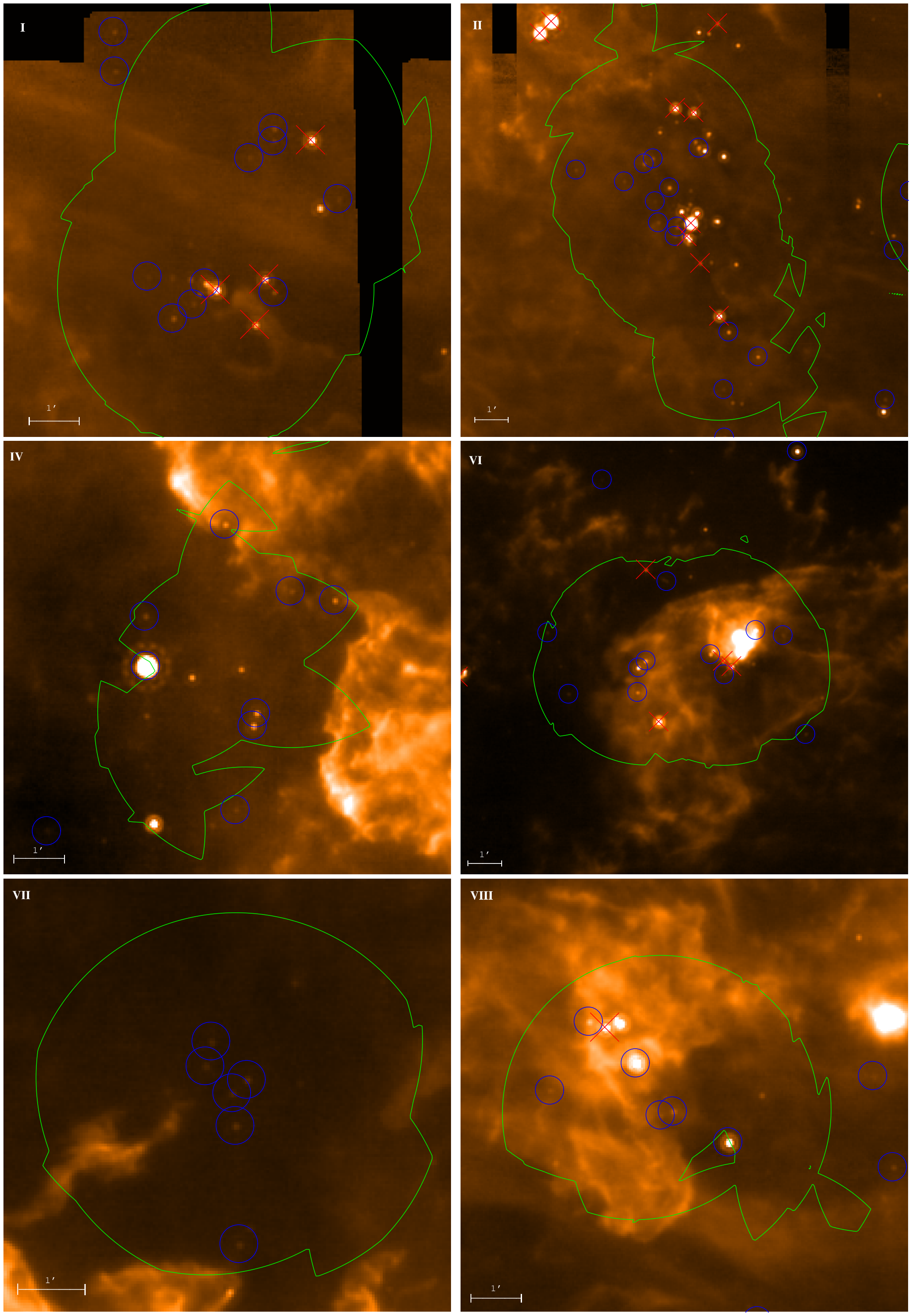

Figure 5.18: Detailed MIPS 24 μm images of the new clusters of IR excess sources identified in this survey and with their positions identified in Figure 5.21. Blank (black) pixels result from incomplete coverage. Red crosses show the position of Class I sources and blue circles show the position of Class II sources. The green contour indicates regions where the local stellar density of YSOs is greater than 0.35 stars pc^{-2}.

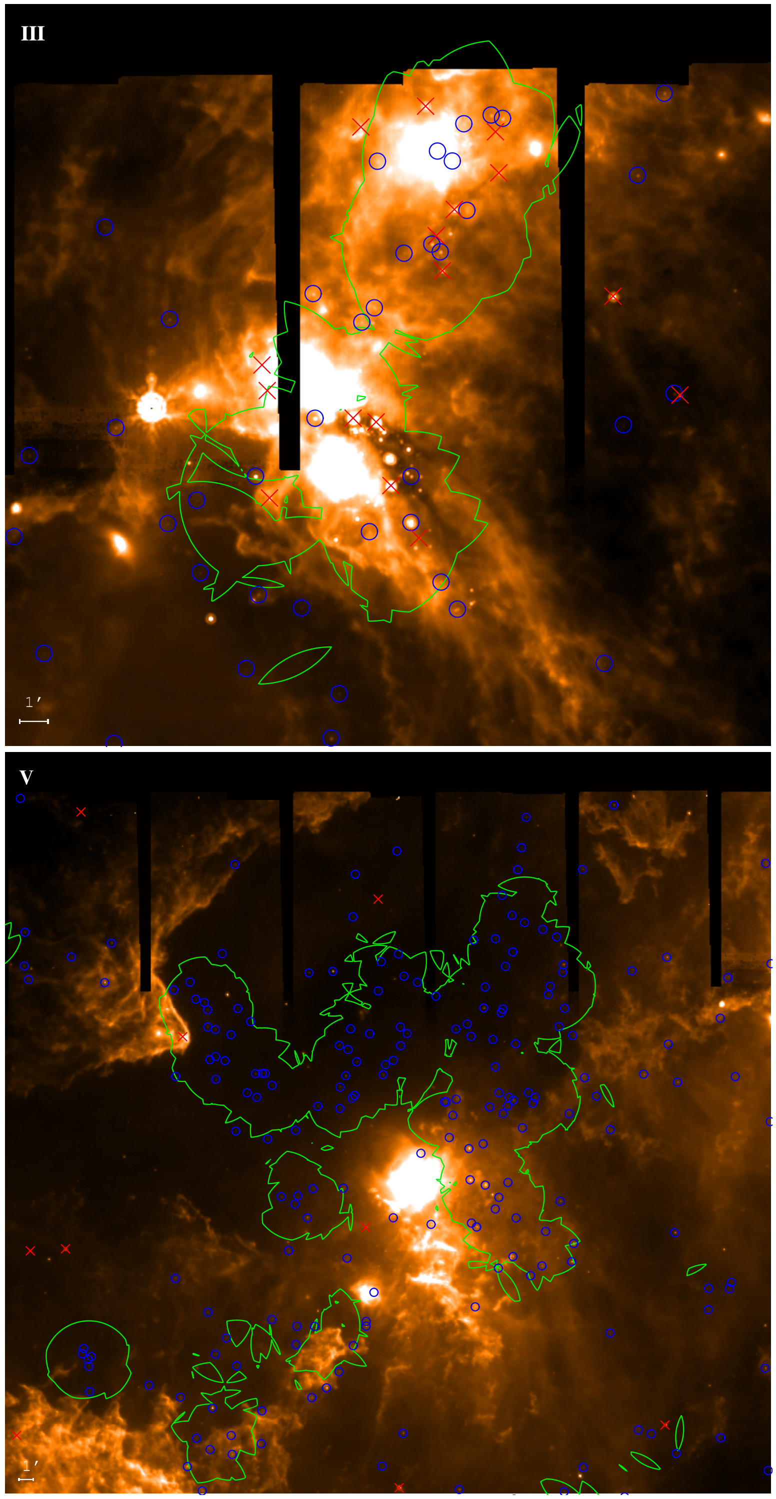

Figure 5.19: Detailed MIPS 24 μm images of the new clusters of IR excess sources identified in this survey and with their positions identified in Figure 5.21. Blank (black) pixels result from incomplete coverage. Red crosses show the position of Class I sources and blue circles show the position of Class II sources. The green contour indicates region where the local stellar density of YSOs is greater than 0.35 stars pc^{-2}.

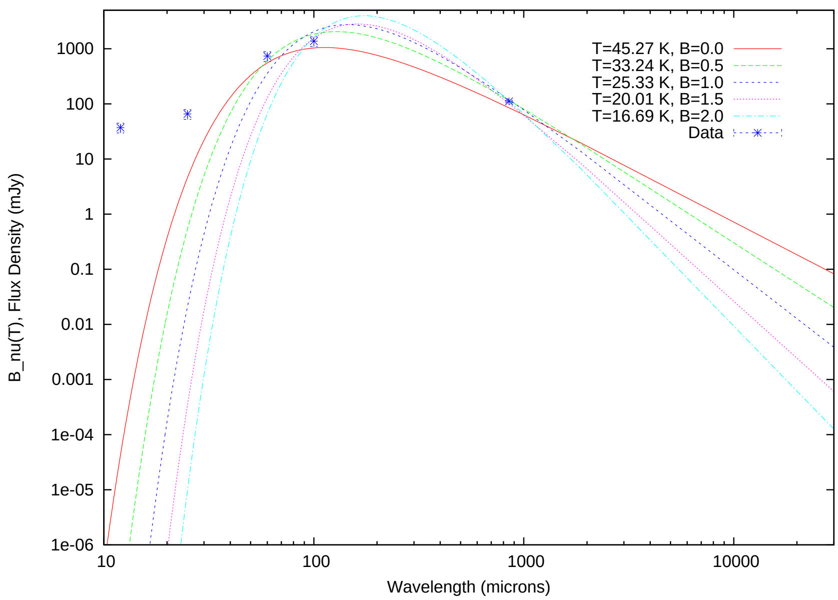

Figure 5.20: Total fluxes contained within the 8×10^{-3} mJy per pixel contour shown in Figure 5.9 in each of the IRIS images and SCUBA 850 μm image. The lines indicate the best fit blackbody curves through the 60 μm, 100 μm and 850 μm points for values of β between 0 and 2, with corresponding values of T from the best fits shown. The assumed errors on the 60 μm, 100 μm data points were 10% and 5% on the 850 μm data point.

When fitting a modified blackbody curve using the IRIS 12, 25, 60 and 100 μm and SCUBA 850 μm data points it was clear that the 12 and 25 μm data points could not be fit to any greybody curve, presumably due to contamination of the measured flux by starlight. It is also clear in the 24 μm image (Figure 5.9) that the cloud appears dark around the stars in the cluster which would also affect the flux measured from the 25 μm IRIS data.

Figure 5.20 shows the best fit curves through the 60 μm, 100 μm and 850 μm points for β values between 0 and 2 with resulting measures of the temperature from those fits. The best fit is obtained using values of $\beta = 0$ and T = 45 K. Adopting values of 100 kg m^{-2} for C at 250 μm (Hildebrand, 1983), 2300 pc for D, the distance to W4 and 110 Jy for S_ν at 850 μm, the mass of the cloud for the AFGL 333 region is calculated to be 200 M$_\odot$ for a temperature of 45 K.

For greybodies, Hildebrand (1983) states that β values are expected to vary from 1 at < 200 μm to > 2 at wavelengths > 1000 μm (Erickson et al., 1981; Schwartz, 1982). Using β values from 1 to 2, the temperature of the dust is calculated to be 17-25 K. The 60 μm point lies significantly ($>2\sigma$) above the best fit line for the $1 < \beta < 2$ fits and so a temperature of 45 K is used here in subsequent calculations when determining the star formation rate. However, any stars with envelopes within the contour may contribute to the 60 μm flux so it is noted that using temperatures ranging between 17-25 K results in a range of masses of the cloud in AFGL 333 of 1400-8700 M$_\odot$.

The locus occupied by the W4 loop in the 24 μm mosaic is defined to include only pixels with values above 30 MJy/sr and lying within 20-50$'$ of the centre of the W4 loop. The total flux contribution from the W4 loop in the IRIS 100 μm data using this locus is measured to be $\approx$40,000 Jy with a corresponding flux measurement of 1367 Jy for AFGL 333. The contour around AFGL 333 therefore includes $\sim$3.4% of the total flux in the ring at 100 μm and since mass is proportional to the measured flux assuming the same temperature throughout the loop, the total mass of the ring is estimated to be $\sim$6000 M$_\odot$.

The 2MASS K_s band and MIPS 24 μm point source detections appear to be complete down to fluxes of $\sim$0.7 mJy and $\sim$2 mJy respectively. In both bands this implies that the majority of sources are detected down to $\sim$0.5 M$_\odot$ based on the fluxes of the models of Robitaille et al. (2006), assuming ages of 0.9-1.1 Myr. Using the IMF adopted by Kroupa (2001), the mean mass for the initial mass function (IMF) for masses > 0.5 M$_\odot$

is 1.3 $M_\odot$ and the survey detects approximately 68% of the mass in the stars (Kroupa, 2001). There are 121 IR excess sources situated in the locus of the W4 loop, giving a total mass of stars forming of ~230 $M_\odot$ assuming a mass of 1.3 $M_\odot$ for each source and correcting for the missing mass of the IMF by multiplying by a factor of 0.68^{-1}. Thus, a star formation efficiency of ~4% is estimated in the W4 loop. If the dust is very cold (17 K, $\beta = 2$) then the total cloud mass is ~250000 $M_\odot$ and the star formation efficiency is only ~0.09%. A star formation rate of 2.3 $\times 10^{-4}$ $M_\odot$ yr^{-1} is determined, based on the assumption that the young stars detected are typically ~1.0 Myr old.

The number of bubbles of similar size to W4 (20-30 pc in radius) in the Galaxy is calculated to be approximately 500 assuming an exponential function with a scale length of 2 kpc and maximum height above the plane of 0.2 kpc and the number density of HI shells of similar size from Daigle et al. (2007). Therefore, over the whole Galaxy the contribution to the star formation rate is 0.1 $M_\odot$ yr^{-1}. The Galactic star formation rate is estimated to be ~3-5 $M_\odot$ yr^{-1} (Smith et al., 1978; Miller & Scalo, 1979; McKee, 1989; Timmes et al., 1997; Diehl et al., 2006) and therefore the contribution to the total star formation rate from star forming bubbles similar to W4 in the Galaxy is estimated to be ≈2.5%.

5.8 Evidence for Triggering

Figure 5.21 shows the spatial distribution of Class I and II sources and the positions of the clusters identified in the field. The Class I sources are generally not distributed as widely as the Class II sources and appear to be more abundant to the north west of the field in clusters I-III, near the interface with the W3 star forming region. The Class I sources located near the centre of the loop may be located in the near or far part of a three dimensional shell and their apparent position near the centre of the loop would therefore result from projection. Figure 5.22 shows the density of IR excess sources and mean pixel fluxes in circular annuli using 5 pc bins centred on the W4 loop as shown in Figure 5.23. There is no apparent overdensity of IR excess sources coincident with the peak of the radial profile of the loop located at 20-25 pc from the loop centre.

Elmegreen (1998) cite W4 as an example of large scale triggered star formation caused by the accumulation of material swept up by the expansion of the loop. The

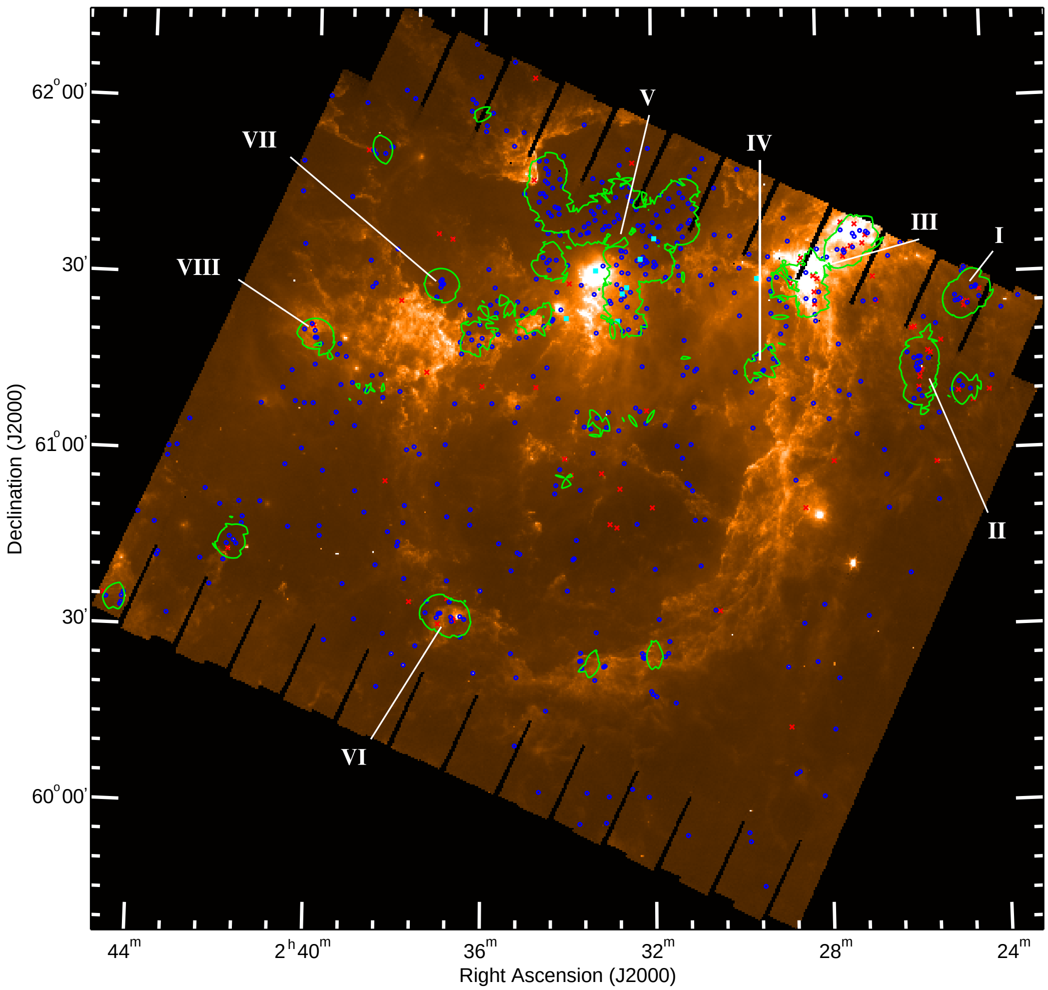

Figure 5.21: Spatial distribution of the IR excess sources (Class I and II sources) identified in the survey overlaid on the MIPS 24 μm image. The intensity scale is linear from 17 to 60 MJy/sr. Red crosses show the position of Class I sources and dark blue circles show the position of Class II sources. The green contour indicates the regions where the local stellar density of IR excess sources is greater than 0.35 stars pc^{-2}. The light blue squares indicate the positions of the O stars in the field.

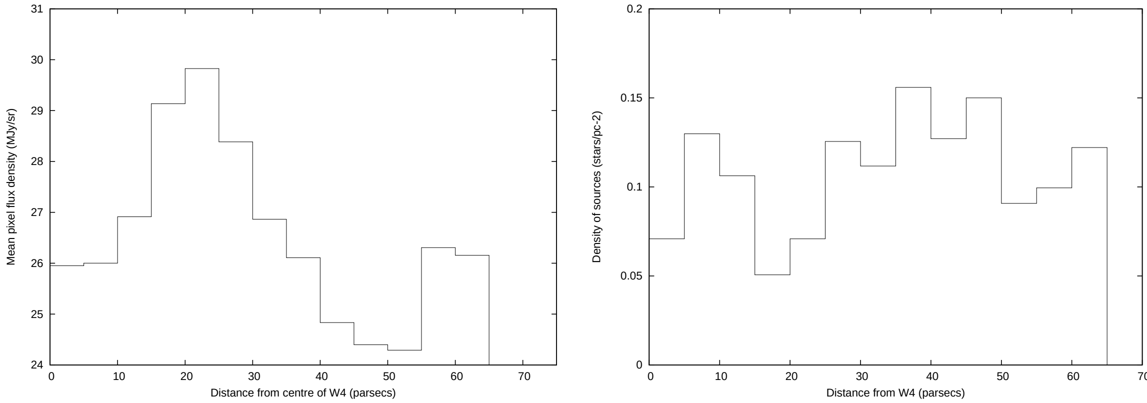

Figure 5.22: Left: Radial profile of the W4 HII region using mean pixel flux densities calculated in annuli centred on the centre of the W4 loop using 5 pc bins as shown in Figure 5.23. Right: Histogram of IR excess source surface densities observed within the same annuli.

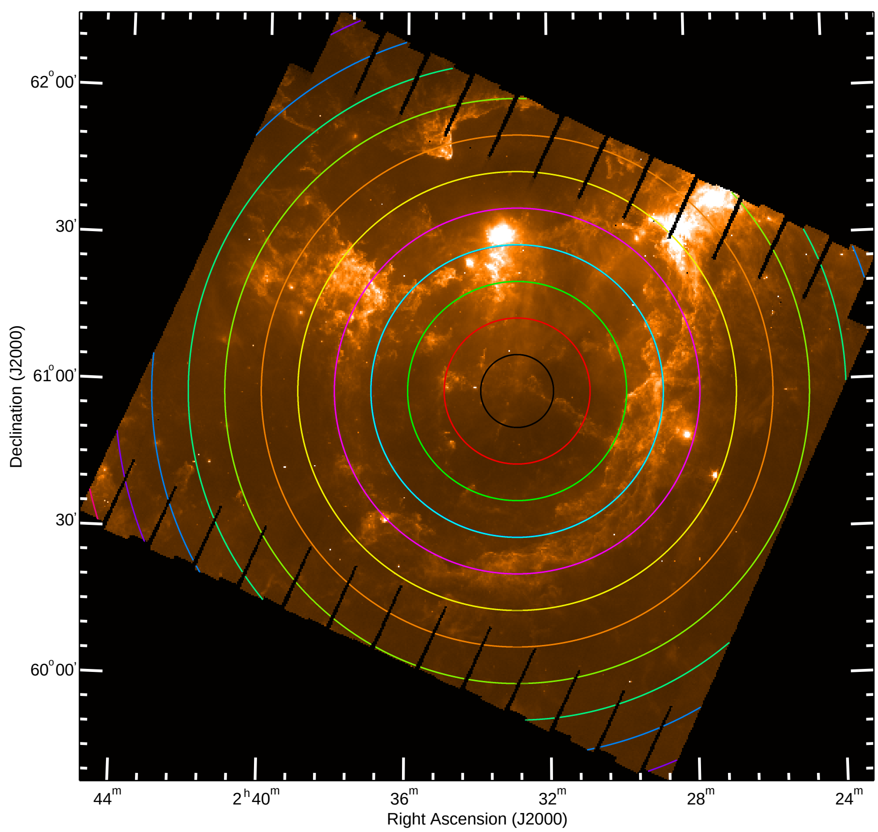

Figure 5.23: The position of the 5 pc annuli used in Figure 5.22. The intensity scale is linear from 17 to 60 MJy/sr.

southern half of Cluster III is identified as AFGL 333 in the north western part of the ring and Cluster VI is located in the south of the loop. Both of these clusters in the loop contain both class I and II sources suggesting that star formation is still taking place. The location and young age of the stars within these clusters compared to OCl 352, which has an age estimated to be between $\sim$1.3-4.3 Myr (Dennison et al., 1997; Normandeau et al., 1996), are consistent with some triggered star formation occurring within the swept shell of W4. Cluster VI in particular does not appear to have any recent star formation taking place around it. However, OCl 352 is near the ring, so star formation is not co-eval if the loop is a remnant produced from a previous burst of star formation and not driven by winds from OCl 352.

The northern half of cluster III is located 5 pc north-west of AFGL 333 and also contains a similar proportion of class I sources. This cluster is aligned with diffuse emission in the 24 μm image but this clump appears to be located outside of the main loop and about 10pc south of the neighbouring W3(OH) region. Star formation appears to be ongoing in this cluster but does not appear to be directly associated with the ring. It is therefore plausible that the W4 loop has expanded into a clumpy medium in which star formation was already occurring.

Clusters I and II are located beyond the ring and are not coincident with any diffuse emission. About one third of the IR excess sources identified here are class I sources, implying that star formation is taking place here without any accumulation of material by the loop. These clusters are also located too far from IC 1795 located in W3 to be part of the three generation triggering suggested by Oey et al. (2005).

Cluster IV is located on the inside edge of the W4 loop. The positions of the IR excess sources close to the 0.35 star pc^{-2} contour defining the cluster suggest that its inclusion as a cluster may result from the chance alignment of distributed sources. It contains no Class II sources and so star formation appears complete here.

Cluster V is the large agglomeration of sources to the north and east of OCl 352 which only contains 1 Class I source for which the proportion of IR excess sources classified as Class I is much lower ($\sim$1%) than seen in Clusters I, II, III and VI where the proportion is typically 30-35%. This suggests that the star formation in this region is nearly complete and occurred before the on-going star formation seen in Clusters VI, and the north-west part of the field (Clusters I-III). These IR excess sources do not appear to be triggered by the expanding shell and are not coincident with any diffuse emission. If the Class II sources are ∼1 Myr old then they are still younger than OCl 352 with an estimated age of 1-4 Myr. Therefore, their formation may have been triggered previously by winds from OCl 352, with the cloud out of which they formed now dispersed by the winds.

Clusters VII and VIII are located towards the east of the field and are not located in the locus of the W4 loop defined in Section 5.7. In these clusters, 1 source out of 12 is classified as Class I which, like Cluster V, implies that star formation is mostly complete here. Their positions outside of the loop is not consistent with the notion that their formation has been induced by the expansion of the W4 loop.

Clusters VI and AFGL 333 are located in the W4 loop and it is possible that in these cases that the sweeping up of material by the shell has accelerated star formation and in the case of cluster VI induced star formation in a region where none was taking place. However, the fact that Clusters I, II and the northern half of Cluster III contain young Class I sources and are located outside of the W4 loop indicates that star formation may already be occuring in parts of the field that do not appear to have yet interacted with the W4 loop. Thus, the distribution of IR excess sources in the field can be also explained by the expansion of the W4 loop into a clumpy medium in which star formation has already taken place to the north (in the case of Cluster V) and is still in progress to the northwest (in the case of Clusters I, II and III). Overall, there is little evidence of co-eval star formation in a recent burst in the ring clouds.

5.9 Summary

The evidence for triggered star formation in the swept-up shell in the region around the W4 loop is examined. The close to circular morphology of the loop suggests that it may be a remnant from a previous HII region or supernova but there is no pulsar detected to confirm the latter. Another possibility is that the expansion is driven by outflows and winds from O stars in the cluster OCl 352 but this cluster is not centrally located, residing instead in the north ridge of the ring.

AFGL 333 is one of two clusters located in the observed ring, consistent with compression of the cloud as material is swept-up. However, there are several clusters in other parts of the field which include Class I sources indicating that star formation is already occurring in parts of the cloud not yet swept up. The formation of a large agglomeration of Class II objects north of OCl 352 may have been triggered by OCl 352 prior to the formation of the other clusters in which star formation is still occurring. AFGL 333 appears to be part of a larger structure into which the W4 loop is expanding. The presence of Class I sources further into the structure suggests that star formation is already taking place here without the need for further compression of the cloud by the expansion of the loop. Therefore, while it is possible that the expansion of the W4 loop triggered the onset or accelerated the star formation in AFGL 333, the process may have occurred on a similar timescale without the influence of the expanding shell. Like the Rosette, it is not clear that the dominant mode of star formation is triggering associated with the expanding shell.

The dust temperature of AFGL 333 is estimated to be 45 K resulting in a cloud mass estimate of 6000 $M_{\odot}$ for the W4 loop. The star formation efficiency is estimated to be $\sim$4% in the loop and the contribution to the Galactic star formation rate from similar sized shells in the galaxy is estimated to be $\approx$2.5%.

CHAPTER 6

Conclusions and Future Work

6.1 Conclusions

6.1.1 Survival of Discs in Star Forming Regions

This thesis has derived information from the detection of circumstellar discs as a means of investigating the environments in which planets (Chapter 3) and stars (Chapters 4 & 5) form. As discussed in Chapter 1, disc survival lifetimes set constraints on the timescales of planet formation.

In Chapter 4, a survey of YSOs in the Rosette Molecular Cloud is presented where NGC 2244, the ionising cluster at the centre of the nebula, is believed to be approximately 2-3 Myr old (Balog et al., 2007). In Chapter 5, a similar survey of YSOs is presented for the W4 loop with age estimates of the structure ranging from 6-20 Myr (Oey et al., 2005) for the superbubble and ∼1-4 Myr for the cluster OCl 352, containing 9 O stars. These surveys use near and mid IR data which is sensitive to young sources with an IR excess. The number of discless sources (young sources with no IR excess) is difficult to estimate using this data, particularly in the interiors of clusters. However, from IRAC band 1 star counts, one cluster in the RMC for which the survey of the IR excess sources appears most complete demonstrates that the number of cluster members with discs may be as high as ∼80%, consistent with the disc frequencies found in other young clusters by Haisch et al. (2001b).

Haisch et al. (2001b) found from L band excesses that in young clusters the disc lifetimes are ∼6 Myr. Haisch et al. (2001a) found that in the star forming region IC 348 the disc lifetimes are shorter for discs around stars earlier than G-type, approximately

2-3 Myr. Theoretical studies (Johnstone et al., 1998) and observational evidence (Balog et al., 2007) suggest that discs around early type stars or discs in close proximity to O stars have shorter lifetimes. Johnstone et al. (1998) applied a model of photoevaporation of circumstellar discs by external UV radiation from neighbouring hot stars to YSOs in the Orion Nebula to show that their discs were destroyed via this mechanism. The final disc size predicted after 1 Myr of radiation from a source at a distance of 0.3 pc was less than 1 AU. Balog et al. (2007) found evidence that in NGC 2244, the open cluster at the centre of the Rosette Nebula, the fraction of stars with a disc was lower (27%) for stars located within 0.5 pc from an O star than those located futher away (45%).

The field covered in the survey of W4 contains 8 O-stars and the dense ridge of the RMC (excluding NGC 2244) contains 1 O-star and over both regions there are $\sim$5 YSOs with discs (but not envelopes) within 0.5 pc of these stars. Due to the difficulties in finding discless sources it is not possible to test whether the fraction of sources with discs is consistent with the results of Balog et al. (2007) for NGC 2244. However, this does demonstrate that some YSOs are forming close enough to O-stars that their discs may be subject to photoevaporation by UV radiation (Johnstone et al., 1998), but some still survive in the Class II stage.

Lada & Lada (2003) state that the majority of stars form in embedded clusters. In the RMC, approximately 50% of the IR excess sources are located in clustered environments with high stellar surface densities. The corresponding fraction in the W4 sample is $\sim$30%. Contrary to Lada & Lada (2003), there is a minority of stars forming in clusters and this is probably due the incompleteness of the survey due to some YSOs not exhibiting an IR excess and blending of close sources.

In both the RMC and W4 the fraction of the youngest (Class I) sources found in a clustered environment is 38%. In W4, the large agglomeration of IR excess sources to the north of OCl 352 contains only 1 Class I source, compared to the smaller, more tightly bound clusters for which the fraction of YSOs that are Class I sources is in the range 29%-36%. The fraction of Class I sources found in clustered environments in the RMC is much lower ranging from 0-25%, probably due to bias of only using MIPS 24 μm data for W4 which favour the detection of very young objects and some edge-on Class II objects may be misidentified as Class I objects. However, there is little evidence in either region for a recent burst of star formation producing mainly Class I objects.

Any disc around a given star is generally more likely to be within 0.5 pc of an O star if it is a member of the same clustered environment. The RMC and W4 surveys show that ∼5 IR excess sources outside of NGC 2244 have angular separations from O stars that imply that they may be within 0.5 pc if they are at the same distance along the line of sight as the O star. This implies that the destruction of discs via irradiation of UV photons from nearby O stars is only a small factor affecting the disc survival rate.

If the lifetime of the disc is shorter than the timescale for the formation of planetesimals then this will have implications on the fraction of stars with planetary systems for stars forming in clustered environments. The environments that may be favourable to the formation of stars may not necessarily also be favourable to the survival of the protoplanetary disc and the subsequent formation of planets. The formation of planetesimals in the protoplanetary discs of stars in clusters must have occurred within the ∼6 Myr timescale of the disc lifetime. Stars forming within 0.5 pc of an O-star likely have their discs destroyed too quickly (within 1 Myr) to form planetesimals, although very few examples of such were found. It is possible that sources close to O stars that have already had their discs destroyed are missed by these surveys but even if this is the case, in both regions the O stars are only located in particular regions of the clouds so most stars will still form >0.5 pc from O stars.

Without growth of planetesimals in the protoplanetary disc, debris discs such as that seen around ϵ Eridani would also not develop around the host star as it requires continual replenishment from collisions of larger bodies that formed in the disc. Since 70-90% of stars are expected to have formed in clusters (Lada & Lada, 2003), the observed incidence of debris discs around main sequence stars of 16-17% (Trilling et al., 2008; Habing et al., 2001) could be representative of planetary systems that form around rarer stars forming in distributed populations. If this were the case it would imply that the timescale for disc survival in clusters was too fast for planetesimals to form. However, it would be difficult to form the <15% of stars with giant planets Fischer et al. (2003) and the 16-17% with planetisimal discs (with little overlap of systems) just from the <30% of distributed stars.

6.1.2 Tracking Features of the ϵ Eri Debris Disc

In Chapter 3 the evidence for rotation of the substructure in the debris disc around ϵ Eridani is examined following on from the work of Greaves et al. (2005). This is the first attempt to quantitatively detect and measure the motion and rotation of clumps in a dusty disc around another star.

The clumps in the dusty ring are believed to be caught in gravitational resonances by the outward migration of a planet (Wyatt et al., 2003) and to orbit the star at faster than the Keplerian rate (Ozernoy et al., 2000; Quillen & Thorndike, 2002) because they are co-rotating with a planet located closer to the star. Radial velocity and transit techniques normally used to detect extra-solar planets are limited to finding planets out to $\sim$5 AU from their host stars (see Figure 6.1). Tracking the rotation of disc features in a debris disc relatively close to the Sun and face-on it is possible to infer the existence of a Neptune-like planet out to distances $\sim$30 AU from the star. Apart from ϵ Eridani the only other debris disc with resolved structure and oriented close to face-on is that associated with Vega.

The task of tracking disc features is made significantly harder by the presence of background galaxies in the field of view. Identifying the size and position of clumps in the disc using clumpfinding algorithms is hampered by the irregular shape of the clumps. Data at 850 μm wavelength were previously obtained using the Submillimetre Common User Bolometer Array (SCUBA) over periods in 1997-1998 and 2000-2002. By χ^2 fitting after shift and rotation operations, images from these two epochs were compared to recover proper motion and orbital motion of the disc. The same procedures were then performed on simulated images to estimate the accuracy of the results. For ϵ Eridani, the fitted rate is $\sim 2.75 \pm 1.5^{\circ} yr^{-1}$ consistent with a planet orbiting at 26$\pm$9 AU.

However, the rate of rotation cannot be uniquely identified using the simulated data set even with the inclusion of a third epoch SCUBA-2 image. The rotation rates recovered with or without the third epoch SCUBA-2 image are about half the input rates. The underestimation and deviation of the rotation rates recovered from the simulated datasets are caused by apparent distortions of the structure in the disc caused by chance alignment with background galaxies coincident with the ring. This effect gets worse for larger rotation rates and longer periods and the $2.75^{\circ} yr^{-1}$ recovered over the 4 year period may already be an underestimate.

Even so, future observations with SCUBA-2 can rule out no rotation of the ϵ Eridani dust clumps with $\sim 4\sigma$ confidence. Assuming a rate of about 2.75° per year, the rotation of the features after a 10-year period could be shown to be $\geq 1^{\circ}$ per year at the 3σ level; faster than the Keplerian rate of rotation.

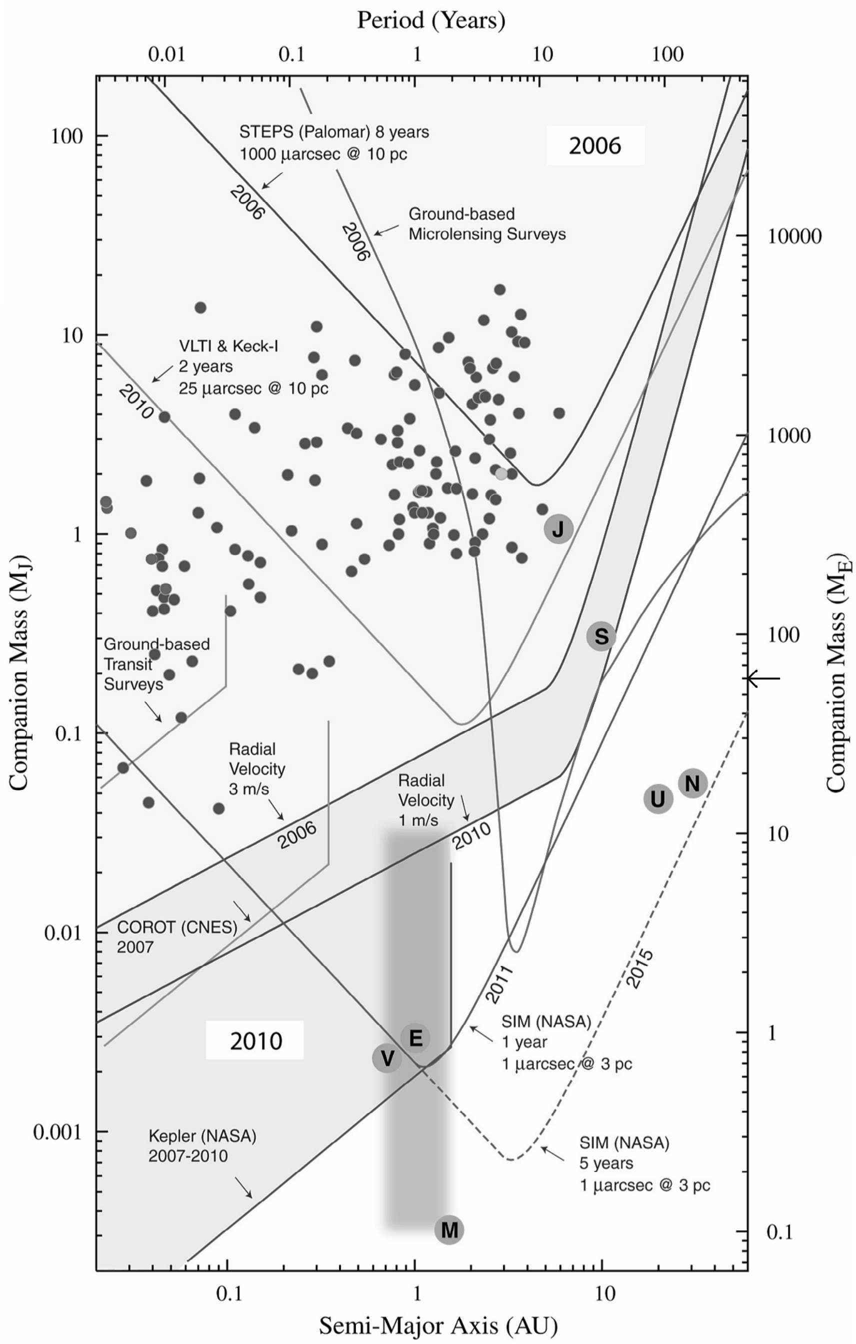

Figure 6.1: The parameter space for the masses and orbital radii of extra solar planets probed by various planet hunting techniques. Solar system planets are also included. Figure Courtesy NASA/JPL-Caltech (P.R. Lawson, S.C. Unwin, and C.A. Beichman (2004)). The planet predicted to be perturbing the ϵ Eridani debris disc (Ozernoy et al., 2000) with Semi-Major Axis 60 AU and Mass of 0.2 M_J would occupy a position indicated by the arrow on the right hand axis.

The ϵ Eridani disc represents an analogue of the young solar system with the K2V host star being of similar spectral type to that of the Sun and having a known planet detected via radial velocity techniques. The planet in this system will be undergoing a heavy bombardment phase similar to that experienced by the Earth in the early solar system. However, the 1.7 M_J mass planet orbiting at 3.4 AU detected from radial velocity measurements (Hatzes et al., 2000) will likely be more efficient than Jupiter at ejecting objects on Earth-crossing orbits from the system (Horner & Jones, 2008).

6.1.3 Protoplanetary Discs - Investigating Possible Triggered Star Formation

Chapters 4 and 5 are focused on searching for observational evidence for triggered star formation as outlined in Elmegreen (1998). This follows on from previous work in which the evidence for triggering was based on the location of embedded clusters in clumps forming out of swept up material in molecular clouds (Phelps & Lada, 1997; Carpenter et al., 2000). These studies were centred around finding clusters and were not sensitive to any stars forming in isolation and did not produce any estimate for the relative ages of the various regions of star forming activity making it difficult to establish an age gradient across the molecular cloud.

New observations from the Spitzer Space Telescope at near and mid IR wavelengths allow individual sources with IR excesses to be identified and their evolutionary stages estimated based on the slopes of their spectral energy distributions. This gives a more detailed picture of star formation and makes it clearer which parts of a molecular cloud are in the process of forming stars and in which regions stars have formed recently but the star formation process appears complete.

In Chapter 4, the evidence for triggering via the collect and collapse of material swept up by the expanding HII region around the OB association NGC 2244 into the Rosette Molecular Cloud (RMC) is examined. There are two clusters of IR excess sources situated on the nebula cloud boundary whose location is consistent with the collect and collapse model. The majority of the star formation in the RMC is taking place in a dense ridge approximately 15-25pc from the centre of NGC 2244. Román-Zúñiga et al. (2008) argue that the shock front from the nebula may have recently passed through the cloud here and induced star formation. However, the morphology of the ridge is not consistent with a swept up shell and is 5-10pc ahead of the ionisation front. Also, there are at least three clusters identified in the survey located in parts of the cloud which have not had any interaction with the expanding ionisation front. One of these cluster contains sources exhibiting SEDs consistent with extreme youth which demonstrates that star formation is occuring in the cloud without any compression from NGC 2244. Therefore, triggered star formation associated with the collection of material by the expanding NGC 2244 ionisation front does not appear to be the dominant mode of star formation in the cloud.

Chapter 5 examines a similar scenario in the region around the W4 loop. The close to circular morphology of the loop suggests that it may be remnant from a previous HII region or supernova but there is no pulsar detected to confirm this latter suggestion. Another possibility is that the expansion is driven by outflows and winds from O stars in the cluster OCl 352 but this cluster is not centrally located, residing instead in the north ridge of the ring. AFGL 333 is one of two clusters located in the observed ring, consistent with compression of the cloud as material is swept-up. However, there are several clusters in parts of the field which include Class I sources indicating that star formation is already occurring in parts of the cloud not yet swept up. The formation of a large agglomeration of Class II objects north of OCl 352 may have been triggered by OCl 352 prior to the formation of the other clusters in which star formation is still occurring. AFGL 333 appears to be part of a larger structure into which the W4 loop is expanding. The presence of Class I sources further into the structure suggests that star formation is already taking place here without the need for further compression of the cloud by the expansion of the loop. Therefore, while it is possible that the expansion of the W4 loop triggered the onset or accelerated the star formation in AFGL 333, the process may have occurred on a similar timescale without the influence of the expanding shell. Like the Rosette, it is not clear that the dominant mode of star formation is triggering associated with the expanding shell.

The RMC and W4 loop are often cited as examples of triggered star formation where the cloud is compressed or swept up into a dense ridge which leads to the onset of gravitational collapse. In both the RMC and W4 loop, 2 clusters of IR excess sources are located in the shells with 3-4 clusters located outside of the shell. In the W4 loop the clusters are located 10-20 pc ahead of the ring and in the RMC, clusters are observed as far as 25-30 pc outside of the shell. Also, Class I sources are not exclusively found in the swept up shells implying that star formation is an on-going process in many parts of the field. These stars may have either formed by the action of an external trigger, more local triggering such as winds or outflows from adjacent clusters or gravo-turbulent collapse.

Even for young sources located in the swept up material there is sometimes a dense ridge of cloud that the front/shell is expanding into where active star formation is already taking place (e.g. W3 and the dense ridge in the RMC). This is consistent with a scenario in which the star formation observed in the swept-up shell would have taken place without the additional compression of the cloud from the expanding front; the young stars are simply revealed by the shell's radiative removal of some of the cloud. The interaction of the compressing front may have accelerated the rate of star formation in these cases but there is nothing observationally to suggest that this is the case; the fraction of IR excess sources that are Class I sources is not higher for clusters in the shell.

Therefore, there is circumstantial evidence that some stars are forming in regions of the clouds where the material appears swept up, but triggered star formation does not appear to be the dominant mode of star formation in either the RMC or the W4 loop.

6.2 Future Work

6.2.1 Recovering a Rotation Rate

The ϵ Eridani and Vega debris discs are the only debris discs close enough to the Sun with a favourable inclination angle so that individual disc features can be resolved. Identifying the clumpy structure of more distant debris discs of the same dimensions at a wavelength of 850 μm out to distances of $\sim$10 pc would require an improvement in resolution by a factor of $\sim$3 to observe the same level of detail as currently seen in the ϵ Eridani ring. This would require an aperture of diameter about 3 times that of the JCMT, approximately 50m. The Large Millimeter Telescope (LMT) is a 50m dish currently under contruction but will only be able to observe at 850 μm for $\sim$10% of the time, during the dry winter months. The technique of tracking of disc substructure as a means of planet detection via gravitational resonances is therefore currently limited to these specific cases until the construction of the Atacama Large Millimetre Array (ALMA). Using the 450 micron data would improve the resolution of the images by a factor of $\sim$2. However, this would be limited by the lack of data in the 1997-98 epoch for ϵ Eridani.

The major obstacle preventing the recovery of a rotation rate in the ϵ Eridani debris disc is the presence of the background galaxies in the field. The simulated data constructed in this thesis assumed that all of the clumps visible in the ϵ Eridani ring were not background sources and were associated with the star and debris disc. Recoding of the clump-finding algorithm used in Chapter 3 to assign pixels to clumps based on the location of the flux centroid of the nearby clumps rather than the brightest pixel values could be used to help identify clumps not co-moving with the ring. This would probably require a third epoch dataset acquired with SCUBA-2. Ideally the entire background could be modelled and subtracted out but realistically only background galaxies above a brightness threshold could be identified. These background galaxies could thus be subtracted from the image and not included when determining a rotation of the ring using χ^2-fitting. SCUBA-2 will also observe a wider field (up to $7'$) and so can identify the galaxies chopped onto with SCUBA.

The reliability of this procedure could be assessed using the simulated data. Assuming the background galaxies could be reliably subtracted from the image the same brightness threshold could then also be applied to the simulated data to account for the fact that galaxies above this threshold would have been subtracted out. Alternatively, the full galaxy counts could be used in the simulated data and the clump finding algorithm applied to identify and subtract non-moving objects from the simulated data. This way, the simulated data would be handled identically to the actual observations. In combination with a third epoch from SCUBA-2 this may improve the recovery of the input rotation rates enough that the actual rotation rate of the ring can be estimated with reasonable accuracy rather than just defining an upper limit.

6.2.2 Improved Observations - Towards a More Complete Survey of YSOs

The mid IR Spitzer data is particularly useful in identifying sources outside of the dense cores of clusters where star counting methods fail due to the small stellar surface densities for the YSOs compared to the background stars. However, observations for the Rosette and W4 regions are not complete, in particular Class III YSOs for which there is no or negligible IR excess are not included in the survey. As discussed in chapter 4, in many of the embedded clusters identified by Phelps & Lada (1997) the survey is particularly incomplete with many sources not resolved in the MIPS 24 μm band near the centres of the clusters. High resolution observations at 10 μm and 20 μm with cameras on large ground based telescopes such as Gemini and the Very Large Telescope (VLT) may allow some of the bright stars in embedded clusters to be resolved.

The high density of stars found in the interiors of embedded clusters can be probed more effectively using star counting methods which do not discriminate against Class III YSOs with no IR excess. Colour plots constructed using IRAC bands 1-2 vs 3-4 miss IR excess sources due to the lack of detections in bands 3 and 4 at 5.8 μm and 8.0 μm largely due to diffuse PAH emission at these wavelengths. Román-Zúñiga et al. (2008) have recently obtained deep J, H and K photometry using FLAMINGOS and constructed J-H vs. H-K colour-colour plots to identify young sources. This deep J, H and K photometry could also be combined with IRAC bands 1 and 2 (3.6 and 4.5 μm) to construct J-H vs. H-4.5 μm and H-K vs. K-4.5 μm colour-colour plots to identify sources missed in the IRAC bands 1-2 vs 3-4 colour-colour plots and give a more complete census of the star forming population. Observations of the W4 region in the IRAC bands and deep J, H and K bands would clearly improve the completeness of the survey completed with MIPS 24 μm only. The completeness as a function of the background flux could also be estimated using a fake star analysis. Other methods can also identify young stars. For example, Wang et al. (2008) presented the first high spatial resolution X-ray study of NGC 2244 using Chandra and plan to present Chandra observations of the embdded clusters in the RMC later this year.

The observations described above may result in more complete surveys of the young stellar objects but there still remains the possibility that star forming regions located on the edge of HII regions and bubbles may have been undergoing star formation already. The expanding HII region or shells may have simply been halted by the dense gas around the already star forming regions. In this sense the star forming regions are just being revealed but not triggered by the expanding ionisation front. Future observations will need to find more convincing signatures of triggered star formation predicted by numerical simulations, for example mapping the RMC at high resolution in CO could allow the dynamics of the clouds to be investigated and determine whether clumps or cores with stars are moving outwards with the expansion of the shell.

6.2.3 Improved Simulations - Predictions of Observational Signatures

Early models of triggering were based on only one dimension but more recent models have been extended to three dimensions. Dale et al. (2007a) showed using smoothed particle hydrodynamic (SPH) simulations that an HII region expanding into a smooth medium can result in the fragmentation of the gas. This demonstrates that an O star can cause even smooth gas that would not normally fragment and form stars to do so, via the collect and collapse model of triggered star formation. This model does not include the possible impact of secondary triggering events as envisaged by the sequential triggering suggested by Elmegreen & Lada (1977) which Dale et al. (2007a) point out may lead to the formation of many more fragments.

Dale et al. (2007b) extended this work from the simple smooth medium and used SPH simulations to observe the impact of irradiation by an external sources of ionizing photons on a turbulent molecular cloud. It was found that the feedback can drastically alter the morphology of the cloud but the impact on the star formation rate is relatively minor, increasing the star formation efficiency by $\sim$30% which was not observed in the study of the RMC presented here; in fact no over-density of IR excess sources was found at radii from NGC 2244 coincident with the nebula/cloud boundary. Comparing the results with a control run in which the cloud was left to form by itself with no ionizing photons impacting on the cloud Dale et al. (2007b) examined a number of properties of their star forming cores: masses, velocity components, total velocity, rotation components, total spin, momentum components, total momentum and kinetic energy. No observational signature was found in which the triggered cores were distinguishable from the non-triggered core in the control run but this may be because only a small number of objects were formed so the statistics are unreliable.

Larger scale versions of these simulations would produce a larger number of objects and improve the statistics so that an observational signature such as the velocities or masses of cores can be determined, so that it may be possible to distinguish between cores whose formation is triggered and those which are not. Looking for such a signature could then be used to determine whether parts of star forming regions like the RMC and W4 loop are in fact triggered or if the young stars have just been revealed by radiation passing into a denser cloud. The Dale et al. (2007a) simulation is also limited to forming high mass stars due to the resolution limit of the simulations. The numerical simulations described above could also be improved by including secondary triggering events and a larger number of particles to test whether the IMF can be recovered and seek detectable observational differences between cores formed from feedback and those that are not.

Bibliography

Allen L. E., Calvet N., D'Alessio P., Merin B., Hartmann L., Megeath S. T., Gutermuth R. A., Muzerolle J., Pipher J. L., Myers P. C., Fazio G. G., 2004, ApJS, 154, 363

Allen L. E., Hora J. L., Megeath S. T., Deutsch L. K., Fazio G. G., Chavarria L., dell R. W., 2005, in IAU Symposium, Cesaroni R., Felli M., Churchwell E., Walmsley M., eds., pp. 352–357

Andre P., Ward-Thompson D., Barsony M., 1993, ApJ, 406, 122

Archibald E. N., Jenness T., Holland W. S., Coulson I. M., Jessop N. E., Stevens J. A., Robson E. I., Tilanus R. P. J., Duncan W. D., Lightfoot J. F., 2002, MNRAS, 336, 1

Audley M. D., Holland W. S., Hodson T., MacIntosh M., Robson I., Irwin K. D., Hilton G., Duncan W. D., Reintsema C., Walton A. J., Parkes W., Ade P. A. R., Walker I., Fich M., Kycia J., Halpern M., Naylor D. A., Mitchell G., Bastien P., 2004, in Presented at the Society of Photo-Optical Instrumentation Engineers (SPIE) Conference, Vol. 5498, Millimeter and Submillimeter Detectors for Astronomy II. Edited by Jonas Zmuidzinas, Wayne S. Holland and Stafford Withington Proceedings of the SPIE, Volume 5498, pp. 63-77 (2004)., Bradford C. M., Ade P. A. R., Aguirre J. E., Bock J. J., Dragovan M., Duband L., Earle L., Glenn J., Matsuhara H., Naylor B. J., Nguyen H. T., Yun M., Zmuidzinas J., eds., pp. 63–77

Aumann H. H., 1985, PASP, 97, 885

—, 1988, AJ, 96, 1415

Aumann H. H., Beichman C. A., Gillett F. C., de Jong T., Houck J. R., Low F. J., Neugebauer G., Walker R. G., Wesselius P. R., 1984, ApJ, 278, L23

Backman D. E., Dasgupta A., Stencel R. E., 1995, ApJ, 450, L35+

Backman D. E., Paresce F., 1993, in Protostars and Planets III, Levy E. H., Lunine J. I., eds., pp. 1253–1304

Balog Z., Muzerolle J., Rieke G. H., Su K. Y. L., Young E. T., Megeath S. T., 2007, ApJ, 660, 1532

Barnard V. E., Vielva P., Pierce-Price D. P. I., Blain A. W., Barreiro R. B., Richer J. S., Qualtrough C., 2004, MNRAS, 352, 961

Bary J. S., Weintraub D. A., Kastner J. H., 2003, ApJ, 586, 1136

Basu S., Johnstone D., Martin P. G., 1999, ApJ, 516, 843

Beichman C. A., Bryden G., Rieke G. H., Stansberry J. A., Trilling D. E., Stapelfeldt K. R., Werner M. W., Engelbracht C. W., Blaylock M., Gordon K. D., Chen C. H., Su K. Y. L., Hines D. C., 2005, ApJ, 622, 1160

Beichman C. A., Bryden G., Stapelfeldt K. R., Gautier T. N., Grogan K., Shao M., Velusamy T., Lawler S. M., Blaylock M., Rieke G. H., Lunine J. I., Fischer D. A., Marcy G. W., Greaves J. S., Wyatt M. C., Holland W. S., Dent W. R. F., 2006, ApJ, 652, 1674

Benedict G. F., McArthur B. E., Gatewood G., Nelan E., Cochran W. D., Hatzes A., Endl M., Wittenmyer R., Baliunas S. L., Walker G. A. H., Yang S., Kürster M., Els S., Paulson D. B., 2006, AJ, 132, 2206

Berry D. S., Reinhold K., Jenness T., Economou F., 2007, in Astronomical Society of the Pacific Conference Series, Vol. 376, Astronomical Data Analysis Software and Systems XVI, Shaw R. A., Hill F., Bell D. J., eds., pp. 425–+

Bertin E., Arnouts S., 1996, A&AS, 117, 393

Blitz L., Stark A. A., 1986, ApJ, 300, L89

Blitz L., Thaddeus P., 1980, ApJ, 241, 676

Block D. L., 1990, Nature, 347, 452

Block D. L., Geballe T. R., Dyson J. E., 1993, A&A, 273, L41+

Bonnor W. B., 1956, MNRAS, 116, 351

Bontemps S., André P., Kaas A. A., Nordh L., Olofsson G., Huldtgren M., Abergel A., Blommaert J., Boulanger F., Burgdorf M., Cesarsky C. J., Cesarsky D., Copet E., Davies J., Falgarone E., Lagache G., Montmerle T., Pérault M., Persi P., Prusti T., Puget J. L., Sibille F., 2001, A&A, 372, 173

Boss A. P., 2000, ApJ, 536, L101

Brott I., Hauschildt P. H., 2005, in ESA SP-576: The Three-Dimensional Universe with Gaia, Turon C., O'Flaherty K. S., Perryman M. A. C., eds., pp. 565–+

Bryden G., Beichman C. A., Trilling D. E., Rieke G. H., Holmes E. K., Lawler S. M., Stapelfeldt K. R., Werner M. W., Gautier T. N., Blaylock M., Gordon K. D., Stansberry J. A., Su K. Y. L., 2006, ApJ, 636, 1098

Burns J. A., Lamy P. L., Soter S., 1979, Icarus, 40, 1

Carpenter J. M., Heyer M. H., Snell R. L., 2000, ApJS, 130, 381

Chambers J. E., 2004, Earth and Planetary Science Letters, 223, 241

Chandrasekhar S., Fermi E., 1953, ApJ, 118, 113

Chen H., Myers P. C., Ladd E. F., Wood D. O. S., 1995, ApJ, 445, 377

Cohen M., Kuhi L. V., 1979, ApJS, 41, 743

Cohen M., Megeath S. T., Hammersley P. L., Martín-Luis F., Stauffer J., 2003, AJ, 125, 2645

Cox P., Deharveng L., Leene A., 1990, A&A, 230, 181

Currie M., 2004, Starlink User Note 95.28

Daigle A., Joncas G., Parizeau M., 2007, ApJ, 661, 285

Dale J. E., Bonnell I. A., Whitworth A. P., 2007a, MNRAS, 375, 1291

Dale J. E., Clark P. C., Bonnell I. A., 2007b, MNRAS, 377, 535

Deharveng L., Zavagno A., Caplan J., 2005, A&A, 433, 565

Dennison B., Topasna G. A., Simonetti J. H., 1997, ApJ, 474, L31+

Dent W. R. F., Walker H. J., Holland W. S., Greaves J. S., 2000, MNRAS, 314, 702

Di Folco E., Thévenin F., Kervella P., Domiciano de Souza A., Coudé du Foresto V., Ségransan D., Morel P., 2004, A&A, 426, 601

Diehl R., Halloin H., Kretschmer K., Lichti G. G., Schönfelder V., Strong A. W., von Kienlin A., Wang W., Jean P., Knödlseder J., Roques J.-P., Weidenspointner G., Schanne S., Hartmann D. H., Winkler C., Wunderer C., 2006, Nature, 439, 45

Digel S. W., Lyder D. A., Philbrick A. J., Puche D., Thaddeus P., 1996, ApJ, 458, 561

Dominik C., Decin G., 2003, ApJ, 598, 626

Dominik C., Laureijs R. J., Jourdain de Muizon M., Habing H. J., 1998, A&A, 329, L53

Duquennoy A., Mayor M., 1991, A&A, 248, 485

Ebert R., 1957, Zeitschrift fur Astrophysik, 42, 263

Elmegreen B., 1992, in Star Formation in Stellar Systems, Tenorio-Tagle G., Prieto M., Sanchez F., eds., pp. 381–+

Elmegreen B. G., 1985, in Birth and the Infancy of Stars, Lucas R., Omont A., Stora R., eds., pp. 215–254

—, 1989, ApJ, 340, 786

—, 1998, in ASP Conf. Ser. 148: Origins, Woodward C. E., Shull J. M., Thronson Jr. H. A., eds., pp. 150–+

Elmegreen B. G., Lada C. J., 1977, ApJ, 214, 725

Erickson E. F., Knacke R. F., Tokunaga A. T., Haas M. R., 1981, ApJ, 245, 148

Fajardo-Acosta S. B., Telesco C. M., Knacke R. F., 1998, AJ, 115, 2101

Fazio G. G., 2005, in Neutrinos and Explosive Events in the Universe, Shapiro M. M., Stanev T., Wefel J. P., eds., pp. 47–+

Fazio G. G., Hora J. L., Allen L. E., Ashby M. L. N., Barmby P., Deutsch L. K., Huang J.-S., Kleiner S., Marengo M., Megeath S. T., Melnick G. J., Pahre M. A., Patten B. M., Polizotti J., Smith H. A., Taylor R. S., Wang Z., Willner S. P., Hoffmann W. F., Pipher J. L., Forrest W. J., McMurty C. W., McCreight C. R., McKelvey M. E., McMurray R. E., Koch D. G., Moseley S. H., Arendt R. G., Mentzell J. E., Marx C. T., Losch P., Mayman P., Eichhorn W., Krebs D., Jhabvala M., Gezari D. Y., Fixsen D. J., Flores J., Shakoorzadeh K., Jungo R., Hakun C., Workman L., Karpati G., Kichak R., Whitley R., Mann S., Tollestrup E. V., Eisenhardt P., Stern D., Gorjian V., Bhattacharya B., Carey S., Nelson B. O., Glaccum W. J., Lacy M., Lowrance P. J., Laine S., Reach W. T., Stauffer J. A., Surace J. A., Wilson G., Wright E. L., Hoffman A., Domingo G., Cohen M., 2004a, ApJS, 154, 10

Fazio G. G., Hora J. L., Allen L. E., Ashby M. L. N., Barmby P., Deutsch L. K., Huang J.-S., Marengo M., Megeath S. T., Pahre M. A., Patten B. M., Wang Z., Willner S. P., Hoffmann W. F., Moseley S. H., Arendt R. G., Mentzell J. E., Trout-Marx C., Eisenhardt E., Stern D., Gorjian V., Bhattacharya B., Carey S., Glaccum W. J., Lacy M., Lowrance P. J., Laine S., Nelson B. O., Reach W. T., Stauffer J. R., Surace J. A., Wilson G., Pipher J. L., Forrest W. J., McMurty C. W., McCreight C. R., McKelvey M. E., McMurray R. E., 2004b, in Bulletin of the American Astronomical Society, Vol. 36, Bulletin of the American Astronomical Society, pp. 699–+

Fischer D. A., Butler R. P., Marcy G. W., Vogt S. S., Henry G. W., 2003, ApJ, 590, 1081

Fixsen D. J., Dwek E., 2002, ApJ, 578, 1009

Gaustad J. E., 1963, ApJ, 138, 1050

Gomes R. S., 2003, Icarus, 161, 404

Gomez M., Hartmann L., Kenyon S. J., Hewett R., 1993, AJ, 105, 1927

Greaves J. S., Holland W. S., Jayawardhana R., Wyatt M. C., Dent W. R. F., 2004a, MNRAS, 348, 1097

Greaves J. S., Holland W. S., Moriarty-Schieven G., Jenness T., Dent W. R. F., Zuckerman B., McCarthy C., Webb R. A., Butner H. M., Gear W. K., Walker H. J., 1998, ApJ, 506, L133

Greaves J. S., Holland W. S., Wyatt M. C., Dent W. R. F., Robson E. I., Coulson I. M., Jenness T., Moriarty-Schieven G. H., Davis G. R., Butner H. M., Gear W. K., Dominik C., Walker H. J., 2005, ApJ, 619, L187

Greaves J. S., Wyatt M. C., 2003, MNRAS, 345, 1212

Greaves J. S., Wyatt M. C., Holland W. S., Dent W. R. F., 2004b, MNRAS, 351, L54

Gulliver A. F., Hill G., Adelman S. J., 1994, ApJ, 429, L81

Gutermuth R. A., Megeath S. T., Pipher J. L., Williams J. P., Allen L. E., Myers P. C., Raines S. N., 2005, ApJ, 632, 397

Habing H. J., Dominik C., Jourdain de Muizon M., Laureijs R. J., Kessler M. F., Leech K., Metcalfe L., Salama A., Siebenmorgen R., Trams N., Bouchet P., 2001, A&A, 365, 545

Haisch Jr. K. E., Lada E. A., Lada C. J., 2001a, AJ, 121, 2065

—, 2001b, ApJ, 553, L153

Haisch Jr. K. E., Lada E. A., Piña R. K., Telesco C. M., Lada C. J., 2001c, AJ, 121, 1512

Hanawa T., Nakayama K., 1997, ApJ, 484, 238

Hartigan P., Hartmann L., Kenyon S. J., Strom S. E., Skrutskie M. F., 1990, ApJ, 354, L25

Hatzes A. P., Cochran W. D., McArthur B., Baliunas S. L., Walker G. A. H., Campbell B., Irwin A. W., Yang S., Kürster M., Endl M., Els S., Butler R. P., Marcy G. W., 2000, ApJ, 544, L145

Hayashi C., 1966, ARA&A, 4, 171

Hayashi C., Hōshi R., Sugimoto D., 1962, Progress of Theoretical Physics Supplement, 22, 1

Hayashi C., Nakano T., 1965, Progress of Theoretical Physics, 34, 754

Henyey L. G., Lelevier R., Levée R. D., 1955, PASP, 67, 154

Heyer M. H., Williams J. P., Brunt C. M., 2006, ApJ, 643, 956

Hildebrand R. H., 1983, QJRAS, 24, 267

Hiltner W. A., 1949, ApJ, 109, 471

—, 1951, ApJ, 114, 241

Holland W. S., Greaves J. S., Dent W. R. F., Wyatt M. C., Zuckerman B., Webb R. A., McCarthy C., Coulson I. M., Robson E. I., Gear W. K., 2003, ApJ, 582, 1141

Holland W. S., Greaves J. S., Zuckerman B., Webb R. A., McCarthy C., Coulson I. M., Walther D. M., Dent W. R. F., Gear W. K., Robson I., 1998, Nature, 392, 788

Holland W. S., Robson E. I., Gear W. K., Cunningham C. R., Lightfoot J. F., Jenness T., Ivison R. J., Stevens J. A., Ade P. A. R., Griffin M. J., Duncan W. D., Murphy J. A., Naylor D. A., 1999, MNRAS, 303, 659

Horner J., Jones B. W., 2008, Astronomy and Geophysics, 49, 22

Hubickyj O., Bodenheimer P., Lissauer J. J., 2005, Icarus, 179, 415

Jayawardhana R., Wolk S. J., Barrado y Navascués D., Telesco C. M., Hearty T. J., 2001, ApJ, 550, L197

Jeans J., 1902, Philos. Trans. R. Soc. London, Ser. A, 199, 1

Jenness T., Lightfoot J. F., 1998, in Astronomical Society of the Pacific Conference Series, Vol. 145, Astronomical Data Analysis Software and Systems VII, Albrecht R., Hook R. N., Bushouse H. A., eds., pp. 216–+

Jenness T., Lightfoot J. F., Holland W. S., 1998, in Presented at the Society of Photo-Optical Instrumentation Engineers (SPIE) Conference, Vol. 3357, Proc. SPIE Vol. 3357, p. 548-558, Advanced Technology MMW, Radio, and Terahertz Telescopes, Thomas G. Phillips; Ed., Phillips T. G., ed., pp. 548–558

Johnstone D., Hollenbach D., Bally J., 1998, ApJ, 499, 758

Joy A. H., 1945, ApJ, 102, 168

Jura M., 1990, ApJ, 365, 317

Kalas P., Jewitt D., 1996, AJ, 111, 1347

Kenyon S. J., Bromley B. C., 2002, ApJ, 577, L35

—, 2004, AJ, 127, 513

Kenyon S. J., Hartmann L., 1995, ApJS, 101, 117

Kitamura Y., Momose M., Yokogawa S., Kawabe R., Tamura M., Ida S., 2002, ApJ, 581, 357

Konigl A., Pudritz R. E., 2000, Protostars and Planets IV, 759

Kroupa P., 2001, MNRAS, 322, 231

Lada C. J., 1987, in IAU Symp. 115: Star Forming Regions, Peimbert M., Jugaku J., eds., pp. 1–17

Lada C. J., Elmegreen B. G., Cong H.-I., Thaddeus P., 1978, ApJ, 226, L39

Lada C. J., Lada E. A., 2003, ARA&A, 41, 57

Lada C. J., Wilking B. A., 1984, ApJ, 287, 610

Lada E. A., Lada C. J., 1995, AJ, 109, 1682

Landgraf M., Liou J.-C., Zook H. A., Grün E., 2002, AJ, 123, 2857

Langer W. D., van Dishoeck E. F., Bergin E. A., Blake G. A., Tielens A. G. G. M., Velusamy T., Whittet D. C. B., 2000, Protostars and Planets IV, 29

Larson R. B., 1969, MNRAS, 145, 271

—, 1981, MNRAS, 194, 809

Levison H. F., Morbidelli A., 2003, Nature, 426, 419

Li A., Greenberg J. M., 1997, A&A, 323, 566

Li J. Z., Smith M., 2005a, AJ, 130, 721

Li J. Z., Smith M. D., 2005b, ApJ, 620, 816

—, 2005c, AJ, 130, 2757

Lin D. N. C., Bodenheimer P., Richardson D. C., 1996, Nature, 380, 606

Liou J.-C., Zook H. A., 1999, AJ, 118, 580

Mac Low M.-M., Klessen R. S., 2004, Reviews of Modern Physics, 76, 125

Macintosh B. A., Becklin E. E., Kaisler D., Konopacky Q., Zuckerman B., 2003, ApJ, 594, 538

Makovoz D., Marleau F. R., 2005, PASP, 117, 1113

Makovoz D., Roby T., Khan I., Booth H., 2006, in Advanced Software and Control for Astronomy. Edited by Lewis, Hilton; Bridger, Alan. Proceedings of the SPIE, Volume 6274, pp. (2006).

Malhotra R., 1995, AJ, 110, 420

Mamajek E. E., Meyer M. R., Hinz P. M., Hoffmann W. F., Cohen M., Hora J. L., 2004, ApJ, 612, 496

Mannings V., Barlow M. J., 1998, ApJ, 497, 330

Marcy G., Butler R. P., Fischer D., Vogt S., Wright J. T., Tinney C. G., Jones H. R. A., 2005, Progress of Theoretical Physics Supplement, 158, 24

Marsh K. A., Velusamy T., Dowell C. D., Grogan K., Beichman C. A., 2005, ApJ, 620, L47

Massey P., Johnson K. E., Degioia-Eastwood K., 1995, ApJ, 454, 151

Mathieu R. D., Ghez A. M., Jensen E. L. N., Simon M., 2000, Protostars and Planets IV, 703

McKee C. F., 1989, ApJ, 345, 782

Megeath S. T., Allen L. E., Gutermuth R. A., Pipher J. L., Myers P. C., Calvet N., Hartmann L., Muzerolle J., Fazio G. G., 2004, ApJS, 154, 367

Megeath S. T., Flaherty K. M., Hora J., Allen L. E., Fazio G. G., Hartmann L., Myers P. C., Muzerolle J., Pipher J. L., Siegler N., Stauffer J. R., Young E., 2005, in IAU Symposium, Cesaroni R., Felli M., Churchwell E., Walmsley M., eds., pp. 383–388

Mestel L., Spitzer Jr. L., 1956, MNRAS, 116, 503

Miller G. E., Scalo J. M., 1979, ApJS, 41, 513

Miyama S. M., Narita S., Hayashi C., 1987, Progress of Theoretical Physics, 78, 1273

Morbidelli A., Brown M. E., Levison H. F., 2003, Earth Moon and Planets, 92, 1

Moro-Martín A., Malhotra R., 2002, AJ, 124, 2305

Mueller M. W., Arnett W. D., 1976, ApJ, 210, 670

Najita J., Carr J. S., Mathieu R. D., 2003, ApJ, 589, 931

Nakano T., 1998, ApJ, 494, 587

Nelson R. P., Papaloizou J. C. B., Masset F., Kley W., 2000, MNRAS, 318, 18

Nishi R., 1992, Progress of Theoretical Physics, 87, 347

Norman C. A., Ikeuchi S., 1989, ApJ, 345, 372

Normandeau M., Taylor A. R., Dewdney P. E., 1996, Nature, 380, 687

—, 1997, ApJS, 108, 279

Oey M. S., Watson A. M., Kern K., Walth G. L., 2005, AJ, 129, 393

Ozernoy L. M., Gorkavyi N. N., Mather J. C., Taidakova T. A., 2000, ApJ, 537, L147

Peretto N., André P., Belloche A., 2006, A&A, 445, 979

Phelps R. L., Lada E. A., 1997, ApJ, 477, 176

Phelps R. L., Ybarra J. E., 2005, ApJ, 627, 845

Proffitt C. R., Sahu K., Livio M., Krist J., Calzetti D., Gilliland R., Grady C., Lindler D., Woodgate B., Heap S., Clampin M., Gull T. R., Lisse C. M., 2004, ApJ, 612, 481

Quillen A. C., Thorndike S., 2002, ApJ, 578, L149

Rand R. J., Kulkarni S. R., 1989, ApJ, 343, 760

Rand R. J., Lyne A. G., 1994, MNRAS, 268, 497

Reach W. T., Megeath S. T., Cohen M., Hora J., Carey S., Surace J., Willner S. P., Barmby P., Wilson G., Glaccum W., Lowrance P., Marengo M., Fazio G. G., 2005, PASP, 117, 978

Reynolds R. J., Sterling N. C., Haffner L. M., 2001, ApJ, 558, L101

Rieke G. H., Su K. Y. L., Stansberry J. A., Trilling D., Bryden G., Muzerolle J., White B., Gorlova N., Young E. T., Beichman C. A., Stapelfeldt K. R., Hines D. C., 2005, ApJ, 620, 1010

Robitaille T. P., Whitney B. A., Indebetouw R., Wood K., 2007, ApJS, 169, 328

Robitaille T. P., Whitney B. A., Indebetouw R., Wood K., Denzmore P., 2006, ApJS, 167, 256

Román-Zúñiga C. G., Elston R., Ferreira B., Lada E. A., 2008, ApJ, 672, 861

Roques F., Scholl H., Sicardy B., Smith B. A., 1994, Icarus, 108, 37

Saar S. H., Osten R. A., 1997, MNRAS, 284, 803

Sakai T., Oka T., Yamamoto S., 2006, ApJ, 649, 268

Sasselov D. D., Lecar M., 2000, ApJ, 528, 995

Schütz O., Nielbock M., Wolf S., Henning T., Els S., 2004, A&A, 414, L9

Schwartz P. R., 1982, ApJ, 252, 589

Sheret I., Dent W. R. F., Wyatt M. C., 2004, MNRAS, 348, 1282

Shu F. H., 1977, ApJ, 214, 488

—, 1982, The Physical Universe: An Introduction to Astronomy. University Science Books, Sausalito, California, p. 146

Silk J., Suto Y., 1988, ApJ, 335, 295

Skrutskie M. F., Dutkevitch D., Strom S. E., Edwards S., Strom K. M., Shure M. A., 1990, AJ, 99, 1187

Smail I., Ivison R. J., Blain A. W., 1997, ApJ, 490, L5+

Smith B. A., Terrile R. J., 1984, Science, 226, 1421

Smith L. F., Mezger P. G., Biermann P., 1978, A&A, 66, 65

Snell R. L., Loren R. B., Plambeck R. L., 1980, ApJ, 239, L17

Soderblom D. R., Dappen W., 1989, ApJ, 342, 945

Song I., Caillault J.-P., Barrado y Navascués D., Stauffer J. R., Randich S., 2000, ApJ, 533, L41

Spangler C., Sargent A. I., Silverstone M. D., Becklin E. E., Zuckerman B., 2001, ApJ, 555, 932

Stassun K. G., Mathieu R. D., Vrba F. J., Mazeh T., Henden A., 2001, AJ, 121, 1003

Strobel A., 1992, A&A, 253, 374

Strom S. E., 1977, in IAU Symposium, Vol. 75, Star Formation, de Jong T., Maeder A., eds., pp. 179–197

Tafalla M., Mardones D., Myers P. C., Caselli P., Bachiller R., Benson P. J., 1998, ApJ, 504, 900

Tenorio-Tagle G., Bodenheimer P., 1988, ARA&A, 26, 145

Terebey S., Fich M., Taylor R., Cao Y., Hancock T., 2003, ApJ, 590, 906

Thi W. F., van Dishoeck E. F., Blake G. A., van Zadelhoff G. J., Horn J., Becklin E. E., Mannings V., Sargent A. I., van den Ancker M. E., Natta A., Kessler J., 2001, ApJ, 561, 1074

Thronson Jr. H. A., Campbell M. F., Hoffmann W. F., 1980, ApJ, 239, 533

Timmes F. X., Diehl R., Hartmann D. H., 1997, ApJ, 479, 760

Trilling D. E., Bryden G., Beichman C. A., Rieke G. H., Su K. Y. L., Stansberry J. A., Blaylock M., Stapelfeldt K. R., Beeman J. W., Haller E. E., 2008, ApJ, 674, 1086

Troland T. H., Heiles C., 1986, ApJ, 301, 339

Valenti J. A., Fischer D. A., 2005, ApJS, 159, 141

van Dishoeck E. F., Blake G. A., 1998, ARA&A, 36, 317

van Dishoeck E. F., Blake G. A., Draine B. T., Lunine J. I., 1993, in Protostars and Planets III, Levy E. H., Lunine J. I., eds., pp. 163–241

Wang J., Townsley L. K., Feigelson E. D., Broos P. S., Getman K. V., Román-Zúñiga C. G., Lada E., 2008, ApJ, 675, 464

West J. L., English J., Normandeau M., Landecker T. L., 2007, ApJ, 656, 914

Whitworth A. P., Bhattal A. S., Francis N., Watkins S. J., 1996, MNRAS, 283, 1061

Williams J. P., Blitz L., Stark A. A., 1995, ApJ, 451, 252

Williams J. P., de Geus E. J., Blitz L., 1994, ApJ, 428, 693

Williams J. P., Myers P. C., Wilner D. J., di Francesco J., 1999, ApJ, 513, L61

Williams J. P., Najita J., Liu M. C., Bottinelli S., Carpenter J. M., Hillenbrand L. A., Meyer M. R., Soderblom D. R., 2004, ApJ, 604, 414

Winston E., Megeath S. T., Wolk S. J., Muzerolle J., Gutermuth R., Hora J. L., Allen L. E., Spitzbart B., Myers P., Fazio G. G., 2007, ArXiv e-prints, 707

Wolk S. J., Walter F. M., 1996, AJ, 111, 2066

Wyatt M. C., 2005, A&A, 433, 1007

Wyatt M. C., Dent W. R. F., 2002, MNRAS, 334, 589

Wyatt M. C., Dent W. R. F., Greaves J. S., 2003, MNRAS, 342, 876

Wyatt M. C., Dermott S. F., Telesco C. M., Fisher R. S., Grogan K., Holmes E. K., Piña R. K., 1999, ApJ, 527, 918

Wyatt M. C., Greaves J. S., Dent W. R. F., Coulson I. M., 2005, ApJ, 620, 492

Zuckerman B., Becklin E. E., 1993, ApJ, 414, 793